

JAXA Special Publication

Proceedings of the 40th JAXA Workshop on “Investigation and Control of Boundary-Layer Transition”

**Steering Committee of JAXA Workshop on
“Investigation and Control of Boundary-Layer Transition”**

February 2008

Japan Aerospace Exploration Agency

「境界層遷移の解明と制御」研究会

幹事

空気力学研究グループ	高 木 正 平
空気力学研究グループ	徳 川 直 子
空気力学研究グループ	跡 部 隆

客員研究官（昭和 62, 63, 平成元年度）	
大阪府立大学名誉教授	西 岡 通 男
客員研究官（昭和 62, 63, 平成 3 年度）	
東北大学流体科学研究所教授	小 濱 泰 昭
客員研究官（平成 2, 3, 5, 10 年度）	
東京都立科学技術大学教授	浅 井 雅 人
客員研究官（平成 4, 5, 6 年度）	
日本大学理工学部教授	本 橋 龍 郎
客員研究官（平成 6, 7, 8 年度）	
東北大学工学部教授	福 西 祐
客員研究官（平成 7, 8, 9 年度）	
豊橋技術科学大学教授	蒔 田 秀 治
客員（平成 14, 15, 16, 17, 18, 19 年度）	
元帝京大学理工学部教授	伊 藤 信 毅
客員（17, 18, 19 年度）	
明治大学理工学部	山 本 稀 義

JAXA Special Publication
宇宙航空研究開発機構特別資料

Proceedings of the 40th JAXA Workshop on
“Investigation and Control of Boundary-Layer Transition”

「境界層遷移の解明と制御」研究会講演論文集
(第 40 回)

Steering Committee of JAXA Workshop on
“Investigation and Control of Boundary-Layer Transition”

「境界層遷移の解明と制御」研究会

February 2008
2008 年 2 月

Japan Aerospace Exploration Agency
宇宙航空研究開発機構

はしがき

本報告集は、2007年3月14日から16日まで、宮崎県日向市美々津軒において開催された第40回「境界層遷移の解明と制御」研究会の講演要旨を収録したものである。今回の研究会は会の発足から20年の節目の年に当たることから会場を東京から地方に移し、東北大学流体科学研究所の21世紀COEプログラム「流動ダイナミックス国際研究教育拠点」と共同で開催し、公用語を英語とする国際会議（境界層の層流から乱流への遷移研究に関する国際ワークショップ）の形式で行われた。海外から著名な研究者5名をお招きして、それぞれの分野における最先端の研究成果についての解説をお願いすると共に、我が国における遷移研究の現状を直接知って頂くこととした。また、国内からも著名な5名を招待して、最新の研究成果や日本の流体力学研究の回顧などをお願いした。さらに、ポスター発表も取り入れ、自由な質問と討論の場を設けた。講演並びにポスター発表における討論は有益かつ活発で、会議は全体として大きな成果を収めることができた。招待講演を含む全ての講演者、会議への参加者、会場を提供して下さった日向市教育委員会、その他の関係者に対して、幹事一同心から感謝し、厚くお礼を申し上げる。

Preface

This issue forms the Proceedings of the 40th JAXA Workshop on “Investigation and Control of Boundary-Layer Transition”, which was held on the 14th to 16th of March, 2007, at Mimitsu-ken in Hyuga City, Miyazaki, as the International Workshop on Boundary-Layer Transition Study. The Workshop was cosponsored by Institute of Aerospace Technology/JAXA and the 21st Century COE Program, Institute of Fluid Science/Tohoku University. Ten distinguished scientists were invited from abroad and inland and gave keynote lectures on recent development of some fundamental researches and presentations associated with this field. The Conference was very active and presented a lot of things to be learned and so was undoubtedly a great success. All members of the Steering Committee express their thanks to all the speakers and participants for their contributions to this success. Thanks are also extended to the municipal Board of Education, for allowing us to use Mimitsu-ken, which is located at the reservation district for important cultural assets.

Chofu, December 2007

S. Takagi
Y. Kohama
Co-chairs of Workshop

International Workshop on Boundary-Layer Transition Study

March 13-16, 2007

Mimitsu, Hyuga, Miyazaki, Japan

Hosted by

21st Century COE Program Flow Dynamics International Research Educational Base
and
Institute of Aerospace Technology, Japan Aerospace Exploration Agency

Supported by

Institute of Fluid Science, Tohoku University

Workshop Co-chair

Yasuaki Kohama (IFS, Tohoku Univ.)
Shohei Takagi (IAT, JAXA)

Executive Committee

Yasuaki Kohama (IFS, Tohoku Univ.)
Shohei Takagi (IAT, JAXA)
Shuya Yoshioka (Sunrise Beach Research Facility, IFS, Tohoku Univ.)
Takashi Atobe (IAT, JAXA)

Secretary

Shuya Yoshioka (Sunrise Beach Research Facility, IFS, Tohoku Univ.)



The workshop was held at “Mimitsu-ken”, which is a Japanese typical house about 100 years old located at middle of Miyazaki Prefecture.



Participants.

Program

March 13

- 17:00 Shuttle bus departs from Hotel Melissa Hyuga for Hyuga Sun Park.
Welcome Reception at Hyuga Sun Park
- 17:30 Japanese Drum Playing Performance by Tenchikokyō-shōunentai.
- 18:30- Cocktail
- 20:00

March 14

- 9:00-9:10 Welcome address by Yasuaki Kohama (Workshop co-chair, IFS, Tohoku Univ.)
- 9:10-11:30 Session: JAXA 20th anniversary of Investigation and Control of Boundary-Layer Transition Workshop
Chair: Shohei Takagi (Workshop co-chair, IAT, JAXA)
- 9:10-9:20 Opening address by Shohei Takagi (IAT, JAXA)
- 9:20-10:20 The detailed structure of randomization process in free shear layers
by Hiroshi Sato, Hironosuke Saito and Hiroshi Nakamura (Institute of Flow Research)
- 10:30- Statistical Mechanics of Turbulence based on Cross-
11:30 Independence Closure Hypothesis
by Tomomasa Tatsumi (Kyoto University)
- 11:30- Lunch
- 12:40
- 12:40- Session: Experiments in Sunrise beach research facility
13:05 Chair: Takuma Kato (IFS, Tohoku Univ.)
- 12:40- Aerotrains, challenge to zero emission high speed
13:05 transportation system
by Yasuaki Kohama (IFS, Tohoku Univ.)
- 13:05- Introduction of Towing wind tunnel facility in Sunrise beach
13:30 research facility
by Shuya Yoshioka (Sunrise beach research facility, IFS, Tohoku Univ.)
- 13:30- Testing the Effects of Surface Steps on Transition at the
13:55 Towing Wind Tunnel
by Anne Bender and Aaron Drake (Northrop Grumman Corporation)
- 14:15- Session: COE invited lectures 1

17:25 Chair: Shuya Yoshioka (Sunrise beach research facility, IFS, Tohoku Univ.)

14:15- Life after Finite Fossil Fuel
15:15 by Hans Tholstrup

15:15- Recent developments in turbulent flow control
16:15 by Kwing-So Choi, Tim Jukes (University of Nottingham), Takehiko Segawa and Hiro Yoshida (AIST)

16:25- An Experimental Study on the Structure of the Flow past a
17:25 Cylinder-Plane Junction
by Qing-Ding Wei (Peking University)

March 15

9:00- Session: COE invited lectures 2
12:10 Chair: Yasuaki Kohama (IFS, Tohoku Univ.)

9:00- Large-Eddy Simulation of Transition in Wall-Bounded
10:00 Flow
by Leonhard Kleiser (ETH Zurich)

10:00- On the Concept of Hydraulically Smooth Wall
11:00 by J. M. Floryan (The University of Western Ontario)

11:10- Early Times of Fluid Mechanics in Japan: Terada,
12:10 Tani, Imai, and Aeronautical Research Institute
by Tsutomu Kambe (Science Council of Japan)

12:10- Lunch
13:20

13:20- Poster session
14:50

14:50- Tea break
15:30 Ofunade dango (traditional sweets) making performance by Hisae Sato.

15:30- Session: General talks
17:45 Chair: Takashi Atobe (IAT, JAXA)

15:30- An investigation on airfoil tonal noise generation
15:55 by Marthijn Tuinstra (National Aerospace laboratory NLR)

15:55- Detailed flow field around a leading-edge slat at low
16:20 Reynolds numbers
by Sanehiro MAKIYA, Ayumu INASAWA and Masahito ASAI (Tokyo Metropolitan University)

16:20- Control of Vortex Pairing in a Two Dimensional
16:45 Parabolic Jet

by Hideharu MAKITA, Nobumasa SEKISHITA
(Toyohashi University of Technology) and Takeru
MORITA (Toyo Carrier Engineering Co., Ltd)

16:55- Flow Control with Pitching Motion of UAV using MEMS
17:20 Flow Sensors

by Hiroshi Tokutake, Shigeru Sunada, Jin Fujinaga
and Yukio Ohtuka (Osaka Prefecture University)

17:20- Measurements of Fluctuations of Mass Flux and
17:45 Concentration in Supersonic Air/Helium Mixing by Hot-
Wire Anemometry

by Akira KONDO, Shoji SAKAUE and Takakage ARAI
(Osaka Prefecture University)

17:45- Closing address by Shohei Takagi (Workshop co-chair, IAT, JAXA)
17:50

18:20- Workshop dinner at Tokiwa
20:20

March 16

Workshop tour

9:30-10:15 Sunrise Beach Research Facility

10:15-13:00 Guided sightseeing tour around Umagase area

List of Poster Presentations

No. 1

On the critical Reynolds number of the drag coefficient for a circular cylinder
by Tatsuya Matsui (Gifu University)

No. 2

Wall normal jet produced by surface plasma actuator at elevated temperature
by Takehiko Segawa, Hirohide Furutani, Hiro Yoshida (AIST), Timothy Jukes and Kwing-So
Choi (University of Nottingham)

No. 3

Strain field in compressible isotropic turbulence
by Hideaki Miura (National Institute for Fusion Science)

No. 4

Numerical simulations of flow past a 2-D airfoil at a low Reynolds number
by Tomoaki IKEDA, Takuji KUROTAKE, Takahiro SUMI and Shohei TAKAGI (JAXA)

No. 5

The Velocity Distribution Around Aerofoil for Wing in Ground Effect
by Satoshi KIKUCHI, Yasuaki KOZATO, Shigeki IMAO and Hiroyuki MITSUI (Gifu University)

No. 6

Experiments at the Sunrise-Beach Research Facility of the Aerodynamic Characteristics on Ground Effects of Aerofoils with a Secondary Aerofoil
by Yuji Takahashi (Miyakonojo National College of Technology), Masanori Kikuchi, Kimitaka Hirano, Toshio Yuge, Taisi Moriya (University of Miyazaki) and Yasuaki Kohama (Tohoku University)

No. 7

An Experimental Study of the flow field on high speed railroads to investigate a ballast flying phenomena
by Joo-hyun RHO, Yo-cheon KU, Su-hwan YUN (Seoul National University), Jong-soo HA (Hyundai Motor Company) and Dong-ho LEE (Seoul National University)

No. 8

Friction Wear Properties between Partially Polished CVD Diamond and Structural Steel
by Hiroyuki Miki, Naoki Yoshida, Toshihiko Abe, Takanori Takeno, Toshiyuki Takagi and Takeshi Sato (Tohoku University)

No. 9

Unsteady Aerodynamic Characteristics of Wings in Ground Effect
by Takahisa Matsuzaki, Shuya Yoshioka, Takuma Kato and Yasuaki Kohama (Tohoku University)

No. 10

LDV measurements of Unsteady Blade Suction-Surface Flow of an Axial-Flow Turbine Rotor
by Takayuki Matsunuma (AIST)

No. 11

Tonal noise from a symmetrical airfoil at low Reynolds number
by S. Rikitake (Gakushuin University), S. Takagi (JAXA) and T. Kamono (Gakushuin University)

No. 12

Observation of the feedback loop associated with airfoil trailing-edge noise
by Yasufumi Konishi and Shohei Takagi (JAXA)

No. 13

Observation of absolute instability behind symmetrical airfoils at low Reynolds numbers
by T. Kamono (Gakushuin University), S. Takagi, N. Itoh (JAXA) and S. Rikitake
(Gakushuin University)

No. 14

Momentum and energy transfer characteristics in nanoscale Couette flow and at solid-liquid
boundaries
by Daichi Torii and Taku Ohara (Tohoku University)

No. 15

A Numerical Analysis of Aerofoil Flutter in Ground Effects
by Takayuki Kawahara, Masanori Kikuchi and Kimitaka Hirano (University of Miyazaki)

No. 16

Application of silica gels for environmental protection
by Kazunori Nobuhara, Yoshiyuki Fueda , Keiji Ashitaka and Masami Chimura (Fuji Silysia
Chemical Ltd.)

No. 17

Vortices induced by small life
by Osamu Mochizuki (Toyo University)

CONTENTS

The detailed structure of randomization process of free shear layers	1
Institute of Flow Research H. Sato, H. Saito, H. Nakamura	
Statistical mechanics of turbulence based on cross-independence closure hypothesis	5
Kyoto University T. Tatsumi	
Introduction of towing wind tunnel facility in Sunrise Beach Research Facility	9
Tohoku University S. Yoshioka, T. Kato, Y. Kohama	
Recent developments in turbulent flow control	11
University of Nottingham K.-S. Choi, T.N. Jukes	
AIST T. Segawa, H. Yoshida	
Large-eddy simulation of transition in wall-bounded flow	13
KTH P. Schlatter	
Philip Morris Research & Development S. Stolz	
ETH Zurich L. Kleiser	
On the Concept of Hydraulically Smooth Wall	17
The University of Western Ontario J. M. Floryan	
Early times of fluid mechanics in Japan	21
Chern Institute of Mathematics T. Kambe	
An investigation on airfoil tonal noise generation	25
NLR M. Tuinstra	
JAXA T. Atobe, S. Takagi	
Detailed flow field around a leading-edge slat at low Reynolds numbers	27
Tokyo Metropolitan University S. Makiya, A. Inasawa	
M. Asai	
Flow Control with Pitching Motion of UAV using MEMS Flow Sensors	31
Osaka Prefecture University H. Tokutake, S. Sunada	
J. Fujinaga, Y. Ohtsuka	
Measurements of mass flux and concentration	35
in supersonic air/helium mixing by hot-wire anemometry	
Osaka Prefecture University A. Kondo, S. Sakaue, T. Arai	

On the critical Reynolds number of the drag coefficient for a circular cylinder	39
Gifu University T. Matsui	
Numerical simulations of flow past a 2-D airfoil at a low Reynolds number	41
JAXA T. Ikeda, T. Kurotaki	
T. Sumi, S. Takagi	
The velocity distribution around aerofoil for wing in ground effect	45
Gifu University S. Kikuchi, Y. Kozato	
S. Imao, H. Mitsui	
Experiments at the Sunrise-Beach Research Facility of the aerodynamic characteristics on ground effects of aerofoils with a secondary aerofoil	47
Miyakonojo National College of Technology Y. Takahashi	
University of Miyazaki M. Kikuchi, K. Hirano, T. Yuge, T. Moriya	
Tohoku University Y. Kohama	
Friction wear properties between partially polished CVD diamond and structural steel	51
Tohoku University H. Miki, N. Yoshida, T. Abe	
T. Takeno, T. Takagi	
Unsteady aerodynamic characteristics of wings in ground effect	53
Tohoku University T. Matsuzaki, S. Yoshioka	
T. Kato, Y. Kohama	
LDV measurements of unsteady blade suction-surface flow of an axial-flow turbine rotor	57
AIST T. Matsunuma	
Observation of the feedback loop associated with airfoil trailing-edge noise	61
JAXA Y. Konishi, S. Takagi	
Momentum and energy transfer characteristics in nanoscale Couette flow and at solid-liquid boundaries	65
Tohoku University D. Torii, T. Ohara	
A numerical analysis of aerofoil flutter in ground effects	67
University of Miyazaki T. Kawahara, M. Kikuchi	
K. Hirano	

The detailed structure of randomization process of free shear layers

H.Sato, H.Saito and H.Nakamura

Institute of Flow Research,Tokyo

ABSTRACT

The free shear layer is suitable for understanding the basic mechanism of randomization. Sound from a loud-speaker was used for introducing ordered velocity fluctuation in the layer. Three kinds of shear layer were tested and compared. A quantitative expression of the degree of randomness was accomplished by the elementary-wave analysis. The concept of neighbor randomness was introduced for another way of describing randomization. The randomization process of three shear layers does not show any significant difference.

Key Words: Free Shear Layers, Randomization.

0 .Introduction

The laminar-turbulent transition is a very important problem in the fluid dynamics. The detailed structure of the transition is still not understood.. The most important at present is how to express the degree of the randomness. This paper is one answer to this question.

1. Flow Field

Among three layers we concentrate on the separated layer. Other two layers will be compared at the end.

A 40-mesh metal screen of which width is 40 mm was placed in the test section of 25 cm x25 cm wind tunnel. Fig 1 is the mean-velocity distribution at 30

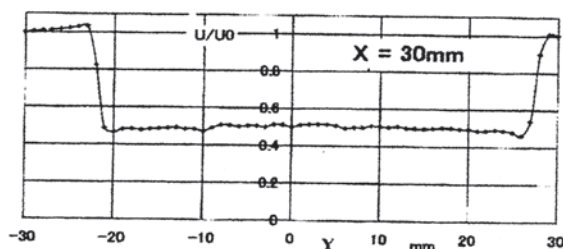


Fig 1 mean-velocity distrubution of separated layer

mm from the screen. The mean-flow velocity is 4 m/s. The shear layer was excited by the sound from a loud speaker placed near the test section. The frequency of sound is 270 Hz. It is clearly shown that two separated layers are formed at two ends of the screen. The randomization is achieved before two separated layers meet downstream. Thus we are making experiment in the single separated layer.

2.Wave Form

The wave form of velocity fluctuation obtained by
 $X = 100 \text{ mm}$ $Y = -25 \text{ mm}$

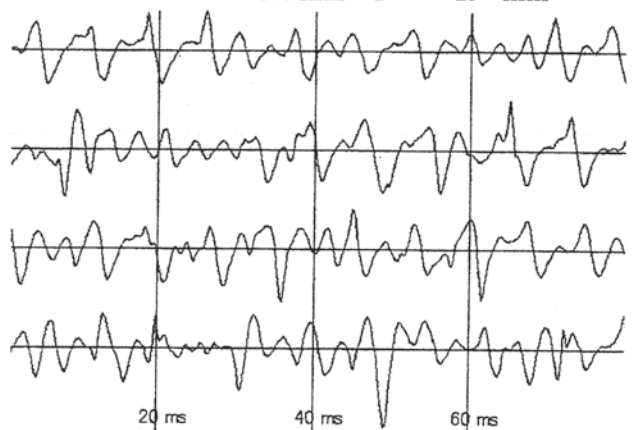


Fig 2 Wave Form

a hot-wire anemometer is shown in figs 2 and 3. The wave form in figure 2 shows some periodicity as well as random components. At $x = 200$ mm the wave form is almost random. This means that the randomization process ends before the $x -$ station.

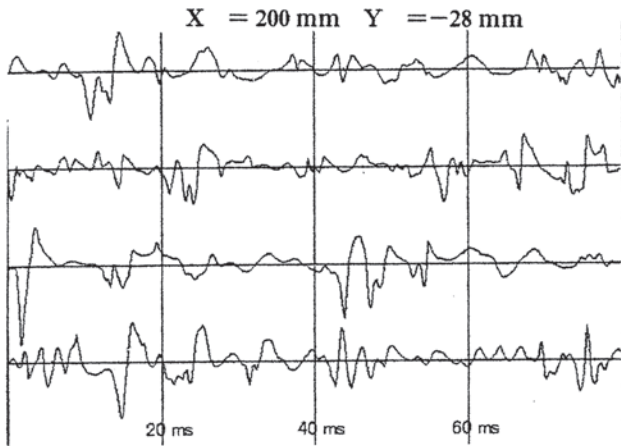


Fig 3 Wave Form

3. spectrum

The energy spectrum of u -fluctuation is taken by FFT process. Figures 4 and 5 are examples. Figure 4 shows some sharp peaks. It means that line components still remains.

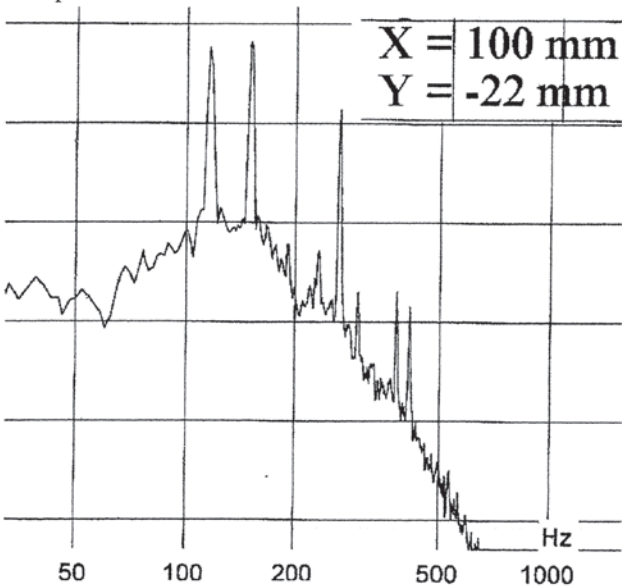


Fig 4 Spectrum

At $X=200$ mm the spectrum is smooth and continuous. It means that a turbulent separated layer is formed here.

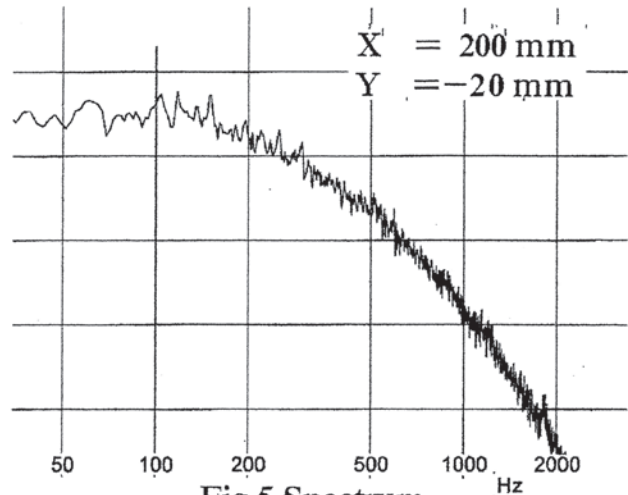


Fig 5 Spectrum

4. elementary-wave analysis

The energy spectrum is useful for detecting the end of randomization process but it does not give any quantitative information of the randomness.

We here propose a new method of analyzing the wave form directly. It is called elementary-wave analysis. The wave form is analyzed piece by piece as shown in fig 6. The wave length and amplitude of each wave is obtained by a small computer, and registered into the memory. Each wave length and amplitude was normalized by the average and expressed on the wave length and amplitude axis by small circles as shown in fig 7.

The wave form at $x = 75$ mm is close to sinusoidal

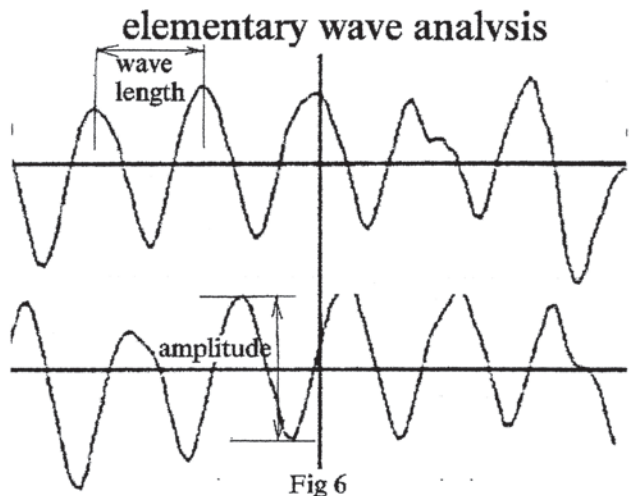


Fig 6

Therefore small circles gather around (1,1) point. The average distance from (1,1) is multiplied by

100 and defined as the random number. Figure 7 indicates that the average is 22.76. This number is an indication of randomness. This value is small and far

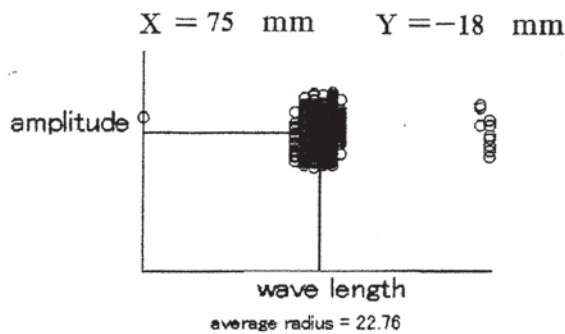


Fig 7

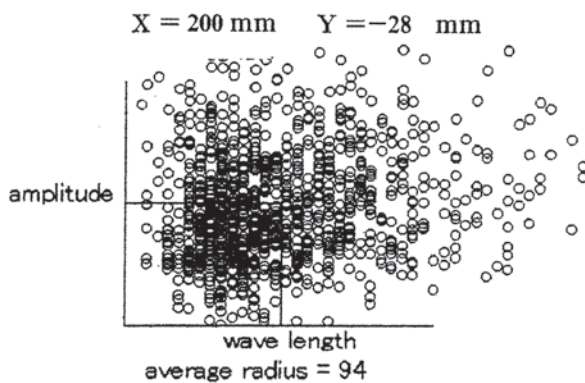


Fig 8

from being random.

Figure 8 shows at X = 200 mm. It is clear that small circles scatter in a wide space and average radius is 94 which indicates a turbulent layer is formed. There is no positive reasoning about the border of being turbulent. This fact is essential to the randomization process. No body can clearly distinguish the border between turbulent and non-turbulent region.

Fig 9 shows the streamwise variation of randomness number. If we assume the border of randomization as 90, it is accomplished between x = 150 and 200.

The Y-distribution of randomness number is not uniform. It seems that the randomization is late near the center line. It should be emphasized here that the results of randomization is poorly reproducible. It seems convincing that the randomization takes place randomly. If it is not so, the process is self

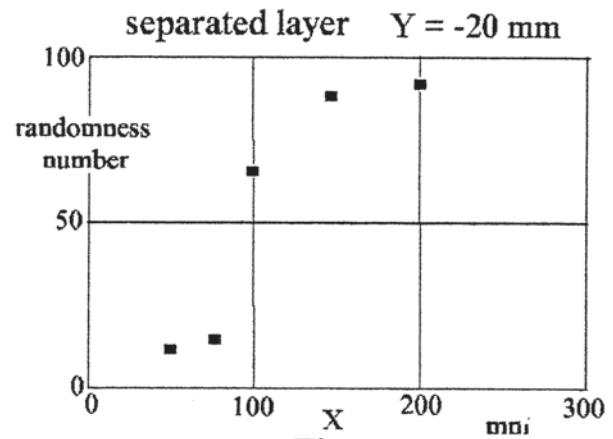


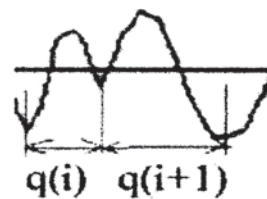
Fig 9

contradictory.

5. Neighbor Randomness

Other feature of randomization is the permutation problem. It is to seek the way of appearance. The random number or dice casting is one of randomness. Each trial is independent and one can easily calculate the probability. This is one of randomness. The turbulent flow is governed by the continuity relation and equation of motion. The appearance of next number can not be independent of the preceding wave.

neighbor randomness



$$= \sum_{i=1}^N \frac{|q(i+1) - q(i)|}{q(i+1) + q(i)} \cdot \frac{100}{N}$$

Fig 10

Fig 10 is the definition of neighbor randomness. It is nothing but summing up of difference of two

neighboring waves. It is clear that for sinusoidal wave the randomness is zero. As moving downstream the randomness increases and eventually it may reach 100.

Fig 11 shows calculated neighbor randomness at

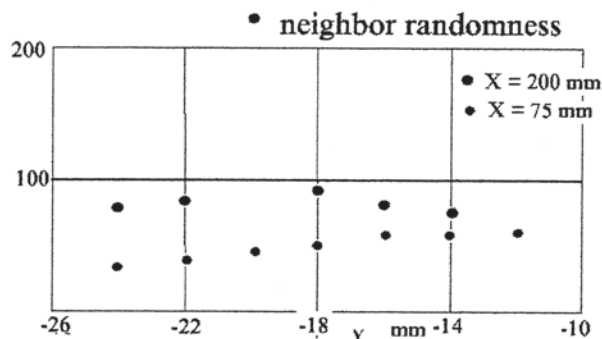


Fig 11

two x-stations. The neighbor randomness is small at small x and reach around 40 at $x = 200$ mm. This is obviously another expression of randomness.

6 . primary- wave analysis spectrum

It is possible to make some statistics based on the primary analysis. It is number of waves accumulated according to the wave length. The vertical scale is in logarithmic.

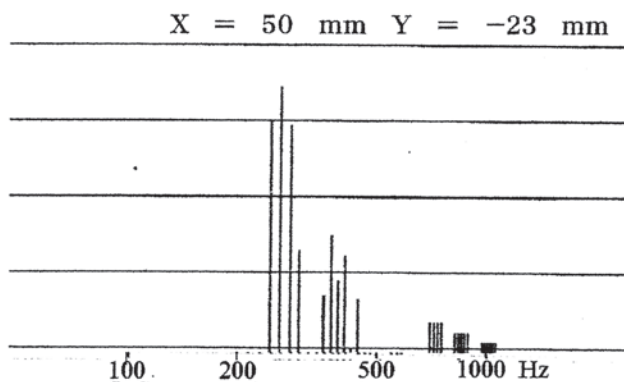


Fig 12

Fig 12 shows an example of the spectrum at relatively upstream position. The concentration of spectrum is clearly observed between 200 and 500 Hz.

Fig 13 shows spectrum at larger x . Many spectral components are formed in lower as well as higher frequency range. It is similar to the energy spectrum.

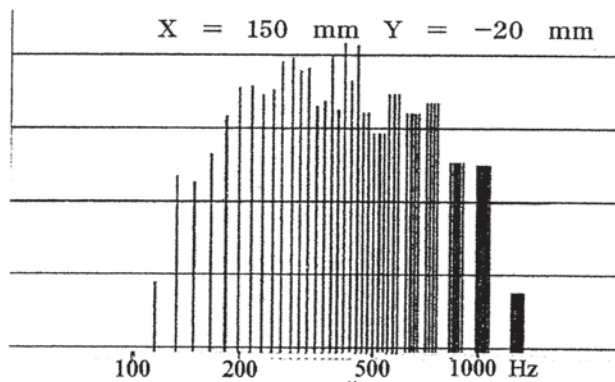


Fig 13

7 . Comparison with other shear flows

Experiments were made with a narrow screen, width being 4 mm. In this case two separated layer meets before they are randomized. the randomization process is more complicated. Accordingly, the randomization is a little slower than the separated layer. Another flow is the wake of a flat plate placed parallel to the flow. In this case there is no separation and a symmetrical laminar wake is formed at the trailing edge. This wake seems to be slow in the randomization process.

Generally speaking, there is no essential difference among these three shear flows. The turbulent wakes also show no significant differences.

8 . conclusion

The following conclusions were obtained

1. The quantitative description of the degree of randomness became possible by the introduction of the primary -wave analysis.
2. The poor reproducibility of randomization process was clearly observed.
3. The turbulent flows made in three different free shear layers are more or less similar.
4. The primary-wave spectrum is another indication of randomness. It shows similar nature as energy spectrum.

Statistical mechanics of turbulence based on cross-independence closure hypothesis

Tomomasa Tatsumi

Kyoto University and International Institute for Advanced Studies

ABSTRACT

A new approach to statistical mechanic of turbulence based on the cross-independence closure hypothesis is presented and its relationship with Kolmogorov's theory of locally isotropic turbulence is discussed.

For homogeneous isotropic turbulence, the one-point velocity distribution is obtained as the inertial normal distribution N1 with the parameter $\alpha = \varepsilon/3$, ε being the energy-dissipation, and no viscosity ν . The energy-dissipation ε satisfies the fluctuation-dissipation theorem and causes the inviscid energy catastrophe $E > 0$ in the limit of $\nu \rightarrow 0$. Since no energy supply is assumed for homogeneous turbulence, the energy E decays in time t as $E \propto t^{-1}$ and hence $\varepsilon \propto t^{-2}$. Two-point velocity distribution is expressed in terms of the velocity-sum distribution and the velocity-difference distribution, and the latter distributions are expressed as another inertial normal distribution N2 with the parameter $\alpha/2$ for $r > 0$, r being the distance of the two points. Although these distributions change discontinuously at $r = 0$ for satisfying the boundary conditions, they are continuous functions of the local coordinate $r^* = r/\eta$, $\eta = (\nu^3/\varepsilon)^{1/4}$ being Kolmogorov's length. In the local range, the velocity-sum distribution is expressed as the local normal distribution N3 with the self-energy-dissipation $\alpha^*(r^*)$ for the velocity-sum as the parameter. The velocity-difference distribution in the local range is axisymmetric with respect to the vector r^* , and the lateral component is expressed as the (one-dimensional) local normal distribution N4 with the self-energy-dissipation $\alpha^*(r^*)$ for the velocity-difference as the parameter. The longitudinal velocity-difference distribution in the local range is obtained as algebraic non-normal distributions A1 and A2 for the inertial and viscous subranges respectively.

For inhomogeneous turbulence, the velocity is decomposed into the mean velocity and the fluctuation velocity around it, and the equations for the mean velocity and the distributions of the one- and two-point fluctuation velocities are derived. The general characters of the equations are discussed with systematic application to inhomogeneous turbulence in scope.

Key Words: Homogeneous isotropic turbulence, inhomogeneous turbulence, cross-independence closure hypothesis, inertial-normal distributions, self-energy and self-energy-dissipation

1. Introduction

In spite of great developments in turbulence research during the last half a century since Kolmogorov's epoch-making work [1], theory of turbulence seems still lacking in the total consistency, statistical theories being mainly concerned with small-scale components of turbulence, while large-scale components mostly left to numerical analysis. The present approach intends to deal with large and small components of turbulence on

equal footing by making use of the Lundgren-Monin equations for the velocity distributions [2,3] together with the cross-independence closure hypothesis proposed by Tatsumi [4].

2. Velocity Distributions

Turbulence is governed by the Navier-Stokes equation,

$$\frac{\partial \mathbf{u}}{\partial t} + (\mathbf{u} \cdot \nabla) \mathbf{u} - \nu \nabla^2 \mathbf{u} = - (1/\rho) \nabla p / \partial \mathbf{x}, \quad (1)$$

and the non-divergence condition,

$$(\partial/\partial \mathbf{x}) \cdot \mathbf{u} = 0, \quad (2)$$

for the velocity $\mathbf{u}(\mathbf{x}, t)$ and the pressure $p(\mathbf{x}, t)$, where ρ and ν denote the density and the kinetic viscosity.

If we take the velocities at two points $\mathbf{u}_1 = \mathbf{u}(\mathbf{x}_1, t)$ and $\mathbf{u}_2 = \mathbf{u}(\mathbf{x}_2, t)$, the one- and two-point velocity distributions are defined as

$$\begin{aligned} f(\mathbf{v}_1, \mathbf{x}_1, t) &= \langle \delta(\mathbf{u}_1 - \mathbf{v}_1) \rangle, \\ f^{(2)}(\mathbf{v}_1, \mathbf{v}_2; \mathbf{x}_1, \mathbf{x}_2; t) &= \langle \delta(\mathbf{u}_1 - \mathbf{v}_1) \delta(\mathbf{u}_2 - \mathbf{v}_2) \rangle, \end{aligned} \quad (3)$$

where \mathbf{v}_1 and \mathbf{v}_2 are the probability variables and the brackets $\langle \rangle$ denote the probability mean with respect to an initial distribution and δ the delta function. The higher distributions $f^{(n)}$, $n \geq 3$ can be defined accordingly.

3. Cross-independence closure hypothesis

The Lundgren-Monin equations are unclosed since the equation for $f^{(n)}$ includes the higher distribution $f^{(n+1)}$, and in order to make the equations solvable we have to introduce a *closure hypothesis* for expressing $f^{(n+1)}$ by the lower-order distributions.

A commonly used hypothesis is the *independence decomposition* of the distribution $f^{(2)}$ such that

$$f^{(2)}(\mathbf{v}_1, \mathbf{v}_2; \mathbf{x}_1, \mathbf{x}_2; t) = f(\mathbf{v}_1, \mathbf{x}_1, t) f(\mathbf{v}_2, \mathbf{x}_2, t). \quad (4)$$

Eq.(4) is known to be valid at large distance $r = |\mathbf{x}_2 - \mathbf{x}_1|$ but not at small distance r .

On the other hand, if we take the sum and difference of the velocities \mathbf{u}_1 and \mathbf{u}_2 as

$$\mathbf{u}_+ = (\mathbf{u}_1 + \mathbf{u}_2)/2, \quad \mathbf{u}_- = (\mathbf{u}_2 - \mathbf{u}_1)/2, \quad (5)$$

and consider the one- and two-velocity distributions of the cross-velocities $(\mathbf{u}_+, \mathbf{u}_-)$ as

$$\begin{aligned} g_+(\mathbf{v}_+; \mathbf{x}_1, \mathbf{x}_2; t) &= \langle \delta(\mathbf{u}_+ - \mathbf{v}_+) \rangle, \\ g^{(2)}(\mathbf{v}_+, \mathbf{v}_-; \mathbf{x}_1, \mathbf{x}_2; t) &= \langle \delta(\mathbf{u}_+ - \mathbf{v}_+) \delta(\mathbf{u}_- - \mathbf{v}_-) \rangle, \end{aligned} \quad (6)$$

$$\mathbf{v}_+ = (\mathbf{v}_1 + \mathbf{v}_2)/2, \quad \mathbf{v}_- = (\mathbf{v}_2 - \mathbf{v}_1)/2, \quad (7)$$

we can define the *cross-independence decomposition* of the distribution $f^{(2)}$ by

$$\begin{aligned} f^{(2)}(\mathbf{v}_1, \mathbf{v}_2; \mathbf{x}_1, \mathbf{x}_2; t) &= \{ \partial(\mathbf{dv}_+, \mathbf{dv}_-) / \partial(\mathbf{dv}_1, \mathbf{dv}_2) \} g^{(2)}(\mathbf{v}_+, \mathbf{v}_-; \mathbf{x}_1, \mathbf{x}_2; t) \\ &= 2^{-3} g^{(2)}(\mathbf{v}_+, \mathbf{v}_-; \mathbf{x}_1, \mathbf{x}_2; t). \end{aligned} \quad (8)$$

$$g^{(2)}(\mathbf{v}_+, \mathbf{v}_-; \mathbf{x}_1, \mathbf{x}_2; t) = g_+(\mathbf{v}_+; \mathbf{x}_1, \mathbf{x}_2; t) g_-(\mathbf{v}_-; \mathbf{x}_1, \mathbf{x}_2; t). \quad (9)$$

The validity of Eqs.(8) and (9) is proved for large and small r as well.

A close similarity may be noticed between this hypothesis and Kolmogorov's theory which assumes the independence of small eddies represented by $\Delta \mathbf{u} = \mathbf{u}_2 - \mathbf{u}_1$ from large eddies represented by \mathbf{u}_1 and \mathbf{u}_2 . Apart from this similarity, the two theories are rather different in the sense that turbulence is assumed to be steady and nearly homogeneous in Kolmogorov's theory while it is taken here to be unsteady and strictly homogeneous.

4. Inertial similarity of velocity distributions

In homogeneous turbulence, the energy

$$E(t) = (1/2) \sum_{i=1}^3 \langle (u_i(\mathbf{x}, t))^2 \rangle, \quad (10)$$

and the energy-dissipation rate

$$\varepsilon(t) = \nu \sum_{i,j=1}^3 \langle (\partial u_i / \partial x_j)^2 \rangle, \quad (11)$$

are related with each other by the equation,

$$dE(t)/dt = -\varepsilon(t). \quad (12)$$

Since there is no genuine length-scale nor time-scale in homogeneous turbulence, they must be expressed in terms of Kolmogorov's scales:

$$\text{length: } \eta = (\nu^3/\varepsilon)^{1/4}, \quad \text{time: } \tau = (\nu/\varepsilon)^{1/2}. \quad (13)$$

Then, the energy-dissipation rate $\varepsilon(t)$ is expressed in dimension as

$$[\varepsilon(t)] = [\nu] \times [\{ (\nu^3/\varepsilon)^{1/4} \tau^{-1} / (\nu^3/\varepsilon)^{1/4} \}^2] = [\nu] \times [\tau^{-2}], \quad (14)$$

where $[]$ denote the dimension.

Thus it follows from Eqs.(11), (12) and (14) that

$$\varepsilon(t) = \varepsilon_0 t^{-2}, \quad E(t) = E_0 t^{-1}, \quad (15)$$

where $\varepsilon_0 = E_0$ are constants of the dimension of ν . Eq.(15) gives the inverse-linear law for the energy-decay.

5. One-point velocity distribution

On substitution from Eqs.(8) and (9) into the Lundgren-Monin equation for the *one-point velocity distribution* f , we obtain the following closed equation for f :

$$[\partial/\partial t + \alpha(t)|\partial/\partial \mathbf{v}|^2] f(\mathbf{v}, t) = 0, \quad (16)$$

$$\alpha(t) = (2/3)\nu \lim_{r \rightarrow 0} |\partial/\partial \mathbf{v}|^2 \int |\mathbf{v}_-|^2 g_-(\mathbf{v}_-, \mathbf{r}, t) d\mathbf{v}_-, \quad (17)$$

with $\alpha(t) = \varepsilon(t)/3$. Eq.(16) is *inertial* in the sense that it is independent of the viscosity ν and Eq.(17) expresses the dissipation $\alpha(t)$ in terms of the variance of the fluctuation velocity \mathbf{u}_- .

The self-similar solution of Eq.(17) in accordance with Eq.(15) is obtained as

$$f(\mathbf{v}, t) = f_0(\mathbf{v}, t) \equiv (t/4\pi\alpha_0)^{3/2} \exp[-|\mathbf{v}|^2 t/4\alpha_0], \quad \alpha(t) = \alpha_0 t^{-2}. \quad (18)$$

with $\alpha_0 = \varepsilon_0/3$. Eq.(18) gives an inertial normal velocity distribution N1 for the one-point velocity distribution f .

The distribution N1 changes self-similarly in time t , starting from a uniform distribution with zero density at $t=0$, growing up as a normal distribution for $t>0$, and tending to the delta distribution representing the dead state for $t \rightarrow \infty$. During this process, the energy $E(t)$ decays as t^{-1} by the fluctuation dissipation (17).

6. Two-point velocity distributions

The equation for the *two-point velocity distribution* $f^{(2)}$ is derived by substituting the relations similar to Eqs. (8) and (9) into the Lundgren-Monin equation for $f^{(2)}$ as

$$\begin{aligned} & [\partial/\partial t + (\mathbf{v}_2 - \mathbf{v}_1) \cdot \partial/\partial \mathbf{r} + \alpha(t)(|\partial/\partial \mathbf{v}_1|^2 + |\partial/\partial \mathbf{v}_2|^2) \\ & - \{ \partial/\partial \mathbf{v}_1 \cdot \partial/\partial \mathbf{x}_1 \beta_1(\mathbf{v}_1, t) + \partial/\partial \mathbf{v}_2 \cdot \partial/\partial \mathbf{x}_2 \beta_2(\mathbf{v}_2, t) \}] \times \\ & \times f^{(2)}(\mathbf{v}_1, \mathbf{v}_2; \mathbf{r}, t) = 0, \end{aligned} \quad (19)$$

where

$$\begin{aligned} \beta_1(\mathbf{v}_1, t) &= (1/4\pi) \int |\mathbf{r}'|^{-1} ((\mathbf{v}_1 + 2\mathbf{v}') \cdot \partial/\partial \mathbf{r}')^2 g_-(\mathbf{v}', \mathbf{r}', t) d\mathbf{v}' d\mathbf{r}', \\ \beta_2(\mathbf{v}_2, t) &= (1/4\pi) \int |\mathbf{r}''|^{-1} ((\mathbf{v}_2 + 2\mathbf{v}'') \cdot \partial/\partial \mathbf{r}'')^2 g_-(\mathbf{v}'', \mathbf{r}'', t) d\mathbf{v}'' d\mathbf{r}''. \end{aligned} \quad (20)$$

The distribution $f^{(2)}$ is expressed in terms of the distributions g_+ and g_- , whose equations are obtained as

$$[\partial/\partial t + (1/2)\alpha(t)|\partial/\partial \mathbf{v}_+|^2] g_+(\mathbf{v}_+, \mathbf{r}, t) = 0, \quad (21)$$

$$\begin{aligned} & [\partial/\partial t + (1/2)\alpha(t)|\partial/\partial \mathbf{v}_-|^2 + 2\mathbf{v}_- \cdot \partial/\partial \mathbf{r} \\ & + (1/2)\partial/\partial \mathbf{v}_- \cdot \{ \partial/\partial \mathbf{x}_1 \beta_1(\mathbf{v}_-, t) - \partial/\partial \mathbf{x}_2 \beta_2(\mathbf{v}_-, t) \}] \times \\ & \times g_-(\mathbf{v}_-, \mathbf{r}, t) = 0. \end{aligned} \quad (22)$$

6.1. Velocity-sum distribution

The *velocity-sum distribution* g_+ is obtained from Eq. (21) as another inertial normal distribution N2, having half a variance of N1.

$$g_+(\mathbf{v}_+, \mathbf{r}, t) = g_0(\mathbf{v}_+, t) \equiv (t/2\pi\alpha_0)^{3/2} \exp[-|\mathbf{v}_+|^2 t/2\alpha_0], \quad (23)$$

6.2. Velocity-difference distribution

Though Eq.(22) is r -dependent, the change takes place in the local range of $O(\eta)$. Hence, for small values of v , the *velocity-difference distribution* g_- is expressed by the solution of the r -independent part of Eq.(22) as

$$g_-(\mathbf{v}_-, \mathbf{r}, t) = g_0(\mathbf{v}_-, t) \equiv (t/2\pi\alpha_0)^{3/2} \exp[-|\mathbf{v}_-|^2 t/2\alpha_0], \quad (24)$$

which is the inertial normal distribution N2.

6.3. Inertial similarity and local similarity

Although the distributions g_+ and g_- expressed by Eqs. (23) and (24) are r -independent, they must satisfy the boundary conditions for $r \rightarrow 0$,

$$g_-(\mathbf{v}_-, 0, t) = f_0(\mathbf{v}_1, t), \quad g_-(\mathbf{v}_-, 0, t) = \delta(\mathbf{v}_-), \quad (25)$$

which is required by the conditions $\mathbf{v}_+ \rightarrow \mathbf{v}_1$ and $\mathbf{v}_- \rightarrow 0$ in this limit. Such discontinuous changes of g_+ for $r \rightarrow 0$ are due to the *inertial similarity*, but actually the changes should occur continuously in the finite *local range* for the finite viscosity $\nu > 0$. (see [5])

7. Local similarity of velocity distributions

In the local range, the velocity distributions are dealt with in terms of the local variables based on Kolmogorov's length and time (13) and indicated by *. [6]

7.1. Velocity-sum distribution

Eq.(21) written in the local variables is solved to give

the *velocity-sum distribution* g_+ as the local normal distribution N3,

$$\begin{aligned} g_+(\mathbf{v}_+, \mathbf{r}^*, t^*) &= (t^*/4\pi\alpha_{+0}^*(r^*))^{3/2} \exp[-|\mathbf{v}_+|^2 t^*/4\alpha_{+0}^*(r^*)], \\ \alpha_{+0}^*(r^*, t^*) &= \alpha_{+0}^*(r^*) t^{*-2}, \end{aligned} \quad (26)$$

where $\varepsilon_{+0}^*(r^*, t^*) = 3\alpha_{+0}^*(r^*, t^*)$ represents the dissipation of the *self-energy* $E_{+0}^*(r^*, t^*) = \langle |\mathbf{u}_{+0}^*(\mathbf{x}^*, \mathbf{r}^*, t^*)|^2 \rangle / 2$.

7.2. Lateral velocity-difference distribution

In the local range, the *velocity-difference distribution* g_- is axisymmetric and composed of the lateral distribution g_{\perp} and the longitudinal distribution g_{\parallel} .

For the *lateral distribution* g_{\perp} , Eq.(22) written in the local variables reduces to the \mathbf{r}^* -independent form and its solution is obtained as the (one-dimensional) local normal distribution N4,

$$\begin{aligned} g_{\perp}(\mathbf{v}_{\perp}^*, \mathbf{r}^*, t^*) &= (t^*/4\pi\alpha_{\perp 0}^*(r^*))^{1/2} \exp[-\mathbf{v}_{\perp}^{*2} t^*/4\alpha_{\perp 0}^*(r^*)], \\ \alpha_{\perp 0}^*(r^*, t^*) &= \alpha_{\perp 0}^*(r^*) t^{*-2}, \end{aligned} \quad (27)$$

where $\varepsilon_{\perp 0}^*(r^*, t^*) = 3\alpha_{\perp 0}^*(r^*, t^*)$ represents the *dissipation* of the *self-energy* $E_{\perp 0}^*(r^*, t^*) = \langle |\mathbf{u}_{\perp 0}^*(\mathbf{x}^*, \mathbf{r}^*, t^*)|^2 \rangle / 2$.

7.3. Longitudinal velocity-difference distribution

Eq.(22) for the *longitudinal distribution* g_{\parallel} is simplified by localizing the non-local parameters β_1 and β_2 and solved assuming the space-similarity of the solution in the subranges of the local range.

$$\begin{aligned} g_{\parallel}(\mathbf{v}_{\parallel}^*, \mathbf{r}^*, t^*) &= t^{*1/2} (r^* t^{*-1/2})^{-\theta} H(\xi), \quad \xi = t^{*1/2} (r^* t^{*-1/2})^{-\theta} \mathbf{v}_{\parallel}^*, \\ \alpha_{\parallel 0}^*(r^*) &= \alpha_{\parallel 0}^*(r^*) t^{*-1/2} 2\theta, \end{aligned} \quad (28)$$

where θ is the parameter characterizing each subrange.

Intermediate subrange

The distribution is obtained as the *inertial normal distribution* N5,

$$H(\xi) = H_0(\xi) \equiv (4\pi\alpha_{\parallel 0}/(1+\theta))^{-1/2} \exp[-((1+\theta)/4\alpha_{\parallel 0})\xi^2], \quad (29)$$

with $0 \leq \theta \leq 1/3$, 0 corresponding to the outer boundary and 1/3 to the inner boundary. The distribution N5 is shown graphically in Fig.1 in standard form.

Inertial subrange

The distribution is obtained as the *inertial algebraic distribution* A1,

$$H(\xi) = H_c(\xi) \equiv 12\pi\alpha_{\parallel 1/3}^2 (\xi^2 + 4a_{1/3})^{-5/2}. \quad (30)$$

with $\theta = 1/3$. The distribution A1 has algebraic tails $|\xi|^{-5}$ for $|\xi| \rightarrow \infty$ and hence divergent moments for $n \geq 4$. The distribution A1 is shown graphically in Fig.1,

Viscous subrange

The distribution is obtained by solving the equation,

$$\{1-(10/3)\xi\}H + \xi\{1-(14/3)\xi\}H' + (9/128)\{1-(8/3)\xi - (256/27)\xi^3\}H'' = 0, \quad (31)$$

with $\theta=1$, $a_1=9/128$. The solution gives the viscous algebraic distribution A2 similar to A1. It also has the tails $|\xi|^{-5}$ for $|\xi| \rightarrow \infty$ and divergent moments for $n \geq 4$. The distribution A2 is shown graphically in Fig.1.

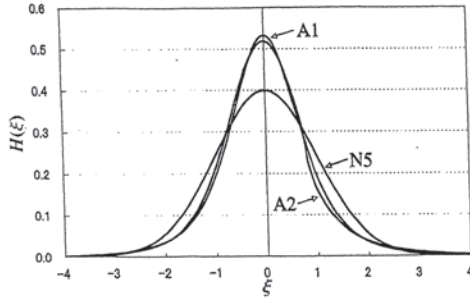


Fig.1 Longitudinal velocity-difference distributions in the local range shown graphically in standard form. N5: Inertial normal distribution (29). A1: Inertial algebraic distribution (30). A2: Viscous algebraic distribution obtained from Eq.(31).

8. Overview of homogeneous turbulence

An overview of the velocity distributions of *homogeneous turbulence* obtained here may be given by Fig.2, or the diagram of the cross-velocity variances $\langle u^{*2} \rangle$ (\square) and $\langle u^{*-2} \rangle$ (Δ) versus the distance r^* measured by Makita et al. [7]. The inertial normality of the distributions may be noted. The celebrated 2/3-power variance of Kolmogorov [1] is realized as the distribution A1 in the inertial subrange.

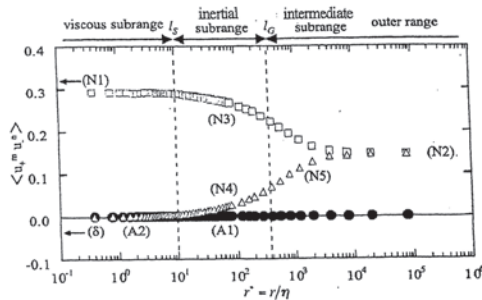


Fig.2 Overview of the two-point velocity distributions on the figure of the longitudinal cross-velocity correlations measured by Makita et al. [7] at $Re = 350$.

9. Extension to inhomogeneous turbulence

The present approach based on the cross-independence closure hypothesis is extended to inhomogeneous turbulence. The turbulent velocity $\mathbf{u}(\mathbf{x}, t)$ is decomposed into its mean $\langle \mathbf{u}(\mathbf{x}, t) \rangle$ and the fluctuation around the mean,

$$\mathbf{u} = \langle \mathbf{u} \rangle + \hat{\mathbf{u}}, \quad \langle \hat{\mathbf{u}} \rangle = \mathbf{0}. \quad (32)$$

9.1. Equations for velocity distributions

On substitution from (32) to Eqs.(1) and (2), we obtain the equations of motion for the mean velocity $\langle \mathbf{u} \rangle$ and the fluctuation velocity $\hat{\mathbf{u}}$. The equations for the distributions of the one-point velocity, the velocity-sum, and the velocity-difference are derived from these equations following the way employed for deriving Eqs.(16),(19), (21), (22) for homogeneous isotropic turbulence. For the details omitted here by the page limitation, see [8].

9.2. General characters of the equations

No need for *ad hoc* assumptions

It should be noted that the above-mentioned equations for the velocity distributions is self-contained and needs no *ad hoc* assumptions but for some simplifications.

Kolmogorov's local isotropy hypothesis

It is also to be noted that the equations for the fluctuation velocity distribution include the mean velocity $\langle \mathbf{u} \rangle$ only in the transfer terms so that the viscous dissipation is not influenced by the mean flow. This verifies Kolmogorov's assumption of the local isotropy.

Turbulent energy dissipation

The equations include the viscous terms as

$$[-\nu |\partial/\partial \mathbf{x}|^2 + \alpha(\mathbf{x}, t) |\partial/\partial \mathbf{v}|^2] f(\mathbf{v}, \mathbf{x}, t) \quad (33)$$

and similar terms in other distributions where $\alpha(\mathbf{x}, t)$ is equivalent to $\alpha(t)$ in (17). Eq.(33) clearly indicates that the turbulent dissipation is caused by the counter diffusion in the velocity space $|\partial/\partial \mathbf{v}|^2$ and not by any spatial diffusion $-\nu |\partial/\partial \mathbf{x}|^2$ with a "turbulent viscosity".

References

1. Kolmogorov AN (1941) Dokl Akad Nauk SSSR **30**: 301-305.
2. Lundgren TS (1967) Phys Fluids **10**: 969-975.
3. Monin AS (1967) PMM J Appl Math Mech **31**: 1057-1068.
4. Tatsumi T (2001) In: Kambe T et al. (eds) Geometry and Statistics of Turbulence. Kluwer Acad. Pub. Dordrecht:3-12.
5. Tatsumi T et al.(2004) Fluid Dyn Res **35**:123-158.
6. Tatsumi T et al.(2007) Fluid Dyn Res **39**:221-266.
7. Makita H et al.(2005) JAXA Spec.Pub.04-002:71-74.
8. Tatsumi T (2007) JAXA Spec.Pub. 06-013:49-52.

Introduction of Towing Wind Tunnel Facility in Sunrise Beach Research Facility

S. Yoshioka^{*}, T. Kato^{*}, and Y. Kohama^{*}

^{*} Institute of Fluid Science, Tohoku University

ABSTRACT

In this paper a newly constructed Towing wind tunnel facility is introduced. This Towing wind tunnel system can create highly complex flow and zero free stream turbulence condition. The performance of this facility is first explained. The results of our first experiment on the boundary layer transition on a flat plate are then given. We concluded that this facility has good performance for complex flow testing under very low freestream turbulence condition.

Key Words: Towing wind tunnel, free stream turbulence, Boundary-Layer transition

1. Introduction

Fluid dynamics experiments have ever been done using wind tunnel. Highly complex flow such as flow between steady surface and moving obstacle is, however, hardly realize in this kind of conventional wind tunnel. It is also hardly realize the zero free stream turbulence condition. These two major fundamental problems make wind tunnel difficult to re-create actual flow condition.

To solve the first problem mentioned above, such as to re-create flow under a moving automobile on the ground and flow around an airplane taking off and touching down in the wind tunnel, we often use a moving belt system set up in the bottom wall of the wind tunnel. This moving belt, however, always generates wall vibration and electric noise which interfere the measurement especially in the region close to the wall. As to the second problem mentioned above, fan certainly generates free stream turbulence. This is fundamentally impossible to avoid. The moving belt also generates turbulence which level is not negligible.

In this paper the development of towing wind tunnel, that may fundamentally solve above mentioned problems is reported. Some first results of experiments of boundary layer transition using this facility is then explained.

2. Towing Wind Tunnel

We have built 7 km long testing line in Sunrise beach research facility of Tohoku University in Hyuga city, Miyazaki, Japan in 2003. In the first 2 km out of total 7 km we constructed a testing track of the towing wind tunnel. A schematic of this facility is shown in Fig. 1. The first 910 m is accelerating region, the next 515 m is the measuring region and the final 475 m is the decelerating region. In this track an electrically driven vehicle runs, see Fig. 2. We named this facility

as HART which stands for Hyuga Aerodynamic Research facility by Towing. We call the vehicle as HART vehicle.

The measuring region is covered by FRP hood in which acoustic material was installed to avoid external noise. In this hood ventilators and lighting facilities are set up. This HART vehicle has 8 tires underneath its body to run, and 4 side tires to guide. 4 tires out of 8 tires underbody was electrically driven. 4 side tires are forced to touch guide walls by springs. At the nose of this HART vehicle an arm supported by hydraulic pressure actuators is equipped. On the tip of this arm an testing model is set. The vibration of the this arm is minimized by the actively controlled hydraulically operated actuator. The acceleration and deceleration rates are 0.15G and -0.45G. The maximum speed of this HART vehicle is 50 m/s. This HART vehicle is radio controlled from the control room beside the testing track

3. Experiments

3.1 Performance test

In Fig. 3 the ground speed and air speed measured by a pitot tube and two hotwires set up on the arm of the HART vehicle are shown. The experiment speed was set at 37.5 m/s as a ground speed. In the middle of the accelerating region the ground speed reached to 37.5 m/s. In the measuring region the air speed is decreasing. As a whole, the air speed is slightly slower as compared with the ground speed. This may be because the HART vehicle drives air around the vehicle itself. This trend is remarkably found in the measuring region. It is inferred that the vehicle pushes out the air inside of the measurement region to the exit direction. As a result, in the exit region of the hood the air speed is slower roughly 10% than the ground speed.

3.2 Boundary-layer transition measurement

In the next stage we replaced the arm on the HART vehicle by a vertical flat plate, see Fig. 4, and tried to measure the boundary layer transition on this flat plate. We put a single hot wire sensor 1 mm away from the surface of the flat plate. We measured velocity signals changing the streamwise location of this sensor keeping the vehicle ground speed constant, 45 m/s to see their Reynolds number dependence.

Fig. 5 shows the obtained velocity signals. Signals in Fig. 5 are representative signals measured in laminar ($Re=1.6 \times 10^6$), intermittent ($Re=2.4 \times 10^6$, 3.2×10^6) and turbulent ($Re=9.2 \times 10^6$) boundary layers. In the signals measured in the intermittent boundary layer ($Re=2.4 \times 10^6$, 3.2×10^6), the passage of the turbulent spots are clearly observed as a positive spike.

The transitional Reynolds number Re_{tr} where the intermittency factor falls to 0.5 is determined as $Re_{tr} \sim 4.0 \times 10^6$. It can be therefore concluded that the free stream turbulence of HART facility is extremely low and boundary layer transition occurs at higher Reynolds number.

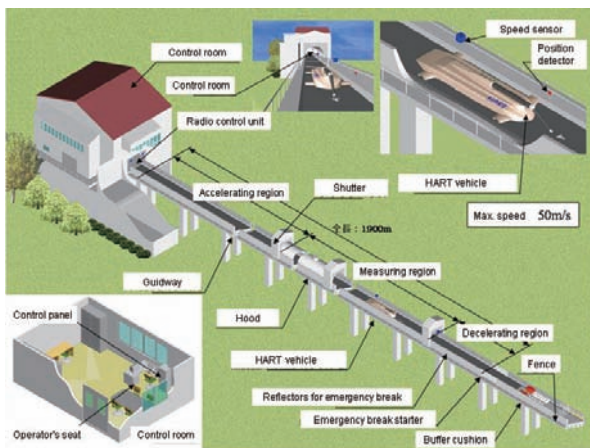


Fig. 1 Schematic view of HART, towing wind tunnel facility



Fig. 2 HART vehicle running in the measuring region

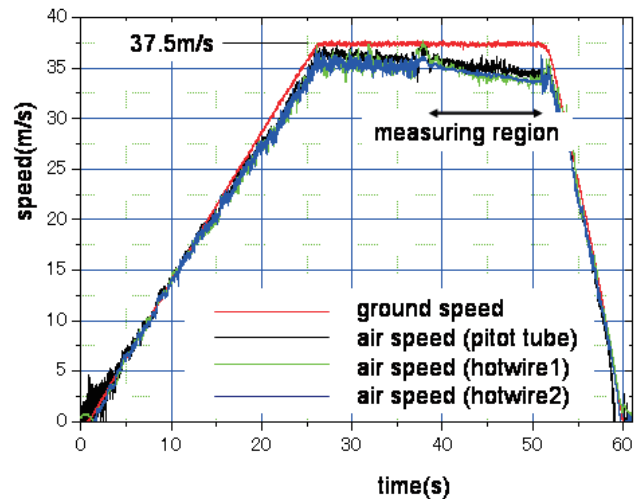


Fig. 3 Comparison of ground and air speed of HART vehicle

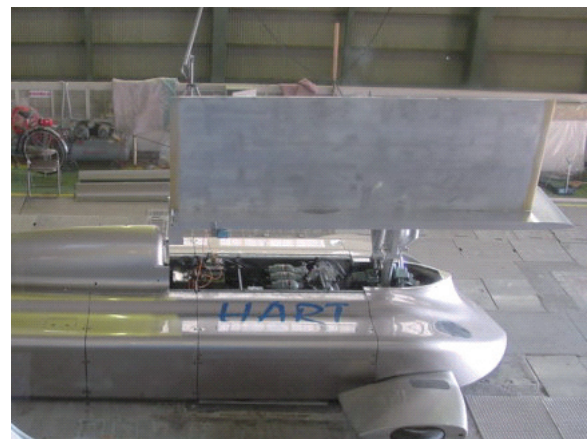


Fig. 4 Vertically installed flat plate on HART vehicle

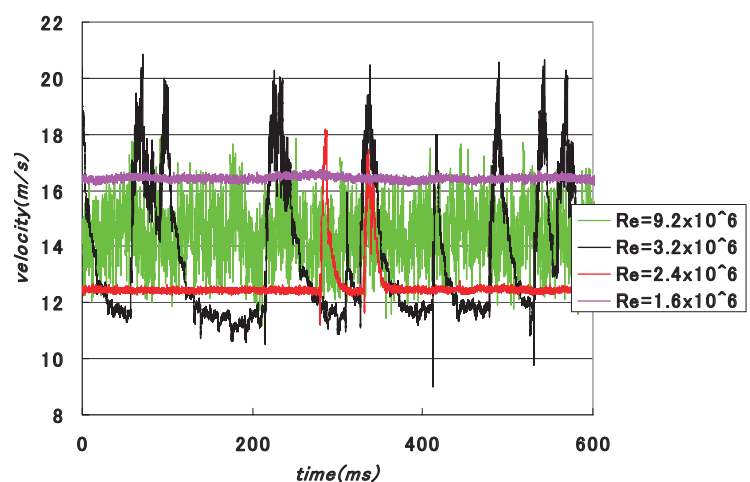


Fig. 5 Measured velocity signals

Recent Developments in Turbulent Flow Control

K.-S. Choi, T.N. Jukes
University of Nottingham, Nottingham, UK

T. Segawa, and H. Yoshida
National Institute of Advanced Industrial Science and Technology, Tsukuba, Japan

ABSTRACT

Recent developments in turbulent flow control are discussed through a presentation of experimental results from wind tunnel tests which have been carried out at the University of Nottingham in collaboration with AIST. A particular emphasis is given to the use of surface plasma for controlling turbulent boundary layers for skin-friction reduction, delaying or reattaching flow separation and enhancing flow mixing.

Key Words: Turbulent flows, drag reduction, separation control, surface plasma

1. Introduction

Surface plasma is an emerging technique in active flow control, which has unique ability to create a body force close to the wall in atmospheric pressure air. The actuators based on surface plasma principle are simple, lightweight, require no moving parts, and are extremely fast acting.

2. Surface Plasma Actuators

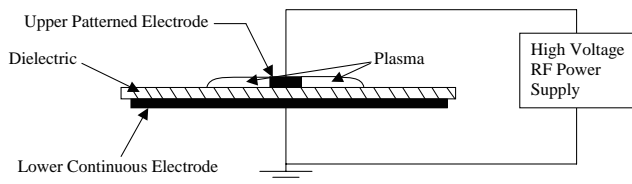


Fig. 1 Symmetric surface plasma actuator.

The electrode layout of surface plasma actuators consists of a pair of electrodes - one patterned and one usually continuous - separated by a dielectric layer (Fig. 1), across which a pulsed or oscillatory voltage is applied. Typical excitation is at several kHz and several kV. Electrode sheets that have been used here are made from Mylar, with a typical thickness in the 125-250 μ m range, double-sided with copper.¹ One or both sides can be etched.

3. Turbulent Drag Reduction

Two sets of electrodes are etched onto the upper surface of the electrode sheet with a common ground electrode between opposing pairs. On energizing one electrode set, the offset of the ground electrode confines plasma formation to one side of the exposed electrode only. At a later point in time the other electrode set is energized, causing plasma to form on the opposite side of these electrodes. By switching the electrodes at an optimum frequency, it is possible

to produce spanwise flow oscillation in the near-wall region of the turbulent boundary layer.^{2,3} We have observed up to 45% of skin-friction drag reduction in the downstream of the actuators. Figure 2 shows the time averaged velocity profile with and without plasma forcing. The plasma causes a large streamwise velocity deficit in the lower region of the boundary layer, extending for $0.1 < y/\delta^* < 2$ ($6 < y^+ < 110$). Within this region, the mean velocity has been reduced by as much as 40% at $y/\delta^* \approx 0.5$ ($y^+ \approx 30$).

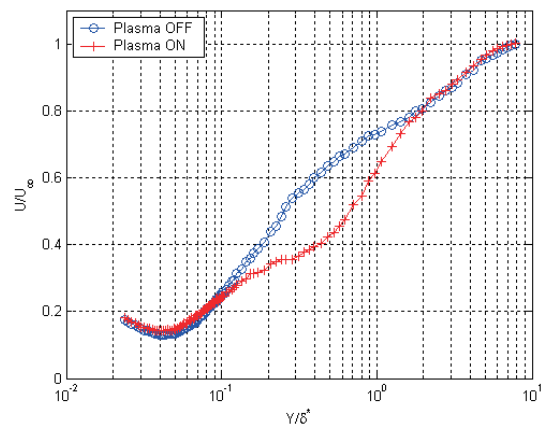


Fig. 2 Mean streamwise velocity profile with (+) and without (\circ) oscillatory surface plasma.

Figure 3 shows the turbulent intensity profile across the boundary layer. Velocity fluctuations have been reduced by as much as 30% for $0.1 < y/\delta^* < 0.55$ ($6 < y^+ < 30$). However, the magnitude of the fluctuations has been increased by up to 30% for $0.55 < y/\delta^* < 2.5$ ($30 < y^+ < 140$). This shift indicates that turbulence production has been reduced in the near-wall region, yet increased further out from the wall due to the change in local mean velocity gradient.

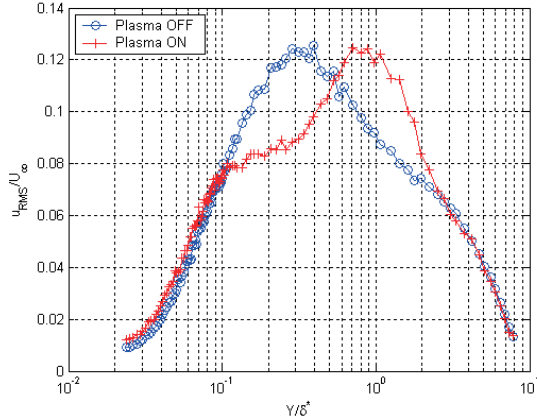


Fig. 3 Turbulent intensity profile with (+) and without (o) oscillatory surface plasma.

4. Flow Separation Control

For this experiment, a single plasma actuator was flush mounted within the circular cylinder. This consisted of two $17\mu\text{m}$ thick copper electrodes, separated by $250\mu\text{m}$ Mylar dielectric. The upper electrode was 1mm wide and offset relative to the lower. A high voltage ($E = \pm 3.5\text{kV}$) square-wave pulse train was delivered to the upper electrode. The circular cylinder was rotated about its axis so that the plasma forcing acted at several different azimuthal locations, θ , measured relative to the front stagnation point, where the freestream is from left to right. Plasma was created in 1ms duration pulses at various multiples of the Karman vortex shedding frequency ($f_{\text{plasma}}/f_K = 0.5, 1, 2, 4, 8, 14$). Note that the frequency of separated shear layer roll-ups occurs at $f_{\text{SL}}/f_K = 5.6$ at this Reynolds number.⁴

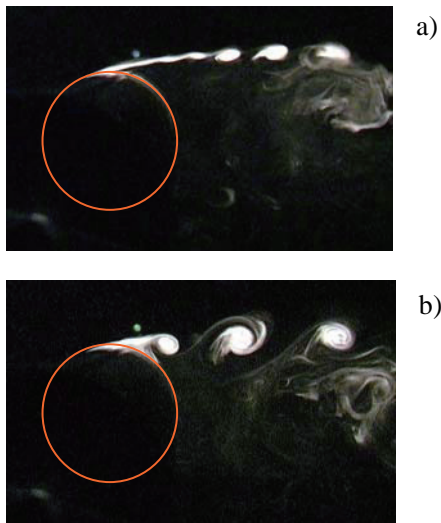


Fig. 4 Flow visualisation images at $\text{Re}_d = 3.3 \times 10^3$. a) Without plasma; b) with plasma actuator at $\theta = 87^\circ$, pulsed at $f_{\text{plasma}}/f_K = 4$.

Figure 4 shows flow visualisation images of the flow around the cylinder with and without plasma forcing. Without plasma (Fig. 4a), it is shown that the free shear layers rolled up into Karman vortices. Plasma forcing (Fig. 4b), clearly caused a significant change in the global flow structure around and in the wake of the cylinder, causing a downstream shift in the separation point. The effectiveness of the plasma in reattaching the flow was dependant on the actuator location. The most dramatic change was observed when the actuator was placed at 87° (i.e. very close to the natural separation point), where the flow was significantly reattached for all plasma forcing frequencies. In fact, the flow appeared to become reattached to the rearward stagnation point when $f_{\text{plasma}}/f_K = 14$.

5. Conclusions

Surface plasma actuators are versatile devices for active flow control, which can be integrated into aeronautical structures, such as the surface of aircraft wings or nacelle. Many flow control applications are possible with these devices from skin-friction reduction to separation flow control as has been demonstrated in this paper. We have also shown that the actuator configuration is easily adjustable, making unique applications possible. It is hoped that this paper could give an opportunity to aerospace engineers to take a look at surface plasma actuators and to find out what they are capable of.

This paper was based on the results of a research project funded by EPSRC and BAE SYSTEMS. TS was a research fellow of Japan Society for the Promotion of Science (JSPS).

References

- 1) T.N. Jukes, K.-S. Choi, G.A. Johnson and S.J. Scott: Characterisation of surface plasma-induced wall flows through velocity and temperature measurement. *AIAA J.*, **44** (2006) 764-771.
- 2) G.E. Karniadakis and K.-S. Choi: Mechanisms on transverse motions in turbulent wall flows. *Ann. Rev. Fluid Mech.*, **35** (2003) 45-62.
- 3) T.N. Jukes, K.-S. Choi, G.A. Johnson and S.J. Scott: Turbulent drag reduction by surface plasma through spanwise flow oscillation. *AIAA paper* 2006-3693 (2006).
- 4) A. Prasad and C.H.K. Williamson: The instability of the shear layer separating from a bluff body. *J. Fluid Mech.*, **333** (1997) 375-402.

Large-Eddy Simulation of Transition in Wall-Bounded Flow

P. Schlatter^{*}, S. Stolz^{**}, and L. Kleiser

Institute of Fluid Dynamics, ETH Zurich, Switzerland,

^{*} KTH Mechanics, Stockholm, Sweden,

^{**} Philip Morris Research & Development, Neuchâtel, Switzerland

ABSTRACT

Laminar-turbulent transition is a crucial phenomenon appearing in a variety of industrial applications. However the involved physical mechanisms as well as methods for reliable and accurate prediction of transition are still a matter of active research. In the present contribution, we give a brief overview on recent advances in the simulation and prediction of transitional and turbulent wall-bounded shear flows. The focus is on large-eddy simulations (LES), which differ from direct numerical simulations (DNS) by resolving only the large-scale, energy-carrying vortices of the fluid flow, whereas the fine-scale fluid oscillations, assumed to be more homogeneous, are treated by a subgrid-scale (SGS) model. The application of LES to flows of technical interest is promising and LES is getting more and more applied to practical problems. The main reason for this is that LES provides an increased accuracy compared to solutions of the (statistical) Reynolds-averaged Navier-Stokes equations (RANS), while requiring only a fraction of the computational cost of a corresponding fully-resolved DNS. Nevertheless, LES of practical transitional and turbulent flows still require massive computational resources and the use of large-scale computer facilities.

Key Words: Large-Eddy Simulation, Deconvolution Modelling, Wall Turbulence, Transition

1. Laminar-Turbulent Transition

Fluid flows are important in many technical applications of today's industrial world. The knowledge of the local fluid state, i.e. laminar or turbulent, is of major importance, since for instance drag and mixing significantly differ between the ordered laminar flow and the chaotic turbulent motion. Applications include e.g. flows along wings, intermittent flows around turbine blades and in combustion engines. The laminar-turbulent transition process and specifically its triggering mechanisms are not fully understood even nowadays. A summary of developments in transition research is given in the review article by Kachanov (1994) and in the monograph by Schmid & Henningson (2001).

A schematic overview of laminar-turbulent transition is given in Fig. 1 (taken from the LES presented in Schlatter, 2005) for the canonical case of plane incompressible channel flow excited by Tollmien-Schlichting (TS) waves (natural transition). The fluid flows along the plate until at a certain downstream position the laminar flow becomes unstable giving rise to two-dimensional wave disturbances. These spanwise rollers rapidly

evolve into three-dimensional perturbations of triangular shape (Λ -vortices), which in turn tend to break down into localised turbulent spots through the formation of pronounced hairpin vortices. The spots grow and merge to form a fully turbulent flow.

2. Numerical Simulation: LES

The fully resolved numerical solution of the Navier-Stokes equations is extremely expensive even for moderate Reynolds numbers Re since the required CPU time roughly scales as Re^3 . Practical high Reynolds-number calculations thus need to be performed using simplified turbulence models. Commonly used methods include the Reynolds-averaged Navier-Stokes equations (RANS) in which the mean flow is computed with statistical turbulence models. A technique with a level of generality in between DNS and RANS is the large-eddy simulation (LES). In an LES, only eddies (turbulent vortices) above a certain size are resolved on the numerical grid, whereas the effect of the smaller scales is modelled by a subgrid-scale (SGS) model. The scale separation is motivated by the conjecture that smaller eddies are more homogeneous and isotropic than the large ones and depend less on the specific flow situation. For an

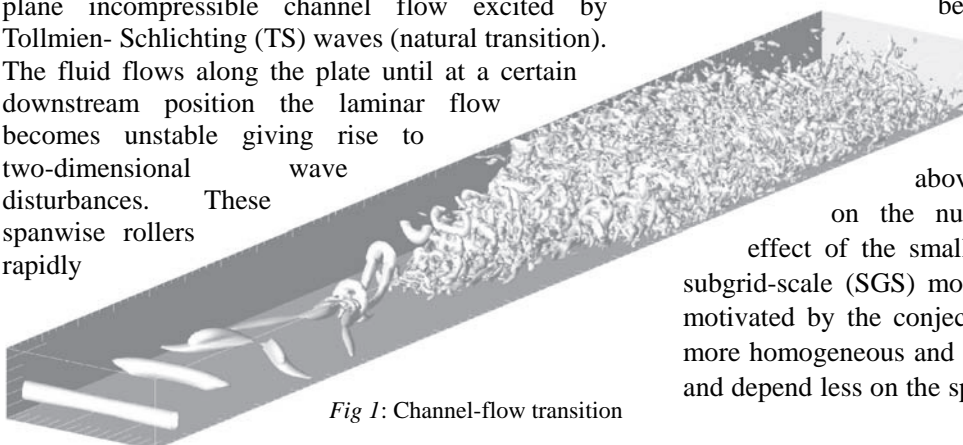


Fig 1: Channel-flow transition

LES thus only a fraction of the computational cost compared to a fully resolved DNS (typically of order 0.1-1%) is required.

The success of an LES is essentially dependent on the quality of the underlying subgrid scale (SGS) model, but also on the applied numerical discretisation scheme (its order and accuracy). However, the latter point has only recently been put into active consideration (Chow and Moin, 2003). The most common SGS model is the Smagorinsky (1963) model, based on the eddy-viscosity assumption. A major generalisation of SGS modelling was achieved by Germano et al. (1991) who proposed an algorithm which allows for dynamically adjusting coefficients of SGS models. A different class of SGS models has been introduced by Bardina et al. (1980) based on the scale-similarity assumption. Considerable research effort has recently been devoted to the development of SGS models of velocity estimation or deconvolution type, see e.g. the review by Domaradzki and Adams (2002). General reviews about different strategies for LES and SGS modelling are given in Lesieur and Métais (1996), Meneveau and Katz (2000) and Piomelli (2001) as well as in the recent text books by Sagaut (2005), Geurts (2003) and Lesieur et al. (2005).

3. LES of Laminar-Turbulent Transition

In transitional flows one is typically dealing with stability problems where small initial disturbances with energies many orders of magnitude smaller than the energy of the steady base flow are amplified and may finally evolve into turbulent fluctuations. Moreover, the spatial and temporal evolution of various wave disturbances and their nonlinear interaction needs to be computed accurately over many disturbance cycles. An SGS model suitable for transition should be able to deal equally well with laminar, various stages of transitional and turbulent flow states. The model should leave the laminar base flow unaffected and only be effective when nonlinear interactions between the resolved and non-resolved scales become important. The initial laminar flow and the following growth of the instability waves is often sufficiently resolved even on a coarse LES grid.

While a number of applications of different SGS models to turbulent flows have been analysed, the application to transitional flows has become an active field of research only recently. An example of the difficulty of transitional flows is that the classical Smagorinsky model is too dissipative and usually, in addition to distorting laminar flows, relaminarises transitional flows. Several improvements have been

proposed, e.g., by Piomelli et al. (1990), Voke and Yang (1995) and Germano et al. (1991) with the dynamic model. Several extended and more robust versions of the dynamic model have been proposed, e.g. the Lagrangian dynamic SGS model (Meneveau et al., 1996) or the localisation model (Ghosal et al., 1995). A slightly different approach was followed by Ducros et al. (1996) with the filtered structure function (FSF) model. A high-pass filter is used to decrease the influence of large scales in the calculation of the SGS terms. As a consequence, the model influence is reduced in regions where the mean-flow shear dominates over the turbulent shear, e.g. in the vicinity of walls or in laminar regions. Related models include the filtered Smagorinsky model (Sagaut et al., 2000) and also the dynamic mixed-scale model (Sagaut, 1996). Another way to avoid model contributions in laminar flow was followed by Vreman (2004) and subsequently Park et al. (2006) by constructing the SGS stress tensor such that it vanishes in undisturbed flow. The variational multiscale (VMS) method by Hughes et al. (2000), providing an explicit scale separation between the large and small scales based on disjunct spectral filters has, e.g., been used for simulating bypass transition along a flat plate (Calo, 2004).

As to the work of our group, in Schlatter (2005), results obtained using LES of transitional and turbulent incompressible channel flow are presented. These simulations have been performed using spectral methods in which numerical errors (differentiation, aliasing) are small. Various classical and newly devised SGS closures have been implemented and evaluated, including the approximate deconvolution model (ADM, Stolz and Adams, 1999), the relaxation-term model (ADM-RT) (Stolz and Adams, 2003 and Schlatter et al., 2004), and the new class of high-pass filtered (HPF) eddy-viscosity models (Stolz et al. 2005, Schlatter et al., 2005a and Stolz et al., 2005, 2007). These models are discussed briefly in the following.

In Schlatter et al. (2004), in addition to the original ADM algorithm, new variants have been examined. In particular an SGS model (ADM-RT model) with direct relaxation regularisation of the velocities based on a 3D high-pass filtering of the computational quantities is investigated. This model is related to the spectral vanishing viscosity (SVV) approach (Karamanos and Karniadakis, 2000). The appropriate definition of the relaxation term causes the model contributions to vanish during the initial stage of transition and, approximately, in the viscous sublayer close to walls.

The application of the HPF eddy-viscosity models to transitional flows was presented in Stolz et al. (2005), see also Vreman (2003). The HPF formulation is related to the VMS by computing the SGS terms on a highpass-filtered velocity field, thereby, with suitable filters, ignoring mean shear. Detailed analysis of the energy budget including the SGS terms revealed that the contribution to the mean SGS dissipation is nearly zero for the HPF models, while it is a significant part of the SGS dissipation for other models (Schlatter et al., 2005a). Moreover, unlike the classical eddy-viscosity models, the HPF models are able to predict backscatter. It has been shown that in channel flow that locations with intense backscatter are closely related to low-speed turbulent streaks in both LES and filtered DNS data.

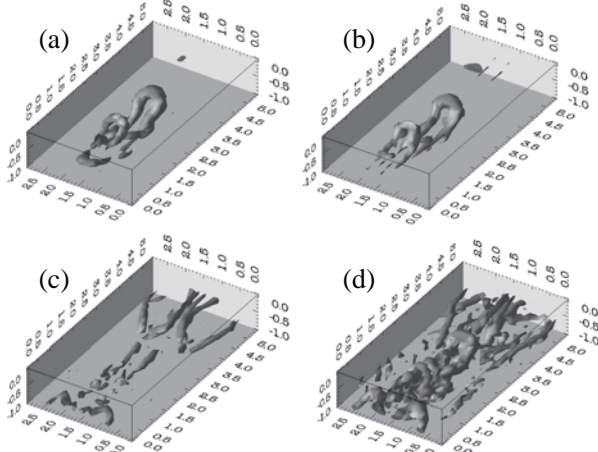


Fig. 3: Comparison of the prediction of transitional structures using different SGS models: (a) fully-resolved DNS, (b) ADM-RT, (c) dynamic Smagorinsky model, (d) no-model LES (coarse-grid DNS). The box contains only 32x32x33 grid points (from Schlatter et al., 2005b).

The above references demonstrate that, e.g. for the model problem of temporal transition in channel flow, averaged integral flow quantities like the skin friction Reynolds number Re_τ or the shape factor H_{12} can be predicted reasonably well by LES even on coarse meshes (see also Meyers and Sagaut, 2007). However, for a reliable LES in particular applied to transitional flows, it is equally important to faithfully represent the physically dominant transitional flow mechanisms and their 3D vortical structures such as the formation of Λ and hairpin vortices. A successful SGS model needs to predict those structures well even at low resolution, as demonstrated by Schlatter et al. (2005b), Schlatter et al. (2006) and Stolz et al. (2007). A comparison of various SGS models and their performance to predict transitional structures is shown in Fig. 2 for temporal channel-flow transition. When considering integral quantities only (e.g. skin

friction) major differences between the predictions could not be established (Schlatter et al., 2004). The flow structures however have been found to be fairly different. In particular, the no-model LES and the standard dynamic Smagorinsky model fail to predict a distinct roll-up of the shear layers, and additionally spurious structures appear which lead to premature breakdown to turbulent flow. On the other hand, the high-order relaxation in the ADM-RT model closely follows the evolution of the exact (DNS) data.

In Schlatter et al. (2006), different SGS models have been tested and compared in both the temporal and the spatial transition simulation approach. Fig. 3 shows a series of visualisations taken from a spatial LES using the ADM-RT model during classical K-type transition clearly showing the relevant series of break-ups of the distorted vortical structures eventually leading to a turbulent flow.

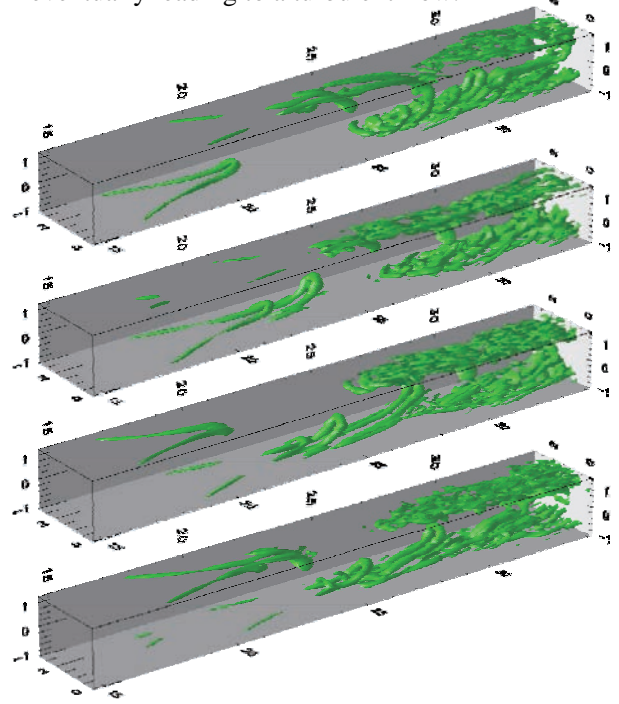


Fig. 2: Sequence (top to bottom) of vortical structures during spatial K-type transition using the ADM-RT model with only 32 grid points in the wall-normal and spanwise direction (Schlatter et al., 2006).

Compressible supersonic boundary-layer transition has recently been considered by Stolz et al. (2007). Compressible flows differ in various aspects from incompressible one: Not only is the type of equations changed to hyperbolic, giving the possibility of shock waves, but also the applied numerical methods are different. Whereas the above results used spectral methods, for the compressible case finite differences were employed. It is important to test modelling approaches also for compressible

transition and turbulence. The results in Stolz et al. (2007) show that using both ADM and the HPF model accurate approximate statistics (velocity profiles, skin friction etc.) are found. In addition ADM was found to be capable to predict instantaneous (flow structures) and at significantly reduced resolution.

At present, research in LES follows various directions. On the one hand, improved and new SGS models are developed; existing models are also applied to more complex flow cases with good results. In that respect, LES has matured to a research tool to predict e.g. complex transitional scenarios, see the recent application to bypass transition and control mechanisms (Schlatter et al. 2007a,b). On the other hand, methods to actually quantify the errors of LES, e.g. induced by the lower resolution, but also by the discretisation scheme (Geurts, 2006) are considered. Solution-adaptive grid-refinement methods are currently being developed which could allow more reliable (and efficient) results for complex flow cases (Hoffman, 2006).

4. Summary

The results obtained for transitional wall-bounded flows using various SGS models show that it is in fact possible to accurately simulate transition using LES on relatively coarse grids. However, the performance of the various models examined is considerably different with respect to an accurate prediction of e.g. the transition location and the characteristic transitional flow structures.

By examining instantaneous flow fields from LES of channel flow transition, additional distinct differences between the SGS models can be established. Some models which are based on high-pass filtering, e.g. ADM, ADM-RT and also the HPF eddy-viscosity models, are able to provide a realistic description of the flow structures up to the point of breakdown. In addition, the HPF eddy-viscosity models can be easily implemented in particular as an alternative to classical fixed-coefficient eddy-viscosity models, whilst performing significantly better than their non-highpass-filtered counterparts.

To conclude, LES using advanced SGS models are able to faithfully simulate flows which contain intermittent laminar, turbulent and transitional regions.

J. Bardina, J. H. Ferziger, W. C. Reynolds: AIAA Paper 1357 (1980).
 V. M. Calo: Dissertation Stanford University (2004).
 J. A. Domaradzki, N. A. Adams: J. Turbulence, 3 (2002).
 F. Ducros, P. Comte, M. Lesieur: J. Fluid Mech., 326 (1996), pp. 1-36.

M. Germano, U. Piomelli, P. Moin, W. H. Cabot: Phys. Fluids A, 3:7 (1991), pp. 1760-1765.
 B. J. Geurts: *Elements of Direct and Large-Eddy Simulation*, (2003), Edwards.
 B. J. Geurts: J. Turbulence, 7:55 (2006), pp. 1-16.
 S. Ghosal, T. S. Lund, P. Moin, K. Akselvoll: J. Fluid Mech., 286 (1995), pp. 229-255.
 J. Hoffman: J. Fluid Mech., 568 (2006), pp. 77-88.
 T. J. R. Hughes, L. Mazzei, K. E. Jansen: Comput. Visual. Sci., 3 (2000), pp. 47-59.
 Y. S. Kachanov: Annu. Rev. Fluid Mech., 26 (1994), pp. 411-482.
 G.-S. Karamanos, G. E. Karniadakis: J. Comput. Phys., 163 (2000), pp. 22-50.
 M. Lesieur, O. Métais: Annu. Rev. Fluid Mech., 28 (1996), pp. 45-82.
 M. Lesieur, O. Métais, P. Comte: *Large-Eddy Simulations of Turbulence*, (2005), Cambridge University Press.
 C. Meneveau, T. S. Lund, W. H. Cabot: J. Fluid Mech., 319 (1996), pp. 353-385.
 C. Meneveau, J. Katz: Annu. Rev. Fluid Mech., 32 (2000), pp. 1-32.
 J. Meyers, P. Sagaut: Phys. Fluids, 19:048105 (2007), pp. 1-4.
 N. Park, S. Lee, J. Lee, H. Choi: Phys. Fluids, 18:125109 (2006), pp. 1-24.
 U. Piomelli, T. A. Zang, C. G. Speziale, M. Y. Hussaini: Phys. Fluids A, 2:2 (1990), pp. 257-265.
 U. Piomelli: CFD2001 Proceedings, Kitchener (2001).
 P. Sagaut: Rech. Aéro., 1 (1996), pp. 51-53.
 P. Sagaut, P. Comte, F. Ducros: Phys. Fluids, 12:1 (2000), pp. 233-236.
 P. Sagaut: *Large Eddy Simulation for Incompressible Flows*, (2005), Springer.
 P. Schlatter, S. Stolz, L. Kleiser: Int. J. Heat Fluid Flow, 25:3 (2004), pp. 549-558.
 P. Schlatter: Dissertation ETH Zurich, No. 16000 (2005).
 P. Schlatter, S. Stolz, L. Kleiser: J. Turbulence, 6:5 (2005a), pp. 1-21.
 P. Schlatter, S. Stolz, L. Kleiser: IUTAM Symposium on Laminar-Turbulent Transition (2005b), Springer, pp. 323-328.
 P. Schlatter, S. Stolz, L. Kleiser: J. Turbulence, 7 (2006), pp. 1-24.
 P. Schlatter, H. C. de Lange, L. Brandt: Turbulence and Shear Flow Phenomena 5 (2007), to appear.
 P. Schlatter, H. C. de Lange, L. Brandt: Advances in Turbulence XI (2007), to appear.
 P. Schmid, D. S. Henningson: *Stability and Transition in Shear Flows*, (2001), Springer.
 J. Smagorinsky: Mon. Weath. Rev., 91:3 (1963), pp. 99-164.
 S. Stolz, N. A. Adams: Phys. Fluids, 11:7 (1999), pp. 1699-1701.
 S. Stolz, N. A. Adams: Phys. Fluids, 15:8 (2003), pp. 2398-2412.
 S. Stolz: J. Fluids Eng., 127 (2005), pp. 666-673.
 S. Stolz, P. Schlatter, L. Kleiser: Phys. Fluids, 17:065103 (2005), pp. 1-14.
 S. Stolz, P. Schlatter, L. Kleiser: AIAA J., 45:5 (2007), pp. 1019-1027.
 P. Voke, Z. Yang: Phys. Fluids, 7:9 (1995), pp. 2256-2264.
 A. W. Vreman: Phys. Fluids, 15:8 (2003), pp. L61-L64.
 A. W. Vreman: Phys. Fluids, 16:10 (2004), pp. 3670-3681.

On the concept of hydraulically smooth wall

J.M.Floryan

Department of Mechanical and Materials Engineering
The University of Western Ontario, London, Ontario, Canada

ABSTRACT

A search for a precise definition of hydraulically smooth wall is carried out. It is argued that in the case of transitional flows such definition can be based on the onset of flow instabilities. Flow in a channel with distributed surface roughness is considered as a case study. Results of the linear stability analysis show that the presence of the roughness destabilizes the traveling-wave instability as well as introduces a new instability that manifests itself in the form of streamwise vortices. The critical conditions for the occurrence of both instabilities are given for different classes of roughness shape. It is shown that these conditions can be predicted with a reasonable accuracy in the case of an arbitrary (but Fourier transformable) roughness by considering only the leading Fourier mode (wavy-wall model). A segment in the parameter space where the roughness does not induce any instability regardless of its shape has been identified; this segment identifies conditions under which the rough wall behaves as a hydraulically smooth wall.

Key Words: flow instabilities, distributed surface-roughness, hydraulically smooth wall.

1. Introduction

Flows over rough walls have been studied since the early works of Hagen¹ and Darcy², which were focused on turbulent regimes. Reynolds³ was the first to pose the problem in the context of laminar-turbulent transition. While the questions studied, i.e., what kind of effects the presence of distributed surface roughness can induce in a flow and when a rough wall behaves as hydraulically smooth, are of fundamental importance their rational resolution is still lacking. Both questions are of considerable practical importance in several application areas, e.g., design of large Reynolds number laminar airfoils, small Reynolds number turbulent airfoils, compact heat exchangers, laminar electrostatic precipitators, etc. The original investigations involved measurements of turbulent flows in open channels and in pipes. Various possible roughness forms were classified using the concept of "equivalent roughness"³. Phenomenological effects of the "equivalent roughness" were summarized in the form of friction coefficient⁵⁻⁷. These and other similar investigations show that surface roughness contributes directly to the dynamics of turbulent flow only if the wall is hydraulically rough. The concept of hydraulic smoothness is very appealing; however, no precise criterion exists for predicting whether a given surface can be considered as being hydraulically smooth for flow conditions of interest. While the modelling concepts of this type have been continuously re-evaluated⁸⁻⁹, they failed so far to uncover the mechanisms that govern the complex, flow-condition-dependent interaction between the

roughness geometry and the moving fluid.

This presentation reviews the role played by distributed roughness in the laminar-turbulent transition process in shear layers. It is known that this process involves various instabilities that eventually lead to the fully turbulent state. The experimental evidence shows that the roughness contributes directly to the dynamics of the flow only if its amplitude is sufficiently large. A frequently used criterion for determination of the critical roughness size is that the roughness Reynolds number $Re_k = U_k k / \nu < 25$ ¹⁰, where k is the roughness height, U_k is the undisturbed velocity at height k and ν the kinematic viscosity. Such a criterion, however, does not address the issue of shape and distribution of the roughness.

There is a large body of experimental observations focused on the laminar-turbulent transition that provide phenomenological description of the flow response in the form of correlations between the height of the roughness, the flow conditions and the critical Reynolds number for certain classes of geometrical forms of the roughness¹¹⁻¹⁵. The range of applicability of these correlations is not certain because they are based on a limited experimental data and have been determined for, in essence, artificially created roughness forms. These correlations, nevertheless, form the basis of all roughness sensitive designs.

The surface roughness can be divided into three classes for the purposes of discussion, i.e., isolated

two-dimensional roughness, e.g., spanwise trip wire, isolated three-dimensional roughness and distributed roughness. The transition mechanisms for the first class of roughness is associated with inflectional separated velocity profiles and are considered understood at least on qualitative level¹⁶⁻¹⁸. The characteristic feature of the flow around an isolated, three-dimensional roughness element is the presence of the horseshoe vortex that generates streamwise vortices on the downstream side¹⁰. The transition mechanism is thought to be associated with the strong instabilities of inflectional shear layers set up by the streamwise vortices, similar to the case of Görtler instability¹⁹. The effects of distributed roughness are not understood¹⁰. Various experiments indicate that when the roughness is operative the departure from the laminar state is explosive²⁰⁻²¹. Theoretical attempts based on the roughness-induced distortion of velocity profile proved inconclusive²²⁻²⁴ similarly as did concepts based on the roughness-induced additional mixing²⁵. The spectral model of roughness shape²⁶ proved to be very powerful and holds a promise to uncover the mechanisms associated with the distributed roughness. Theoretical analysis of the two-dimensional traveling-wave instability²⁷ shows that the roughness is responsible for the reduction of the critical Reynolds number and the amount of reduction is in agreement with the experimental observations²⁸. Three-dimensional analyses of Couette flow over wavy-wall²⁹ and Poiseuille flow in a converging-diverging channel³⁰ show that surface corrugations are able to generate streamwise vortices. Surface roughness may also play a large role in the transition process through amplification of the transient growth mechanism³¹; however, this role remains to be substantiated.

The main objective of the analysis described in the next section is the determination of the role played by distributed surface roughness in the early stages of the transition process through the use of the linear stability theory. This analysis uses spectral models²⁶ where the roughness geometry is represented in terms of Fourier expansions. Determination of the effects of different geometries is reduced to scans of parameter space formed by the coefficients of such expansions. Use of stability theory provides a convenient tool for the identification of the conditions when the roughness is not hydraulically active; roughness that does not destabilize the flow modifies the flow in an insignificant manner and thus such wall may be considered as hydraulically smooth. The reader should note that the just proposed definition of hydraulic smoothness for transitional flows is different from the common albeit ill-defined smoothness for turbulent flows where the smoothness

implies turbulent friction independent of the roughness.

2. Outline of the analysis

We follow Ref.[32] and begin with the plane Poiseuille flow confined between flat rigid walls at $y=\pm 1$ and extending to infinity in the x -direction. Velocity and pressure fields in the form

$$\mathbf{V}_0(\mathbf{x}) = [u_0(y), 0] = (1 - y^2, 0), \quad p_0(\mathbf{x}) = -2x / \text{Re}, \quad (1)$$

describe the fluid motion, where the motion is directed towards the positive x -axis, $\mathbf{x}=(x, y)$, and the Reynolds number Re is based on the half-channel height and the maximum x -velocity. Assume that the lower wall is replaced by a corrugated wall whose location $y_L(x)$ is specified as

$$y_L(x) = -1 + \sum_{n=-\infty}^{n=\infty} S^{(n)} e^{in\alpha x} \quad (2)$$

where $S^{(n)} = S^{(-n)*}$ and star denotes the complex conjugate. The flow in the corrugated channel can be represented as

$$\mathbf{V}_2(\mathbf{x}) = [u_2(x, y), v_2(x, y)] = \mathbf{V}_0(\mathbf{x}) + \mathbf{V}_1(\mathbf{x}) = [u_0(y), 0] + [u_1(x, y), v_1(x, y)], \quad (3)$$

$$p_2(\mathbf{x}) = p_0(x) + p_1(x, y),$$

where \mathbf{V}_1 and p_1 are the velocity and pressure modifications owing to the presence of the corrugation. Substitution of the above representation of the flow quantities into the Navier-Stokes and continuity equations, introduction of stream function defined as $u_1 = \partial_y \Psi$, $v_1 = -\partial_x \Psi$, elimination of pressure and representation of the unknowns in the form of Fourier expansions

$$\Psi(x, y) = \sum_{n=-\infty}^{n=\infty} \Phi^{(n)}(y) e^{in\alpha x} \quad (4)$$

where $\Phi^{(n)} = \Phi^{(-n)*}$, $f_u^{(n)} = f_u^{(-n)*}$, $f_v^{(n)} = f_v^{(-n)*}$, lead to

a system of nonlinear ordinary differential equations for the functions $\Phi^{(n)}$, $n \geq 0$, in the form

$$\left[D_n^2 - in\alpha \text{Re}(u_0 D_n - D_n^2 u_0) \right] \Phi^{(n)} - i\alpha \text{Re} \sum_{k=-\infty}^{k=\infty} [k D \Phi^{(n-k)} D_k \Phi^{(k)} - (n-k) \Phi^{(n-k)} D_k D \Phi^{(k)}] = 0, \quad (5)$$

where $D = d/dy$, $D_n = D^2 - n^2 \alpha^2$. The boundary conditions at the channel walls are expressed in the form

$$u_0(y_L(x)) + u_1(x, y_L(x)) = 0, \quad v_1(x, y_L(x)) = 0, \quad (6a)$$

$$u_1(x, 1) = 0, \quad v_1(x, 1) = 0. \quad (6b)$$

The above formulation is closed with the fixed volume flux condition and the problem is solved numerically.

The linear stability analysis begins with the governing equations in the form of vorticity transport and continuity. Unsteady, three-dimensional disturbances are superimposed on the mean part in

the form

$$\boldsymbol{\omega} = \boldsymbol{\omega}_2(x, y) + \boldsymbol{\omega}_3(x, y, z, t), \quad \mathbf{V} = \mathbf{V}_2(x, y) + \mathbf{V}_3(x, y, z, t),$$

where subscripts 2 and 3 refer to the mean flow and the disturbance field, respectively. The above equation is substituted into the field equations, the mean part is subtracted and the equations are linearized. The resulting disturbance equations have the form

$$\begin{aligned} \partial \boldsymbol{\omega}_3 / \partial t + (\mathbf{V}_2 \cdot \nabla) \boldsymbol{\omega}_3 - (\boldsymbol{\omega}_3 \cdot \nabla) \mathbf{V}_2 + (\mathbf{V}_3 \cdot \nabla) \boldsymbol{\omega}_2 - \\ (\boldsymbol{\omega}_2 \cdot \nabla) \mathbf{V}_3 = \text{Re}^{-1} \nabla^2 \boldsymbol{\omega}_3, \\ \nabla \cdot \mathbf{V}_3 = 0, \quad \boldsymbol{\omega}_3 = \nabla \times \mathbf{V}_3 \end{aligned} \quad (7a-c)$$

and are subject to the homogeneous boundary conditions

$$\mathbf{V}_3(x, 1, z, t) = 0, \quad \mathbf{V}_3(x, y_L(x), z, t) = 0 \quad (7d)$$

where y_L is given by Eq. (2). The disturbance velocity vector is assumed in the form $\mathbf{v}_3(x, y, z, t) =$

$$\sum_{m=-\infty}^{m=+\infty} [g_u^{(m)}(y), g_v^{(m)}(y), g_w^{(m)}(y)] e^{i[(\delta+m\alpha)x + \beta z - \sigma t]} + CC \quad (8)$$

Substitution of (8) into (7) leads to an eigenvalue problem for (δ, β, σ) for the ordinary differential equations describing functions $g_u^{(m)}, g_v^{(m)}, g_w^{(m)}$. The system of equations governing $g_u^{(m)}, g_v^{(m)}, g_w^{(m)}$ has the form

$$\begin{aligned} S^{(m)}(t_m g_w^{(m)} - \beta g_u^{(m)}) + C g_v^{(m)} = \\ i \text{Re} \sum_{n=-\infty}^{n=\infty} (W_u^{(m,n)} g_u^{(m-n)} + W_v^{(m,n)} g_v^{(m-n)} + W_w^{(m,n)} g_w^{(m-n)}) \\ T^{(m)} g_v^{(m)} = \\ - \text{Re} \sum_{n=-\infty}^{n=\infty} (B_u^{(m,n)} g_u^{(m-n)} + B_v^{(m,n)} g_v^{(m-n)} + B_w^{(m,n)} g_w^{(m-n)}) \\ it_m g_u^{(m)} + D g_v^{(m)} + i \beta g_w^{(m)} = 0, \quad -\infty < m < \infty \end{aligned} \quad (9a-c)$$

where the explicit forms of the operators T, S, C, W, B are given in Ref.[32]. The boundary conditions have the form

$$\begin{aligned} g_u^{(m)}(1) = g_v^{(m)}(1) = g_w^{(m)}(1) = 0. \\ \sum_{m=-\infty}^{m=+\infty} [g_u^{(m)}(y_L), g_v^{(m)}(y_L), g_w^{(m)}(y_L)] = 0 \end{aligned} \quad (10)$$

Equations (9) with boundary conditions (10) have nontrivial solutions only for certain combinations of parameters δ, σ and β . The required dispersion relation has to be determined numerically. For the purposes of calculations, the problem is posed as an eigenvalue problem for σ and its solution is determined numerically.

3. Results and Discussion

Calculations have been carried out for the roughness in the form of sinusoidal wall (wavy wall model), wall with triangular indentations, wall with rectangular indentations and wall with “bump” 32

indentations. Unstable disturbances in the form of streamwise vortices and traveling waves have been identified in all cases. A critical Reynolds number, a critical disturbance wavenumber and a critical roughness wavenumber have been identified for each roughness amplitude S . Results displayed in Fig.1 show that it is possible to identify the maximum permissible roughness amplitude that does not induce any instability for flow conditions of interest regardless of the roughness shape.

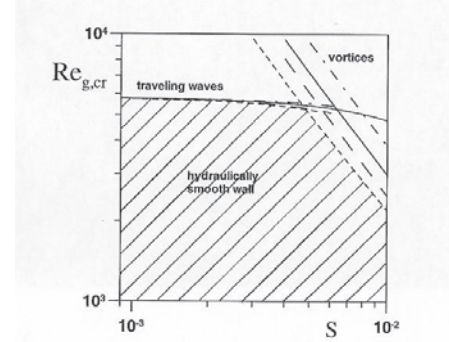


Figure 1. Variations of the global critical Reynolds number $Re_{g,cr}$ describing the traveling-wave instability and the vortex-like instability for the corrugated channel as a function of the corrugation amplitude S . The dash, dash-dot and continuous lines correspond to the corrugation in the form of rectangular grooves, triangular grooves and “sine-bump” grooves, respectively. The shaded area corresponds to the flow conditions that do not produce any instability for the corrugation geometries subject to this investigation.

4. Summary

The critical curves displayed in Fig. 1 demonstrate qualitative similarity of flow response for all corrugation geometries subject to this investigation. If the corrugation amplitude for a given shape and distribution (as defined by the corrugation wave number) and given flow conditions (as defined by the flow Reynolds number) is sufficiently small, such corrugation is able to induce only small modifications in the flow. When the size of the corrugation reaches critical conditions, it can induce large changes in the flow through various instability processes. We can therefore use the onset of any instability as the event that defines the conditions when the wall ceases to be hydrodynamically smooth.

References

- 1) G.Hagen: Math. Abh. Akad. Wiss., (1854) pp.17-98.
- 2) H.Darcy, Recherches expérimentales relatives au mouvement de l'eau dans les tuyaux, Paris, Mallet-Bachelier, (1857).

- 3) O.Reynolds, Philos. Trans. R. Soc. London, **174**, (1883), pp.935-82.
- 4) J.Jimenez, Ann. Rev. Fluid Mech., **36**, (2004), pp.173-196.
- 5) J.Nikuradse, VDI-Forschungsheft #361, (1933); also NACA TM 1292 (1950).
- 6) C.F.Colebrook, J. Institute of Civil Engineers London, **11**, (1939), pp.133-156.
- 7) L.F.Moody, Transactions of the ASME, **66**, (1944), pp.671-684.
- 8) P.Bradshaw, Phys.Fluids, **12**, (2000), pp.1611-1614.
- 9) D.R. Waigh and R.J.Kind, AIAA J., **36**, (1998), pp.1117-1119.
- 10) M.V.Morkovin, In Instability and Transition (ed. M.Y.Hussaini and R.G.Voigt), **1**, pp.281-295. ICASE/NASA LARC Series, Springer, 1990.
- 11) A.Fage, Br. Aero. Res. Council Report No.2120 (1943).
- 12) B.H.Carmichael, Northrop Aircraft Report No. NOR-59-438 (BLC123), (1957).
- 13) H.Schlichting, Boundary Layer Theory, 7th ed., McGraw-Hill, (1979).
- 14) I.Tani, In Boundary Layer and Flow Control, (ed. G.V.Lachman), **2**, (1961), pp.637-656, Pergamon.
- 15) A.E.Doenhoff and A.L.Braslow, In Boundary Layer and Flow Control, (ed. G.V.Lachman), **2**, (1961), pp.657-681, Pergamon.
- 16) P.S.Klebanoff and K.D.Tidstrom, Phys. Fluids, **15**, (1972), pp.1172-1188.
- 17) A.H.Nayfeh, S.A.Ragab and A.A.Al-Maaitah, Phys.Fluids, **4**, (1988), pp.796-806.
- 18) J.A.Masad and V.Iyer, Phys. Fluids, **6**, (1994), pp.313-327.
- 19) J.M.Floryan, Progress in Aerospace Sciences, **28**, (1991), pp.235-271.
- 20) E.Reshotko, In Turbulence and Chaotic Phenomena (ed.T.Tatsumi). Proceedings of IUTAM Symposium, (1984), pp.39-46. Elsevier.
- 21) T.C.Corke, A.Bar Sever and M.V.Morkovin, Phys. Fluids, **29**, (1986), pp.3199-3213.
- 22) K.Singh and J.L.Lumley, Appl. Sci. Res., **24**, (1972), pp.168-186.
- 23) M.Lessen and S.T.Gangwani, Phys. Fluids, **19**, (1976), pp.510-513.
- 24) J.M.Kendall, AIAA Paper 81-0195, (1981).
- 25) C.L.Merkle, K.T-S Tzou and T.Kubota, Dynamics Technology Inc., Report DT-7606-4, (1977).
- 26) J.M.Floryan, J. Fluid Mech. **335**, (1997), pp.29-55.
- 27) J.M.Floryan, Phys. Fluids, **17**, (2005), pp.044101/8.
- 28) M.Asai and J.M.Floryan, European Journal of Mechanics/B Fluids, **25**, (2006), pp.971-986.
- 29) J.M.Floryan, Phys.Fluids, **14**, (2002), pp.312-322.
- 30) J.M.Floryan, J. Fluid Mech., **482**, (2003), pp.17-50.
- 31) J.Szumbariski and J.M.Floryan. J. Fluid Mech., **568**, (2006), pp.243-272.
- 32) J.M.Floryan. European Journal of Mechanics B/Fluids, **26**, (2007), pp.305-329.

Early Times of Fluid Mechanics in Japan: Terada, Tani, Imai, and Aeronautical Research Institute

Tsutomu KAMBE, Tokyo, Japan

Visiting Professor, Chern Institute of Mathematics (China)

ABSTRACT

Science history of fluid mechanics research in Japan is reviewed for the time during the first half of 20th century. Three distinguished persons, Torahiko Terada, Itiro Tani and Isao Imai, were more or less associated with the Aeronautical Research Institute. Before the establishment of the Institute, von Karman and Prandtl were invited to the Institute to give series of lectures.

Terada discovered a sequence of rolling eddies in the boundary layer cooled from above (or heated from below). Tani studied wing shapes and proposed a new wing which keeps its boundary layer laminar as long as possible. Imai resolved a paradox of divergence problem in an asymptotic solution starting from the Oseen equation, for a flow around a solid body placed in a uniform stream.

Key Words: Science History, Terada, Tani, Imai, Aeronautical Research Institute

1. Introduction

When we look back the first half of 20th century of fluid mechanics research in Japan, we find a number of remarkable studies. Three distinguished persons, Torahiko Terada, Itiro Tani and Isao Imai, were more or less associated with the Aeronautical Research Institute of Tokyo Imperial University. Before establishing the Institute, von Karman was invited to the Institute to give a series of lectures on contemporary researches of aeronautics and fluid mechanics in 1927, and in 1929 Prandtl too gave three-day lectures there. Soon after, a 3-meter-wind-tunnel of Göttingen type was constructed at the Institute of its new campus of Komaba.

2. Torahiko Terada (1878 -1935)

Terada (Fig.1) was a physicist, geo-physicist and an essayist, and good at making witty remarks. One of his well-known remarks is “*A natural disaster is likely to occur at such a time when people forget it*” (1934). This was a warning to the government which was preparing war. Another one is: “*A diamond can be processed to a jewel once it is dug up in the rough. However, glass is unable to be finished into a jewel*” (1931). He was warning scientists in general after resigning professorship at Physics Dept (Tokyo Imp. Univ.), but keeping his positions at three research

institutes. He published a paper with second-year students of Physics, “*Some experiments on periodic columnar forms of vortices caused by convection*”¹⁾. Terada recollects, “About ten years ago, it happened to observe the following :

Aluminum powder was mixed and suspended in alcohol. It was spread on the plane bottom of shallow basin, so as to form a thin layer of about 1 mm depth. On tilting the vessel, the liquid mixture flowed down along the plate bed. The powder is arranged into sharply defined bands, consisting of fine filaments running in the direction of liquid flow. Thus, he observed convective roll patterns of flow cooled by evaporation at surface, which was much earlier than studies in the west.

Terada’s experiment (1928) is now understood as a thermal boundary layer. The roll pattern (Fig.3) can be observed as filamentary cloud patterns of cold front flowing over warm moist-rich surface of the Japan Sea, by the satellite photo in winter time. Expressing perturbations by forms proportional to $\exp[\lambda t + iky]$ (where t and y

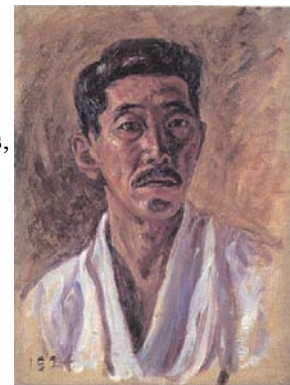


Fig.1 Self-Portrait
(T. Terada).

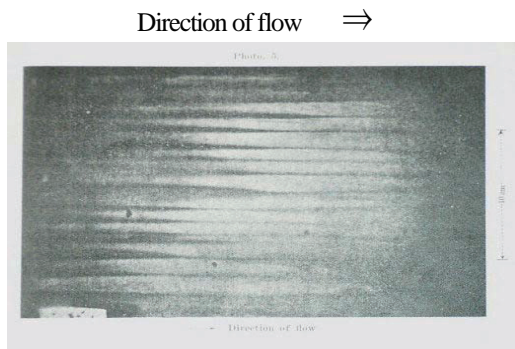


Fig.2 Convective roll pattern of water flow over heated bottom (Terada, 1928).

are time and horizontal coordinate, k the wave number, λ a constant, i the imaginary unit), one can write linear perturbation equations as follows:

$$(D^2 - a^2 - \lambda)T = -W$$

$$(D^2 - a^2)(D^2 - a^2 - \lambda/P)W = a^2 R_a T$$

where T and W represent variation amplitudes of temperature and vertical velocity, Ra the Rayleigh number, Pr the Prandtl number, and $a = k/\delta$, δ the thickness of boundary layer.

The above two equations are equivalent to the perturbation equations of Görtler problem, if we replace T and W with tangential and radial components of velocity (see Drazin and Reid, Ref.9). Terada's experiment was earlier by more than ten years than Görtler's work. (1940).

3. Karman and Prandtl in Japan

In 1921, the Aeronautical Research Institute was established in Tokyo Imp. Univ.. Koroku Wada (much later, to become its director) visited Europe from 1919 to 21, and met Prandtl and von Karman in Germany. When returned, he was asked: *Who is the best person to be invited for the sake of developing aeronautical research in Japan?* According to Iitiro Tani, Wada replied, "Prandtl". After the suggestion, an executive of Kawanishi (Aeroplane Company) visited Göttingen and tried to invite Prandtl to Japan. Prandtl suggested him to speak it to young von Karman. According to Karman's memoirs, his mother was reluctant to the offer, since there was another offer from USA as well. In order to decline, he required his reward to be doubled. Unfortunately, it was accepted. Karman (1881-1963) visited Japan in 1927. His monthly salary was ¥1,000 (when a high rank professor received ¥400. monthly). He gave a series of lectures on Aeronautics²⁾. The subjects were, (a) *Theory of propellers*, (b)

Flight performance, (c) *Stability of airplanes*, and (d) *Aerodynamics forces and vibration*.

Prandtl visited Japan too, in 1929 when an international congress of industries was held in Tokyo, and gave a lecture at the National Diet Building, on "The Role of Turbulence". At the Aeronautical Research Institute, he gave three lectures (Oct. 1929)³⁾: (i) *Turbulenz und ihrer Entstehung*, (ii) *Flüssigkeits-Strömungen: die Geschwindigkeit von der Grössenordnung der Schallgeschwindigkeit*, (iii) *Entstehung der Wirbel*.

Soon after, a 3-meter-wind-tunnel of Göttingen type (Fig.3) was constructed in the restarted Institute at the new campus of Komaba. Amazingly, it is still working at the same place.



Fig.3 Three-meter-wind-tunnel (March 25, 1930).

TANI once recollects: *An evidence of Log-law of turbulent boundary layer was first obtained in Japan.* In the paper of von Karman on the famous Log-law of velocity of the turbulent BL, Karman cited Wada's experimental work measuring turbulent friction drag, obtained in Japan. He regarded it as an experimental evidence for his derivation of Log-law. Tani writes: *I felt that I saw his deep insight and moral of a scientist.*

4. Research Development: KOKEN-KI (航研機)

Long-range Research-Plane named Koken-Ki (Fig.4: width: 27.93m, length: 15.06m, maximum speed: 245Km/h) was developed by the Aeronautical Research Institute (Tokyo Imperial Univ.). This plane accomplished the world record of *Non-Stop Flight-Distance* in 1938. This was the first big project of scientific research in Japan. According to the web-illustration⁴⁾, the flight was as follows.

Time was 4:55 early in the morning, May 13th, 1938. Wind was against with 1.4 m/s. Over-running the runway, the KOKENKI



Fig.4 KOKEN-KI (Aero-Institute-Plane)

finally floated the wing of the crimson (red) on the air. After three-day non-stop flight of 29 turns of a triangular closed flight course (Fig.5), it landed on May 15th, 1938, 7:20 p.m. with establishing the world record of total flight distance 11,000 km. Its speed of 186 km/h (over 10,000 km) was recorded officially. When it landed, its fuel was left sufficiently with 500 L.



Fig.5 Triangular flight course (Kanto, Japan).

5. Itiro TANI (1907–1990)

In 1940, Tani and Noda⁵⁾ proposed an LB24 wing, and Tani and Mituisi⁶⁾ tested experimental performance of LB24 (LB: Light-Blue, symbol color of Tokyo Imp. Univ.). Laminar wing LB24 (Fig.6) has a maximum thickness of $0.1c$ at the position $0.5c$, where c is the chord length, so that the minimum pressure occurs at a downstream position, while in the

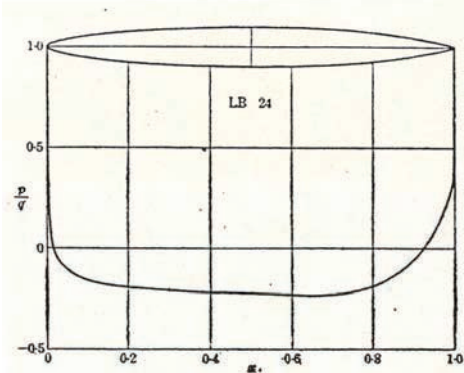
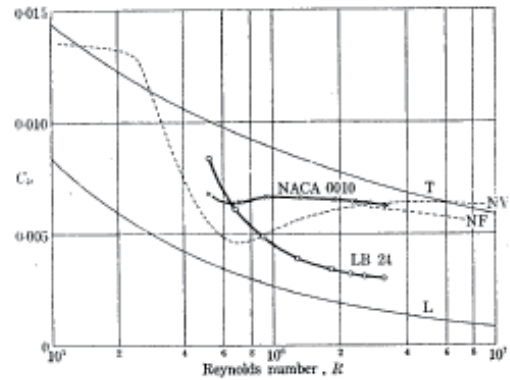

 Fig.6. Laminar Wing (upper)⁶⁾. Pressure vs. chord (lower).


Fig. 8. Variation of drag coefficient of the two symmetrical aerofoils with Reynolds number. The curves L and T represent the drag of a flat plate when the boundary layer is entirely laminar and entirely turbulent, respectively. The curves NV and NF represent the drag of the aerofoil N.A.C.A. 0009 tested in the N.A.C.A. Variable-Density Tunnel and Full-Scale Tunnel, respectively.

Fig.7. C_D vs. Re - diagram⁵⁾

conventional design the thickest part is at 25% chord. The wing section LB24 is designed so as to maintain laminar flow throughout a greater part of boundary layer of the wing. An aerofoil that is likely to delay transition from laminar to turbulent flow in the boundary layer will be that in which the lowest pressure occurs well back along the surface. Tani was 33 years old at this time (See Fig.7 for C_D).

Later, the laminar wing was used in a water-plane 強風 (Gale). In the next stage, it was adopted in 紫電 (Purple Lightning, an airplane). In 1943, Prof. Matsui (松井辰弥先生) designed 飛燕 (Flying Swallow) No.2, but with a wing section of NACA Series.

6. Isao IMAI (1914–2004)

Imai once recollected his young times in his own article, *Recollections of a Fluid Physicist*⁷⁾. He had a special interest in exact solutions to the Navier-Stokes equation from early times of his career (from 1936) of fluid mechanics. In 1951 when he was 37, Imai published a paper⁸⁾, “On the asymptotic behaviour of viscous fluid flow at a great distance from a cylindrical body, with special reference to Filon’s paradox”.

This was a very successful and influential work.. An analytical solution to the steady Navier-Stokes equation, $(u \cdot \nabla)u = -\nabla p + \mu \Delta u$, is sought with successive approximations. He started from a solution to the Oseen equation:

$$U \frac{\partial}{\partial x} u = -\nabla p + \mu \Delta u$$

which is thought to be valid asymptotically at great distances. Note that the Stokes equation,

$$0 = -\nabla p + \mu \Delta u$$

is valid at small distances:

One of his motivations was to resolve the Filon's paradox (1928), which says that the moment of force on a cylindrical body placed in a viscous stream, with nonzero lift, diverges logarithmically by the term ϕ_2 of expansion for the stream function Ψ (U denoting uniform flow U):

$$\Psi = Uy + \psi_1 + \psi_2 + \dots$$

He posed a question himself whether the solution which Filon used is really meaningless, for a viscous flow around a solid body, which is the second approximation next to the Oseen's solution for a sphere (1910) and Lamb's solution for a cylinder (1911):

Carrying out successive Oseen expansions to the next third stage ϕ_3 (of the order of $1/r$, where r is the distance from the body), Imai was able to show that no divergence occurs, and corrected an error of the previous study of Filon:

$$\Psi = Uy + \psi_1 + \psi_2 + \psi_3 + \dots$$

Thus, Oseen type of successive approximation is useful in solving the Navier-Stokes equation for viscous flows and gives a valid solution of far field.

It was well-known at his times that, for uniform viscous flow around a cylindrical body (2D problem), the velocity of solution of the Stokes equation diverges logarithmically with increasing distance, called the Stokes paradox.

On the other hand, there is a solution of the Stokes equation for a sphere (3D problem). However, there is no next-order approximation which behaves appropriately at infinity: Whitehead paradox (1889) for a sphere. Validity of Stokes solution is limited to a near field.

Imai's work is understood in two ways. Firstly, it is related to how to find a solution uniformly valid over whole field for a viscous flow past a cylinder in a uniform stream. Imai's exact asymptotic expression provided a base to solve numerically the Navier-Stokes equation for a viscous flow past a body.

In fact, one of his research assistants (M. Kawaguti, later, Professor, Keio Univ.) carried out numerical computation of a steady flow past a circular cylinder in a uniform stream at a Reynolds number 40 (with respect to the diameter) by using a hand-calculator (Tiger). It took about one year and a half for him to obtain a final result (1953). This was a very successful achievement of direct numerical simulation of the Navier-Stokes equation which succeeded in visualizing standing eddies behind the body for the first time, well before the computer age from 1980.

From mathematical point of view, there remains still an essential obstacle. Although the Oseen approximation gives a valid asymptotic solution at large distances, it is

well-known that the boundary layer thickness adjacent to a solid body at a high R is scaled as $1/R^{1/2}$, whereas the Oseen solution gave the thickness erroneously scaled as $1/R$.

Thus, an idea of *decomposition of flow field* came up to the surface logically. *Near-field* is to be solved by the Stokes equation, while *far-field* to be solved by the Oseen equation. This formidable problem was resolved by the method of matched asymptotic expansions later in 1957 by two groups. The works of Imai (1951), and Tomotika-Aoi (1950) are cited by the paper of Proudman and Pearson (1957).

In summary, the numerical achievement of Kawaguti (1953) paved a path to finding uniformly valid solution of the Navier-Stokes equation, because his numerical result was the near-field solution to the Navier-Stokes equation matched to the far-field solution of Imai's solution. Moreover it coincided with the experiment of Taneda (1956). All these works of Japanese scientists were published before the year 1957 of the celebrated papers of the matched asymptotic expansions by Proudman-Pearson and Kaplun-Lagerstrom.

4. Summary

When we look back one hundred years of development of fluid mechanics research in Japan, we find a number of studies which were original and keeping their influences on the present age.

References

- 1) T. Terada: *Aeron. Res. Inst. Rep.* **3** (1928) 3.
- 2) von Karman: *Aeron. Res. Inst.*, Report, Miscell. No.37 (1927). [translated into Japanese]
- 3) L. Prandtl: *Aeron. Res. Inst.*, Report 65 (1930):
- 4) <http://www.ne.jp/asahi/airplane/museum/kouken.html>
古典航空機電脳博物館 Classic Airplane Museum
富士重工 and イラストレーター小池繁夫.
- 5) Tani and Noda: *Aeron. Res. Inst. Rep.* No.190 (1940).
- 6) Tani and Mituisi: *Aeron. Res. Inst. Rep.* No.198 (1940).
- 7) 今井功: 日本物理学会誌 **51** (1996), 50 年をかえり
みる: ある物理学者の軌跡.
I. Imai: *Bulletin of Phys. Soc. Japan* **51** (1996), no.11
- 8) I. Imai: *Proc. R. Soc. Lond. A* **208**, 487 (1951).
- 9) P.G. Drazin and W.H. Reid: *Hydrodynamic Stability*,
Cambr. Univ. Press, 1981.

T. Kambe:

Member at Science Council of Japan (Tokyo),
Member of IUTAM Bureau,

kambe@ruby.dti.ne.jp

<http://www.purple.dti.ne.jp/kambe/>

An investigation on airfoil tonal noise generation

M. Tuinstra^{*}, T. Atobe^{**}, S. Takagi^{**}

^{*} National Aerospace laboratories (NLR),

^{**} Japan Aerospace Exploration Agency (JAXA)

ABSTRACT

The generation of tonal noise by airfoils has been a continuing problem of which the overall mechanism still remains yet to be uncovered. Results of an experimental investigation on tonal noise generation are presented. Quantitative measurements were obtained by use of hotwire and microphone. Furthermore, a flow visualization of the phenomenon was carried out by use of a smoke wire technique. Based on these experiments, a detailed description of the flow close to the trailing edge is obtained. The sound generation process takes place on the pressure side in the near-trailing edge region, where a thin layer of separated flow exists, which is essential to the mechanism. A Kelvin-Helmholtz instability appears to be the cause of the vortex generation. The interaction of shedding eddies with the trailing edge, resulting in the emission of pressure waves, represents the noise source. Events on the suction side are found to be of no significant influence to the sound generation mechanism. The role of TS waves in the sound generation process is re-evaluated and a novel self-excited feedback loop is proposed to explain the occurrence of tonal noise generation.

Key Words: Airfoil tonal noise, trailing edge noise

1. Introduction

The generation of tonal noise by airfoils has been a continuing problem of which the complete mechanism still remains yet to be uncovered. In the 90's numerous large wind turbine parks were erected as to provide an alternative clean power source. In several cases it was found however, that despite no pollutant gas were emitted, now the tonal noise generation by the turbines presented a large hinder to the direct environment. In various other cases tonal noise generation is known to occur: e.g. on airfoils operating at moderate Reynolds number, small aircrafts, rotors and fans. By the present study, it has been attempted to obtain a deeper understanding of the fundamentals of the tonal noise generation process and offer a hypothesis on why tonal noise emission occurs.

2. Experimental Procedure

The experiments were carried out in a closed-loop, closed-test-section, low turbulence wind tunnel facility at the JAXA Aerodynamics Research Group. The wind tunnel is designed to operate at wind tunnel velocities from 1 to 65 m/s and provides a test section of 550 x 650 mm². The measurements were carried out using a NACA0015 airfoil with a cord length of 0.4 m. The model was horizontally fitted in the test section, at a fixed angle of attack of 5 degrees, completely spanning the wind tunnel section. Measurements were conducted at a free stream velocity of 14.5 m/s. Acoustic measurements were

obtained by a Brüel&Kjær condenser microphone type 4138. The microphone was placed approximately 10cm behind airfoil on the lower wind tunnel wall to avoid flow interference. Velocity measurements were extracted by use of a traverse mounted single wire hotwire. Flow visualization was carried out by use of a smoke wire technique. For this purpose a 50µm diameter, constantan wire was placed in the flow, 1.5 cm upstream the trailing edge at approximately 1 mm distance from the airfoil surface. In order to illuminate the flow a thin laser sheet was used. A Vision Research high speed camera, type Phantom v4.2, enabled image capturing at 2000 Hz, which allowed the detailed recording of the sound generation process

3. Results and Discussion

Prior to quantitative measurements a smoke wire flow visualization was performed in order to acquire a qualitative description of the events occurring on the pressure-side, near-trailing edge region. Smoke wire recordings were made by high speed camera, synchronized with sound measurements. Figure 1 shows a schematic of one cycle of the tonal noise emission process as observed in the smoke wire recordings. It was noted that a separated region exist at the trailing edge, which extends upstream to approximately 10% cord.

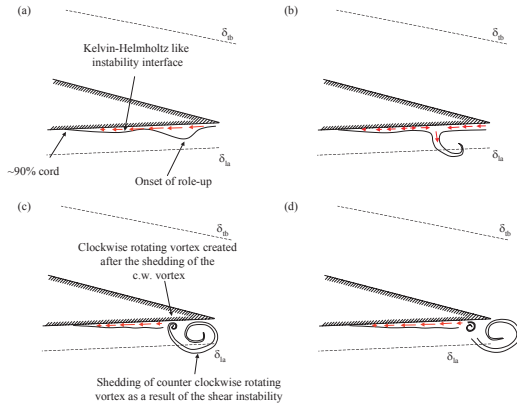


Figure 1: Schematic of the tonal noise generation process

A shear layer instability, as a result of the separated region, causes the rapid amplification of a disturbance wave, which roles up to form a vortex which is shed from the trailing edge. Smoke wire visualization further revealed that no vortex shedding occurs from the suction side and therefore the vortex street behind the airfoil must be a result of wake instabilities.

Hotwire measurements on the pressures-side of the airfoil, presented in Figure 2, show the development of an inflectional velocity profile, most strongly observed at 97% cord. Further downstream, the transfer of high momentum fluid by the shedding vortex, causes the flow to intermittently reattach, which is observed as a weakening of the inflectional property of the velocity profile.

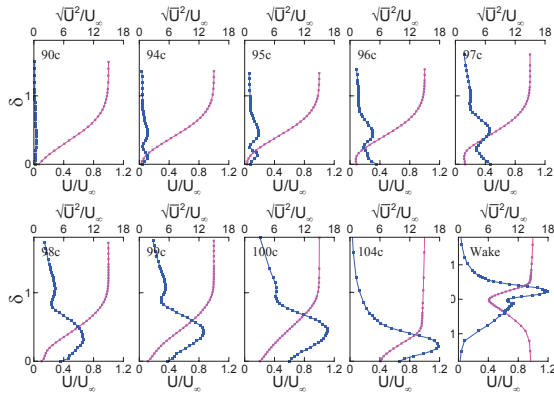


Figure 2: Pressure side velocity and RMS profiles

The RMS profiles show a rapid amplification of the flow fluctuations to 16% of the free stream velocity in a range covering only 10% cord (4 cm). A triple deck structure is observed. The first peak is found closest to the wall, which is associated with separated flow region. A second peak is found at roughly 0.4δ . A third RMS-peak is found to occur

outside the boundary layer at 1.1δ as a result of the vortex extending outside the boundary layer as it sheds from the trailing edge. Phase diagrams also reveal this triple deck structure, showing three regions of correlated fluctuations corresponding with the RMS peaks.

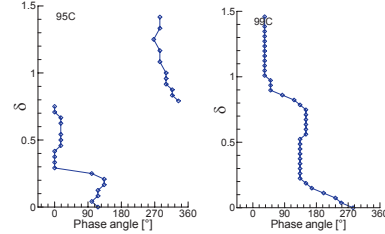


Figure 3: Phase correlation

A new hypothesis on airfoil tonal noise generation is proposed: The sound generation process is confined to the near trailing edge region. Laminar flow separation in this area, provides for a highly unstable flow allowing the rapid amplification of disturbances, which form a vortex which is shed from the trailing edge. A feedback loop is proposed to impose periodicity on the flow. As a vortex is shed, the trailing edge/vortex interaction causes the emission of a pressure wave disturbance. As it propagates upstream it is received at the onset of the instability region, where it initiates the growth of the following vortex.

Realizing the importance of the separation region to the tonal noise generation process a possible explanation of the jumps in the velocity-frequency dependency is deduced. The separation length is found to be in the order of 10% of total cord length. Disturbance wavelength increases with free-stream velocity. When the disturbance-wavelength exceeds that of the separation length it is no longer possible for vortex role-up to occur, resulting in a vorticity imbalance. This enforces the flow disturbances to occur at a shorter wavelength in order to shed excess vorticity. The sudden change in wavelength would be observed as a jump in the velocity-frequency dependency.

4. Summary

An experimental characterization of the flow of the near-trailing edge region by means of by hotwire and smoke wire was successfully carried out. A self-excited feedback loop is proposed in order to explain the periodicity, necessary for tonal noise emission. By considering disturbance wavelength with respect to separation length it is attempted to account for jumps observed in the emitted frequency-velocity dependency.

Detailed Flow Field around a Leading-Edge Slat at Low Reynolds Numbers

Sanehiro MAKIYA*, Ayumu INASAWA* and Masahito ASAI*

*Dept. of Aerospace Eng., Tokyo Metropolitan University,

Abstract

Flows around a leading-edge slat are investigated experimentally at Reynolds numbers $Re \leq 5.2 \times 10^5$. When the slat operates to suppress the leading-edge stall, a periodic vortex shedding occurs due to the instability of laminar wake of the slat at Reynolds numbers less than 2.1×10^5 . The Reynolds number variation of the shedding frequency is not unlike that of the circular-cylinder wake at low Reynolds numbers. For $Re \geq 2.3 \times 10^5$, prominent spectral peaks appear both in the velocity fluctuations and sound-pressure and the frequency of such distinguished noise is found to be proportional to $U_\infty^{0.84}$ as reported in the experiment on the sound generation in a single-element airfoil at small angles of attack, suggesting a possibility of feedback loop between the shear layer instability immediately upstream the slat trailing-edge and the generated sound.

Key Words: Leading-edge slat, Instability, Vortex shedding, Aeroacoustics

1. Introduction

The leading-edge slat is a high-lift device widely used together with the rear flap to suppress the stall of aircraft at high angles of attack. Numerous experimental and computational studies have been conducted on the aerodynamic characteristics of multi-element airfoil⁽¹⁻³⁾. On the contrary to the high-lift achievement, the leading-edge slat gives rise to additional airframe noise, which may be a serious problem in advanced aircraft design. Indeed, slat-generated noise is known to be a significant contributor to the airframe noise during the landing phase, and its reduction is one of the most important and challenging technologies for the aircraft development.

Recent computational studies⁽⁴⁻⁸⁾ on the aeroacoustics of multi-element wing indicate that slat noise consists of broadband low- and mid-frequency components probably originating in the slat cove and narrowband higher-frequency components generated at and around the slat trailing-edge. However, few experiments have been reported on the flow field and the related aeroacoustics of the slat. In the present experimental study, in order to better understand the flow phenomena and noise generation, the flow field around the slat is investigated in detail.

2. Experimental setup and procedure

The experiment is conducted in an open-jet type wind tunnel with exit cross-section of 600 mm (height) \times 300 mm (span). Experimental setup is illustrated in Fig. 1. Two Plexiglas sidewalls are installed in the test section to keep two-dimensionality

of the main stream though upper and lower areas are opened. A three-element wing model is set between the sidewalls. The configuration of the wing model is illustrated in Fig. 2. The stowed wing consists of a NACA23012 airfoil section and its chord c is 300 mm. In the present experiment, the wing is kept unflapped and only the slat is displaced along the chord line of the stowed wing section.

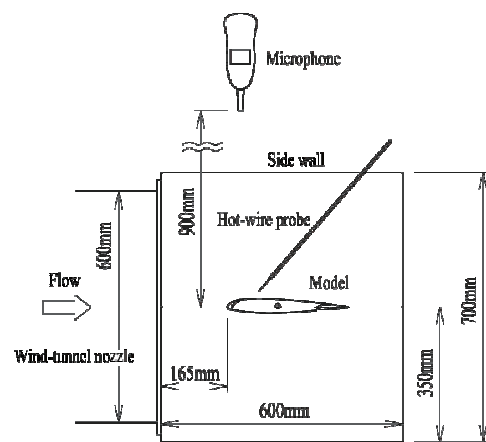


Fig. 1. Experimental setup.

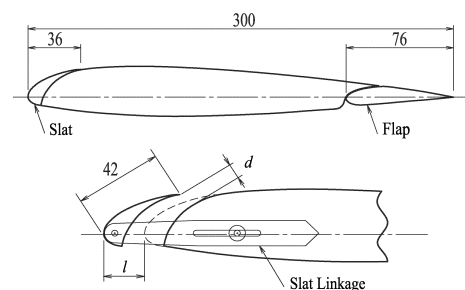


Fig. 2. Configuration of three-element wing model.

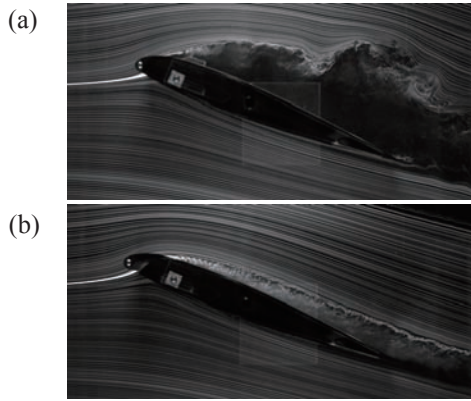


Fig. 3. Flow past NACA23012 airfoil at $\alpha = 20^\circ$, $Re = 8.2 \times 10^4$. (a) No slat gap, (b) slat gap $d = 3.1$ mm ($l = 10$ mm).

The velocity measurements are made using a constant-temperature hot-wire anemometer. To measure aerodynamic noise, a high-precision microphone (LION NL-22) is set 900 mm above the slat trailing edge. Flow visualization is done by means of smoke-wire technique. Two smoke-wires are stretched in the vertical and spanwise directions and still camera shots are taken with stroboscopic light. Movies of smoke-wire visualization are also taken by using a high-speed digital video camera.

The free-stream velocity U_∞ ranges from 2 m/s to 25 m/s and the corresponding Reynolds number based on the stowed-geometry wing chord is $Re = 4.2 \times 10^4$ to 5.2×10^5 .

3. Results and discussion

In the case of stowed configuration, the airfoil stall occurs at angles of attack α higher than 18° , as shown in Fig. 3(a) which visualizes the flow at $\alpha = 20^\circ$ at $Re = 8.2 \times 10^4$. When the slat gap is adjusted properly, the leading-edge stall is completely suppressed at the same angle of attack, as shown in Fig. 3(b). Fig. 4(a) shows a close-up view of the smoke visualization picture of the flow around the slat. When the leading-edge stall is suppressed, we can see a quite periodic vortex shedding from the trailing edge of the slat. In the figure, a laminar separation bubble in the cove region is also seen clearly. Owing to the low Reynolds number $Re = 8.2 \times 10^4$, the separation bubble in the cove remains laminar without noticeable development of Kelvin-Helmholtz instability. Fig. 4(b) displays a top view of visualization, showing that the shedded vortices are almost two-dimensional.

Figs. 5(a) and (b) display the y -distributions of time-mean velocity U and r. m. s. value of velocity

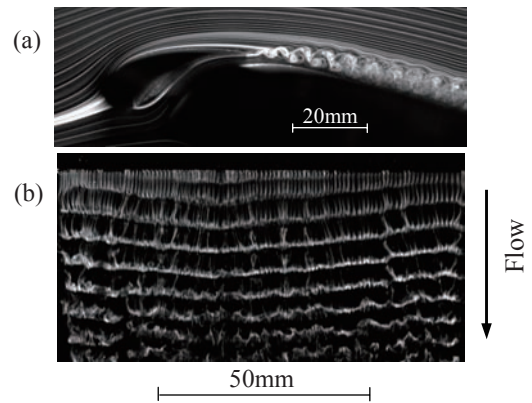


Fig. 4. Flow visualization of the slat wake ($d=3.1$ mm) at $\alpha = 20^\circ$, $Re = 8.2 \times 10^4$. (a) Side view, (b) top view.

fluctuation u' in the near-wake region, 1 mm and 4 mm downstream the slat trailing-edge, respectively. Here, the normal-to-wall coordinate y measures from the surface of the main element. As seen from Fig. 5(a), both the flows passing upper and lower surfaces of the slat accelerate to $1.5U_\infty$. Consequently, the slat wake seems to be that of an airfoil in a uniform flow, though the upper shear layer is thicker than the lower shear layer. A reversed flow region appears between $y = 3.6$ mm and 4.6 mm, as seen from the fact that the velocity decreases to zero at $y = 3.6$ mm and 4.6 mm and increases slightly between these two y -positions: Note that the hot-wire can not sense the flow direction. The velocity distribution with the reversed flow has the nature of absolute instability, which is prerequisite for the onset of global instability, i.e., onset of the periodic wake oscillation⁽⁹⁾. The reversed flow disappears at the location 4 mm downstream the slat trailing-edge as shown in Fig. 5(b). The wake width (defined as the half-value width) is about 1.5 mm so that the streamwise distance of the reversed flow region is not larger than three times the wake width. The present result shows that such streamwise extent of reversed flow region is sufficient for the occurrence of global instability. The peak values of u' in the upper and lower shear layers already exceed $0.15U_\infty$ at this location, which corresponds to the development of wake vortices visualized in Figs. 3 and 4. In Fig. 5(b), we also notice that the two peaks in the u' distribution (at $y = 3.5$ mm and 4.6 mm) are not the same in magnitude, which is due to the difference in the intensity of the velocity gradient (or the shear layer thickness).

Next examined is how the disturbance frequency changes with the free-stream velocity. To avoid

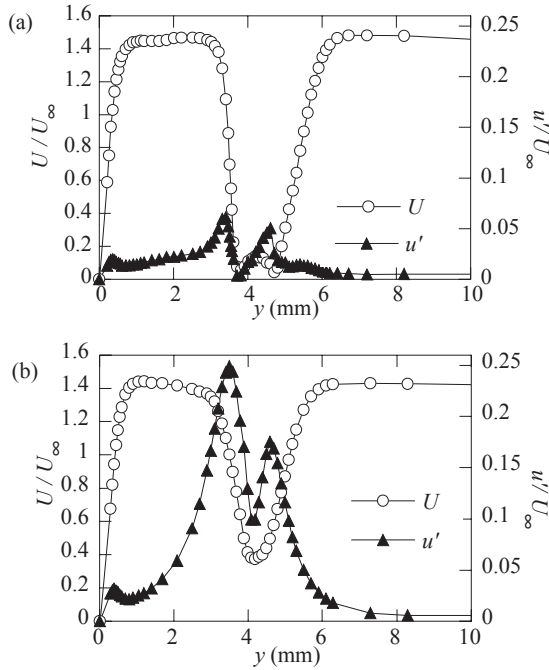


Fig. 5. Mean velocity U and r. m. s. value of velocity fluctuation u' , (a) 1 mm and (b) 4 mm from the slat trailing-edge at $U_\infty = 4$ m/s ($Re = 8.2 \times 10^4$).

possible interferences with the flow, particularly the flow between the slat and the main wing-element, the hot-wire probe is set outside the slat wake (10 mm downstream the slat trailing-edge and $y = 6.4$ mm). Fig. 6 illustrates the relation between the free-stream velocity and the dominant disturbance frequency (its fundamental component). A discontinuity in the dominant frequency occurs between $U_\infty = 10$ m/s ($Re = 2.1 \times 10^5$) and 11 m/s ($Re = 2.3 \times 10^5$). This suggests that the mechanism of vortex generation changes around there ($U_\infty = 10 \sim 11$ m/s). Fig. 7 shows that the Strouhal number based on the thickness of slat trailing-edge t_s ($= 0.5$ mm) $St (= ft_s/U_\infty)$ against the trailing-edge-thickness Reynolds number $Re_{ts} (= U_\infty t_s/\nu)$ for $U_\infty \leq 10$ m/s. St increases gradually to approach 0.12 for $Re_{ts} > 200$. Such a variation in St against Re is quite similar to the case of circular-cylinder wake⁽¹⁰⁾.

Figs. 8(a) and (b) show the power spectrum of velocity fluctuation and the sound pressure level (SPL) distribution (measured by the microphone above the slat trailing-edge), respectively. The measurements are made at $U_\infty = 6$ m/s ($Re = 1.3 \times 10^5$). We can see distinct peaks at $f = 1416$ Hz and at its harmonic frequencies in the power spectrum of the velocity fluctuation (Fig. 8a). This no doubt results

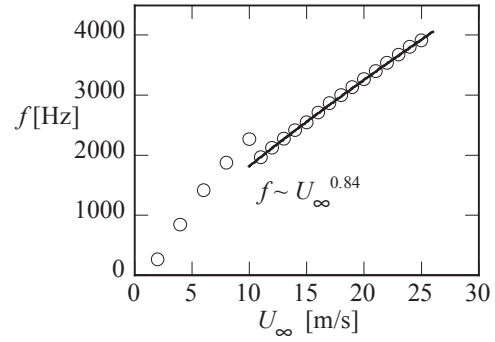


Fig. 6. Noise frequency vs. free-stream velocity.

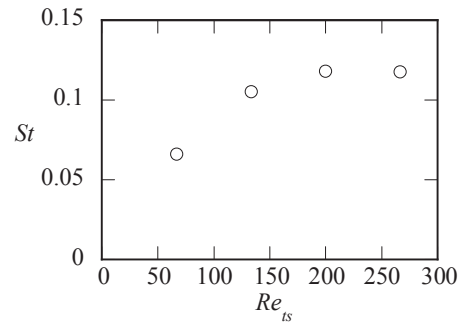


Fig. 7. Strouhal number vs. Reynolds number for $U_\infty \leq 10$ m/s ($Re \leq 2.1 \times 10^5$). t_s is the thickness of the slat trailing-edge.

from the absolute instability of slat wake as mentioned above. On the other hand, we see no distinct peak for the SPL spectrum (Fig. 8b). Thus, sound generation is extremely weak at this low Reynolds number even though the strong periodic vortex shedding already occurs.

Figs. 9(a) and (b) show the similar spectra measured at higher free-stream velocity $U_\infty = 19$ m/s ($Re = 4.0 \times 10^5$). Prominent peaks are observed both in the velocity spectrum and the SPL distribution at $f = 3141$ Hz. Such sharp peaks always appear for $U_\infty \geq 11$ m/s ($Re \geq 2.3 \times 10^5$), and the peak frequency (fundamental component) is found to be proportional to $U_\infty^{0.84}$, as already shown in Fig. 6.

On this concern, it should be referred to the experiments⁽¹¹⁾ on the tonal noise from the NACA0012 airfoil at small angles of attack, where the discrete-tone frequency is proportional to $U_\infty^{0.8}$. In that experiment, the shear layer instability of Kelvin-Helmholtz type was observed on the pressure side of the airfoil immediately upstream the trailing edge, and it was pointed out that the frequency of generated sound was close to that of the most amplified disturbance calculated from the linear instability of

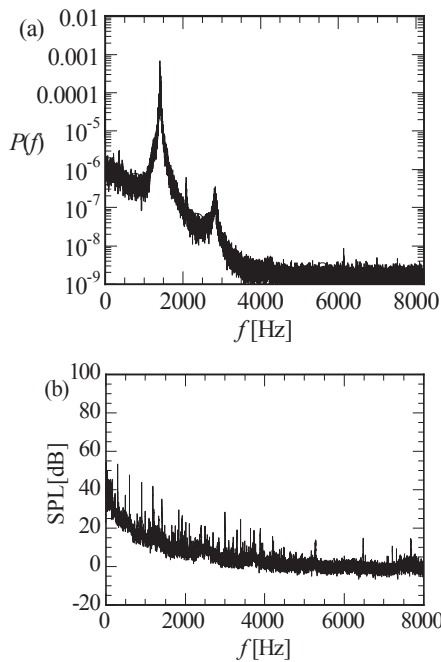


Fig. 8. Power spectrum of the velocity fluctuation in (a) and SPL distribution in (b) at $Re = 1.3 \times 10^5$ ($U_\infty = 6$ m/s).

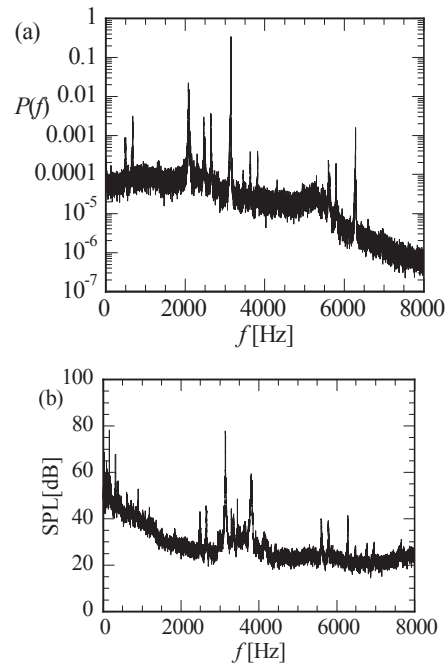


Fig. 9. Power spectrum of the velocity fluctuation in (a) and SPL distribution in (b) at $Re = 4.0 \times 10^5$ ($U_\infty = 19$ m/s).

inflectional velocity profiles near the trailing edge though stability analysis could not explain why the narrow-band peak appears in the spectra. A possible mechanism causing such a discrete peak is the feedback loop through the receptivity process between the shear layer instability and the generated sound though it is not clarified yet.

4. Conclusions

Flows around a leading-edge slat have been investigated experimentally at low Reynolds numbers $Re = 4.2 \times 10^4$ to 5.2×10^5 . The observations have been focused on the flows at a high angle of attack $\alpha = 20^\circ$ where the airfoil undergoes the leading-edge stall for the stowed-geometry case. For $Re \leq 2.1 \times 10^5$, a periodic vortex shedding due to the global instability of the slat wake, which is not unlike in the circular-cylinder wake, occurs, but the associated sound generation is very weak. For $Re \geq 2.3 \times 10^5$, on the other hand, distinguished almost-discrete tone appears and its frequency is proportional to $U_\infty^{0.84}$. Such strong sound generation suggests a possibility of feedback mechanism between the shear layer instability immediately upstream of slat trailing edge and the generated sound, but it still remains open and further investigation is needed.

References

- (1) Nakayama, A. et al.: AIAA J. 28 (1) (1990) pp. 14-21
- (2) Yasuhara, M. et al.: Trans. Jpn. Soc. Aeron. Space Sci., 33 (1991) pp.218-233.
- (3) Maddah, S.R. et al.: Exp. Thermal and Fluid Sci., 25 (2002) pp.651-658.
- (4) Murayama, M. et al.: Trans. Jpn. Soc. Aeron. Space Sci., 49 (2006) pp.40-48.
- (5) Khorrami, M.R. et al.: AIAA J., 38 (11) (2000) pp.2050-2058.
- (6) Khorrami, M.R. et al.: AIAA J., 40 (7) (2002) pp.1284-1291.
- (7) Khorrami, M.R. and Choudhari, M.M.: NASA/TM-2003-212416 (2003).
- (8) Imamura, T. et al.: 12th AIAA/CEAS Aeroacoustics Conference-2006-2668, (2006).
- (9) Huerre P.: Annu. Rev. Fluid Mech., 22 (1990) pp. 473-537.
- (10) Williamson C. H. K.: J. Fluid Mech., 206 (1989) pp.579-627.
- (11) Nash, C. E. et al.: J. Fluid Mech., 382 (1999) pp.27-61.

FLOW CONTROL with PITCHING MOTION of UAV using MEMS FLOW SENSORS

H.TOKUTAKE*, S.SUNADA*, J.FUJINAGA* and Y.OHTSUKA*

*OSAKA PREFECTURE UNIVERSITY

ABSTRACT

A new pitch controller for our developed small airplane was designed, and its ability was confirmed by simulation. In the pitch controller, outputs from the MEMS flow sensor and the transfer function determined by the results of the wind tunnel tests are used. MEMS technology is a key technology of this pitch controller.

Key Words: UAV, pitch control, MEMS flow sensor

1. Introduction

We have developed a small and lightweight airplane. The airplane has a flight controller and can make an autonomous flight. The flight controller was also developed by us in cooperation with Y'sLab Corp. The details of the flight controller are shown in Ref.1. At present, the pitch control is made as follows : The pitch rate is measured by a rate gyro. The angle of elevons is varied so that the longitudinal dynamics is stabilized. This pitch controller can stabilize the pitch motion of the aircraft. For more accuracy of pitch control, we are proposing a new method of pitch control where the flow measurements with MEMS sensors are made. In this paper, the results in the wind tunnel tests with the MEMS sensors are shown and a flight controller based on the new method is designed.

2. Experiment Procedure

Figure 1 shows our developed airplane². The span length and the weight are 40cm and 270g, respectively. It was found by our previous wind tunnel test that this airplane makes a trimmed flight when the pitch angle, the elevon angle and the forward velocity are 11deg, -15deg and 5m/s, respectively. The momentum of this

aircraft, which is given by multiplying the mass by the forward velocity, is so small that it does not injure us seriously when it hits on us. The size, weight and forward speed were determined for safety.

Figure 2 shows a photograph taken by an onboard camera. The number of picture elements is 2million. The image is so clear that the airplane with the onboard camera can be used for getting information from a high altitude.

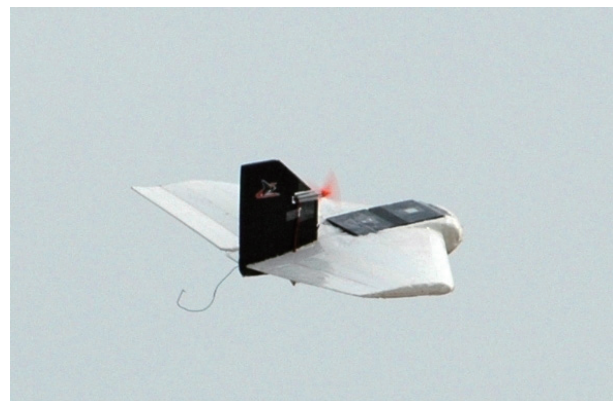


Fig.1 Our developed airplane



Fig.2 A photograph taken by an onboard camera

Figure 3 shows a flow sensor mounted on a wing of the airplane for a new pitch controller. The flow sensor is composed of a chip, which is removed from the commercial flow sensor (D6F-W04A1;OMRON), and a vinyl cover over the sensor on the chip. The cross section of the vinyl cover is nearly semicircle and its diameter is about 5 mm. The output from the sensor can be related to a flow volume through the tunnel by the vinyl cover. And the output from the sensor is positive and negative when the flow goes from A to B and from B to A, respectively. The arrangement of the four flow sensors are shown in Fig.4.

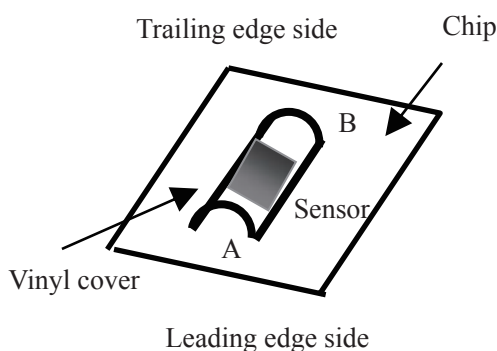


Fig.3 MEMS flow sensor

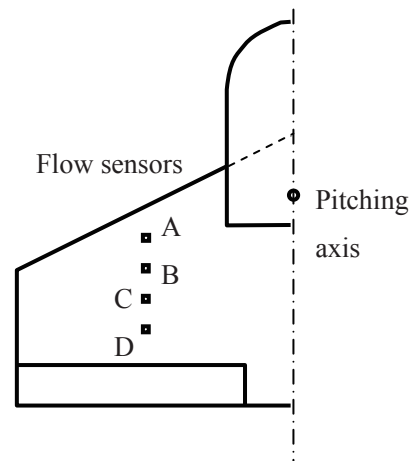


Fig 4. Arrangement of sensors

We made two kinds of wind tunnel tests about the airplane with the sensors on the wing. In both the tests, the airplane was set in a wind tunnel whose wind velocity was 3m/s. The wind velocity is a little smaller than the forward velocity at the trimmed flight stated above. However, the results obtained by these wind tunnel tests are available for a flight with the forward velocity of 5m/s, which is a value of the trimmed flight. This is because the Reynolds number effect on the transfer function and the constraint condition used in a new pitch controller, which will be stated later, are expected to be small.

The first measurements, where the airplane had no motion, were made as follows: The elevon angle was fixed and the angle was -15deg, which is for the trimmed flight. The measurements were made as a parameter of the pitch angle of airplane. The second measurements, where the airplane had pitch motion, were made as follows: The pitch angle of the airplane was varied by a servo motor and the axis of the pitch motion is close to the center of gravity of the airplane. The pitch angle was recorded with a potentiometer.

3. Results and Discussion

Figure 5 shows the results of the first test, where the airplane had no motion. This figure shows the

relation between the pitch angle and the outputs from the four sensors. Note that these outputs cannot be compared between the sensors because the characteristics of the sensors are not common. The output from the sensor C is 0V when the pitch angle is 11deg, which is an angle of attack for the trimmed flight. So, we selected the output from sensor C as an indicator for pitch control whose details will be stated later. This is because the output obtained at the wind velocity of 3m/s is equal to that at the wind velocity of 5m/s, which is the forward velocity at the trimmed flight, just when the former value is equal to 0V.

Figures 6 and 7 show the results of the second test where the airplane had pitch motion. Figure 6 shows the time variation of pitch angle. The time variation includes components with various frequencies. Note that the maximum pitch angle is less than the stall angle of 18deg. Figure 7 shows the measured output from sensor C. The transfer function indicating the relation between the pitch angle and the measured output from sensor C are given by

$$G_a(s) = \frac{-2.2 \times 10^{-2} s^3 - 8.7 s^2 - 7.1 \times 10^2 s - 5.0 \times 10^{-4}}{s^3 + 2.3 \times 10^2 s^2 + 1.5 \times 10^{-4} s + 1.4 \times 10^{-5}}$$

We designed a new controller for pitch motion, where the output of flow sensor C and the transfer function are used. The actuators in this controller are also the elevons as well as in the present pitch controller. And the new controller is expected to be used together with the present pitch controller for high accuracy in the pitch control. It was confirmed by simulation that the pitch angle can be converged on the value at the trimmed flight quicker by using simultaneously both the present controller and the new controller than by using no controller, when the external pitching moment is applied on the airplane with the forward speed of 5m/s. Note that the airplane itself has dynamic stability and that the pitch angle can be converged on the value at the trimmed flight

without a controller. The details of the new controller will be indicated in Ref.3.

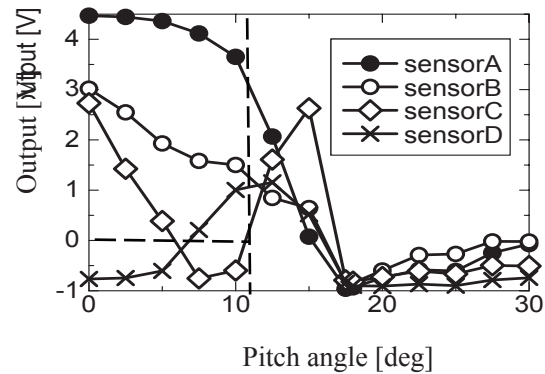


Fig.5 Output of sensors

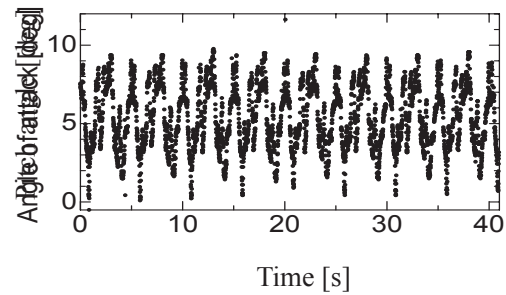


Fig.6 Time-variation of pitch angle

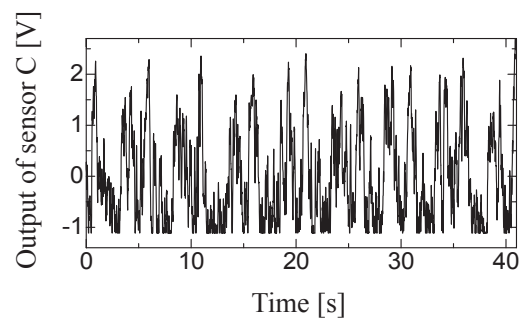


Fig.7 Time-variation of output of sensor C

4. Summary

A new pitch controller for our developed small airplane was designed, and its ability was confirmed by simulation. In the pitch controller, output from the MEMS flow sensor and the transfer function

determined by the results of the wind tunnel tests are used. MEMS technology enables this pitch controller. In future, the ability of the pitch controller will be confirmed by a flight test.

References

- 1) H.Ito, H.Tokutake, S.Sunada and H.Sumino, Proceedings of AHS International Meeting on Advanced Rotorcraft Technology and Life Saving Activities. pp. T-243-2-1-T-243-2-4 (2006).
- 2) J. Fujinaga, H.Tokutake and S.Sunada, Proceedings of the 38th Annual Meeting of JSASS (2007), in Japanese, in press.
- 3) H.Tokutake, S.Sunada and J. Fujinaga, Proceedings of the AIAA Guidance, Navigation and Control Conference and Exhibit (2007), in press.

Measurements of Mass Flux and Concentration in Supersonic Air/Helium Mixing by Hot-Wire Anemometry

Akira KONDO*, Shoji SAKAUE* and Takakage ARAI*

* Graduate school of Aerospace Engineering
Osaka Prefecture University, Sakai, Osaka, Japan

ABSTRACT

In the present study we made efforts to realize a measurement method of mass flux and concentration in supersonic air/helium flow in order to clarify the mixing process. The measuring equipment, which was used for measuring the fluctuations of mass flux and concentration, is consisted of a double-hot-wire probe and CVA (Constant Voltage Anemometer) circuit with 500 kHz bandwidth. The distance between two wires of double-hot-wire probe was 0.16 mm. By using the same material as the hot wire, the correlation coefficient between each hot wire output in Mach 2.4 supersonic flow with the pair of streamwise vortices was about 0.9. Therefore, we confirmed that the flows captured by two wires were almost the same and our device can capture the coherent structure up to 1 mm in Mach 2.4 supersonic flow. When we use the two kinds of wires with the different responses to the variations of mass flux and helium concentration, we can find the air/helium mixing flow field using the calibration maps of each wires. In the present study, we used the two tungsten wires with 5 μm and 3.1 μm in diameter as the double-hot-wire probe and measure the mean mass flux and helium concentration in supersonic air/helium mixing layer in order to improve our measuring method.

Key Words: Supersonic Mixing, Mixing Enhancement, Hot-Wire Measurement, CVA (Constant Voltage Anemometer)

1. Introduction

The measurement of instantaneous mixing process in supersonic flow is great important on supersonic mixing enhancement such as development of scramjet engine. The quantitative measurement methods for fluctuating mass flux and concentration have been proposed by Xillo et al.¹⁾ and Arai et al.²⁾. But they have not been established yet because of the lack of time resolution. The purpose of this study is to establish the instantaneous quantitative measurement method for mass flux and concentration of mixing flow field.

2. Experimental apparatus and procedure

The principle of our measurement method is almost the same method that Harion et al.³⁾ have established in subsonic flow. Our device is consisted of double-hot-wire probe, as shown in Fig. 1, and CVA (Constant Voltage Anemometer) circuit with 500 kHz bandwidth. The double-hot-wire probe needs two kinds of wires with different characteristics of heat transfer. The heat balances of each wire are written as follows,

$$\frac{V_{wi}^2}{R_{wi}(R_{wi} - R_{ai})} = A_i(c) + B_i(c)\sqrt{\rho u} \quad (i = 1, 2) \quad (1)$$

where V_w is the voltage across the hot wire, R_w is the resistance of the hot wire at the operating temperature, R_a is the resistance of the unheated wire at ambient temperature, ρu is the mass flux, and c is the concentration of the fuel gas. In this study, we use helium gas as pseudo fuel. Left side of the eq. (1) indicates the power dissipation ratio (PDR) of the hot wire. Eliminating the square root of the mass flux from eq. (1), we obtain the following iso-concentration equation.

$$PDR_1 = \frac{B_1(c)}{B_2(c)} PDR_2 + A_1(c) - \frac{B_1(c)}{B_2(c)} A_2(c) \quad (2)$$

From eq. (2), we can detect the helium concentration c . Substituting the obtained c into eq. (1), mass flux ρu is obtained.

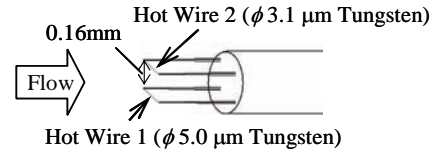


Fig. 1 Double-hot-wire probe.

3. Problems of the measurement method

There are three problems in our measurement method for instantaneous mixing process in supersonic flow, that is, calibration, spatial resolution and thermal lag of hot wire response. In order to resolve these problems, we carried out the following experiments.

3.1 Calibration method

The coefficients A and B in eq. (1) are determined by the hot wire calibration for mass flux ρu and concentration c . It is desirable that the hot wire is calibrated in the wind tunnel in which the measurements are conducted and for the wide variations of mass flux and concentration by as small amount of mixed gas as possible. Thus, we used the sonic nozzle calibration apparatus as shown in Fig. 2. Air/helium mixed gas is blown down through the circular convergent nozzle whose exit diameter is 5 mm, and the hot wire is calibrated at the nozzle exit where the speed of mixed gas reaches Mach 1. By using the sonic nozzle apparatus, we can calibrate the hot wire for the wide variations of mass flux by the small amount of the mixed gas. However, we must confirm that the calibration results can be applied to the measurements in supersonic flow. Figure 3

shows the comparison between the calibration results by using the sonic nozzle and in the supersonic turbulent boundary layer at Mach 2.4. As seen from Fig. 3, both results are in good agreement and the correlation coefficient is 0.997. Thus, we can conclude that the calibration results of the sonic nozzle can be applied to the measurements in supersonic flow.

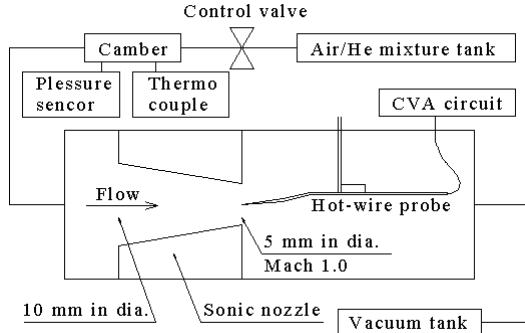


Fig. 2 Sonic nozzle calibration apparatus.

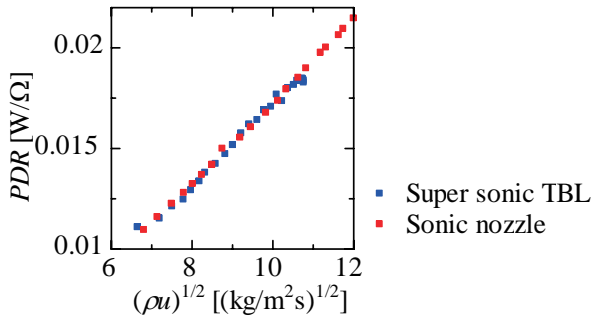


Fig. 3 Calibration results in sonic flow and in Mach 2.4 supersonic turbulent boundary layer.

3.2 Spatial resolution

The each hot wire of the double-hot-wire probe can not measure at the same point due to its configuration. Therefore, the distance between the hot wires must be minimized. So we made the double-hot-wire probe whose distance between each wire was 0.16 mm and length of the wires was 0.5 mm. To confirm similarity of the outputs of the each hot wire, we measured the correlation coefficient between the each hot wire output in Mach 2.4 supersonic flow with two pairs of counter rotating streamwise vortices as shown in Fig. 4. Figure 5 shows instantaneous schlieren photograph of the flow field. The hot wire measurements were done at $x = 100$ mm, $2 \text{ mm} \leq y \leq 14$ mm, $z = 15$ mm. At $x = 100$ mm, the streamwise vortices grew up to $y = 13$ mm and the reflected shock wave passed at $y = 5$ mm. Figure 6 shows the correlation coefficients between the each hot wire output by using the same material. As seen from Fig. 6, the correlation coefficients at $5 \text{ mm} \leq y \leq 13$ mm were about 0.9. Thus, the flows captured by the two wires were almost the same and the flow structures in this region were larger than that in the near wall region. In other words, spatial resolution of our measurement method becomes the sensor size of the double-hot-wire probe $0.5 \text{ mm} \times 0.16 \text{ mm}$.

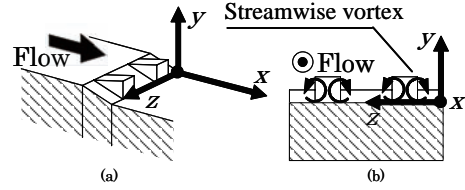


Fig. 4 Schematic of test section and coordinate system (a) overhead view (b) cross section: circular lines indicate streamwise vortices.

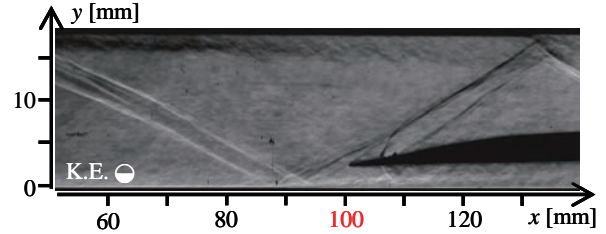


Fig. 5 Instantaneous schlieren photograph of Mach 2.4 supersonic flow with streamwise vortices.

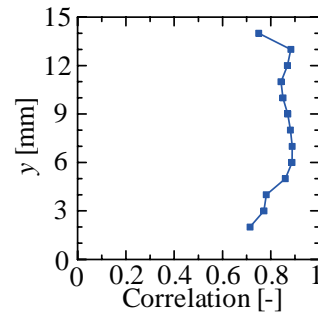


Fig. 6 Correlation coefficients between each hot-wire output.

3.3 Compensation for the lag of hot-wire

The hot wire has the heat inertia, so that the response of the hot wire delays to the fluctuations of the flow. In addition, the time constant of the hot wire response changes according to the flow condition. Thus, the thermal lags of the each hot wire must be compensated by the software processing method⁴.

It is well known that the resistance of the hot wire depends on temperature,

$$R_w = R_{ref} [1 + \alpha (T_w - T_{ref})] \quad (3)$$

and the time constant M of the hot wire by using the basic CVA circuit is written as follows,

$$M = \frac{a_w}{2a_w + 1} \cdot \frac{C_w}{\alpha R_{ref}} \cdot \frac{1}{I_w^2} \quad (4)$$

where a_w is the over heat ratio, C_w is the heat capacity of the hot wire, I_w is the current through the wire and R_{ref} is the resistance of the unheated wire at reference temperature T_{ref} . $C_w/\alpha R_{ref}$ is the constant value peculiar to the each wire, a_w and I_w can be determined by measurement. Therefore, the time constant of the hot wire can be determined if $C_w/\alpha R_{ref}$ is known. Figure 7 shows the typical response of the hot wire when a square wave is injected through input terminal of the CVA circuit. From the results as shown in Fig. 7, the time constant of the wire is determined as the time taken to reach the 63.2% of the final value, and $C_w/\alpha R_{ref}$ is known from eq. (4).

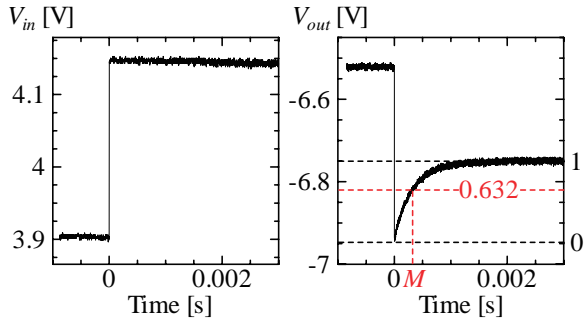


Fig. 7 Inputted step wave and first order lag response waveform of hot wire.

4. Measurements in mixing layer

4.1 Calibration for concentration and mass flux

In the present study, two kinds of tungsten wires were used for the double-hot-wire probe, their diameter were $5\ \mu\text{m}$ (W5) and $3.1\ \mu\text{m}$ (W3.1), respectively. Figure 8 shows the calibration results of the each wire. From these results, the coefficients A and B in eq. (1) were determined as cubic functions of helium concentration, as shown in Fig. 9. Figure 10 shows the calibration map of eq. (2) by using A and B in Fig. 9.

In order to estimate the error included in our measurement method, Fig. 11 shows the comparison between the measurement value and the actual value of mass flux and helium concentration. Here, the measurement value means the value calculated from PDR of each hot wire by using the calibration map as shown in Fig. 10. As seen from Fig. 11, it is found that the error in this method was less than $\pm 10\%$, except for the small PDR region where the iso-concentration lines were close to each other.

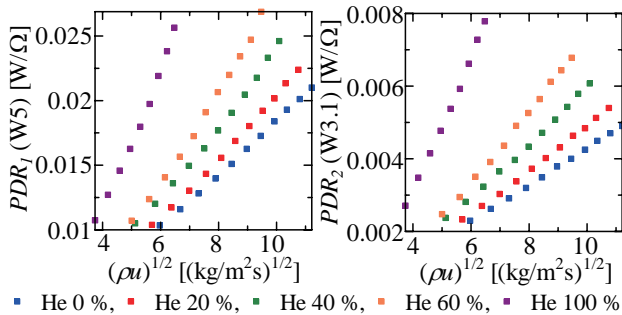


Fig. 8 Calibration results for helium concentration and mass flux.

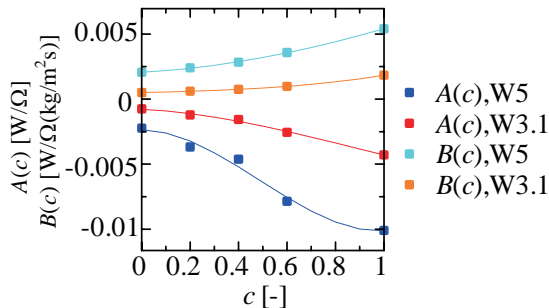
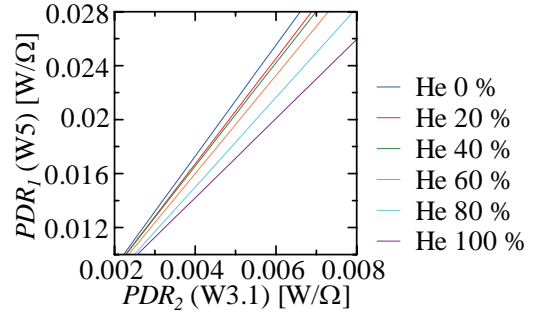

 Fig. 9 $A(c)$ and $B(c)$ determined by Fig. 8: each line indicate cubic approximation for helium concentration.


Fig. 10 Calibration map used for detecting helium concentration.

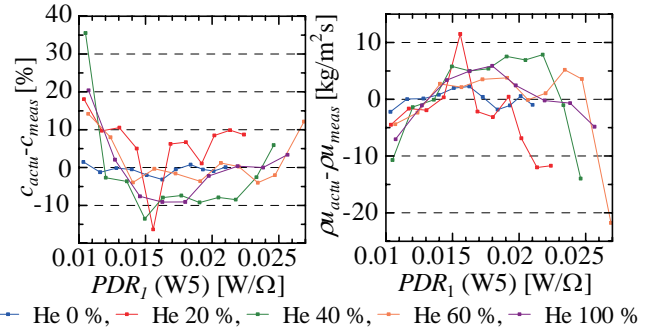


Fig. 11 Difference between measurement value and actual value of helium concentration and mass flux.

4.2 Results and Discussions

In order to demonstrate the usefulness and to clarify the accuracy of our method, we applied our method to the measurement of two dimensional air/helium mixing layer as shown in Fig. 12. Air and helium flow, whose Mach number were 2.4 and 0.8 respectively, were separated by a thin splitter plate and the mixing layer was formed at the plate downstream. The length of the test section was 400 mm, the height was 35.5 mm and the width was 30 mm. Figure 13 shows the instantaneous schlieren photographs of the mixing layer just behind the splitter plate. The measurements were conducted at $x = 30\ \text{mm}$ and $x = 100\ \text{mm}$, $-4\ \text{mm} \leq y \leq 10\ \text{mm}$ and $z = 15\ \text{mm}$.

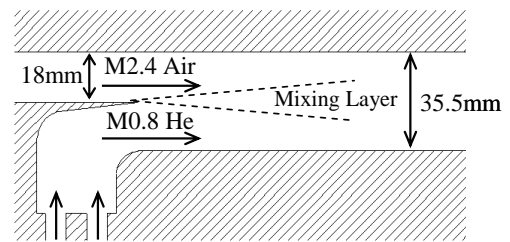


Fig. 12 Schematic of the mixing layer.

Figure 14 shows the mass flux and the helium concentration profiles of the mixing layer. In these figures, blue lines indicate the profile at $x = 30\ \text{mm}$, red lines are at $x = 100\ \text{mm}$. At these stations, air and helium do mix only at the center region of the mixing layer as seen from the schlieren photographs shown in Fig. 13, so that the helium concentration must be zero at the upper side of the mixing layer and must be one at the lower side of the mixing layer.

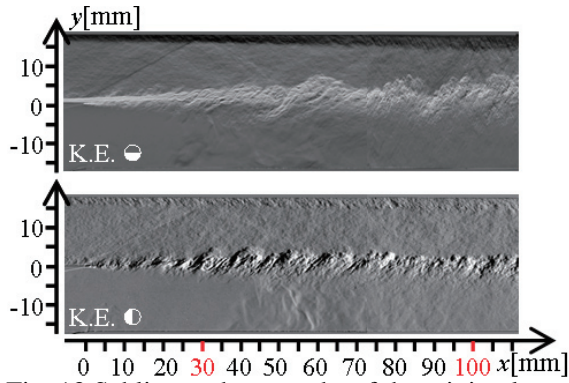


Fig. 13 Schlieren photographs of the mixing layer.

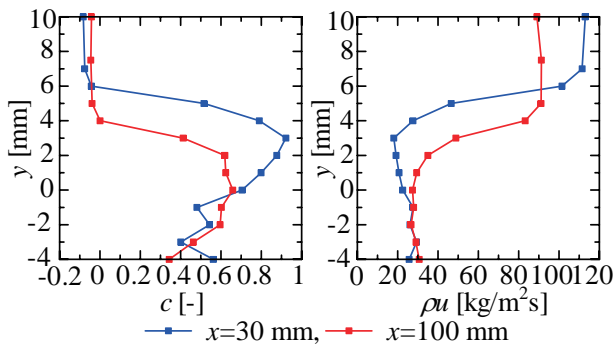


Fig. 14 Measurement results of helium concentration and mass flux in the mixing layer.

However, the results of the helium concentration were inconsistent, especially at the lower side of the mixing layer. Figure 15 plots the results of Fig. 14 on the calibration map of Fig. 10. In the lower side of the mixing layer, the power dissipation ratios of each hot wire were extremely small and the iso-concentration lines were close to each other as mentioned above. Therefore, the results could not be estimated correctly in this region. However, this can be improved if we select the proper material as the hot wire. Figure 16 plots the calibration results of the platinum wire whose diameter was 5 μm together with the calibration results of the two kinds of tungsten wires as shown in Fig. 8. As seen from Fig. 8, it is found that calibration results were changed by materials of hot wire. Therefore, by selecting proper wire materials, the intervals of the iso-concentration lines such as shown in Fig. 15 can be extended and the calibration map can be improved.

5. Conclusions

In the present study, we proposed simultaneous quantitation method of fluctuating mass flux and concentration. At first we resolve three problems in this method: calibration, spatial resolution and thermal lag of hot-wire response. Next, to demonstrate the usefulness of our method, we measured the air/helium mixing layer by using this method, and were able to obtain mass flux and helium concentration separately.

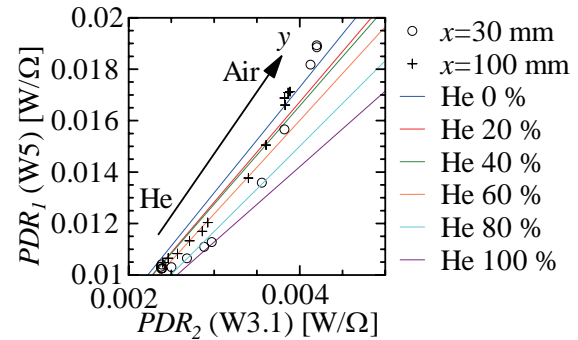
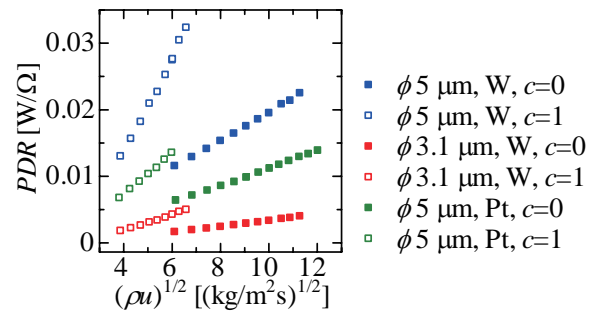


Fig. 15 Measurement results of the mixing layer plotted on the calibration map of Fig. 10.

Fig. 16 Calibration results of $\phi 5 \mu\text{m}$ and $\phi 3.1 \mu\text{m}$ tungsten wire and $\phi 5 \mu\text{m}$ platinum wire.

Acknowledgements

The present research was supported, in part, JSPS, Grant-in-Aid for Scientific Research, 1760694, 2005-2006.

References

- 1) O. C. Xillo, J. A. Schetz, W. F. Ng, and R. L. Simpson, "A Sampling Probe for Fluctuating Concentration Measurement in Supersonic Flow," M. S. thesis, Virginia Polytechnic Institute and State University, Blacksburg, 1998.
- 2) T. Arai, K. Mizobata, R. Minato, N. Tanatugu, Y. Mori, and T. Kudo, "Correlation between Fluctuations of Mass Flux and Hydrogen Concentration in Supersonic Mixing," AIAA-2005-323 AIAA/CIRA 13th International Space Planes and Hypersonics Systems and Technologies Conference, Capua, Italy, May 16-20, 2005.
- 3) J. L. Harion, M. Favre-Marinet, B. Camano, "An Improved Method for Measuring Velocity and Concentration by Thermo-Anemometry in Turbulent helium-air mixtures," Experiments in Fluid, Vol.22, pp.174-182, 1996.
- 4) G. R. Sarma, "Transfer function analysis of the constant voltage anemometer," Review of Scientific Instruments, Vol.69, Num.6, pp.2385-2391, 1998.

On the critical Reynolds number of the drag coefficient for a circular cylinder

T. Matsui

Dept. of Mech. Eng., Gifu University,

ABSTRACT

Drag coefficient of a circular cylinder in a uniform flow shows a steep fall when the Reynolds number increases from about 3.0×10^5 to about 3.8×10^5 in our experiments. At about $Re = 3.6 \times 10^5$, the drag coefficient curve is not continuous, but has a jump, and also a lift force actually acts on the cylinder. This phenomenon results from the sudden and asymmetric appearance of separation bubbles on both sides of the circular cylinder. The asymmetric formation of separation bubbles is the origin of lift. The Reynolds number, $Re = 3.6 \times 10^5$, is appropriately called the critical Reynolds number for the drag coefficient of a circular cylinder.

Key Words: critical Reynolds number, drag coefficient, lift coefficient, separation bubble

1. Introduction

The steep decrease at large Reynolds numbers in the drag coefficient curve will be described in connection with separation bubbles. A new definition of the critical Reynolds number will be proposed by referring to the experimental results by Ohkura and Okude⁽¹⁾.

2. The discontinuity of the drag coefficient and the generation of lift

The drag coefficient, C_D and the lift coefficient C_L , are shown in Fig. 1 against Reynolds number. We can see a discontinuity or a jump in the C_D curve at about $Re = 3.6 \times 10^5$ and at about the same Re number, we can see generation of lift, the value of which is not constant and it is shown that generation of lift⁽²⁾⁽³⁾ is a stochastic phenomenon.

3. The pressure distribution on the surface of a cylinder

The pressure distributions on a circular cylinder are shown at different Reynolds numbers, $Re = 2.0 \times 10^5$, 3.6×10^5 and 5.0×10^5 and for the frictionless flow, in Fig. 2.

The upward arrows in the figure show the separation of the boundary layer from the cylinder surface, and the downward arrows show the reattachment of the separated shear layer to the cylinder surface. Small steps in the curves show the

separation bubbles on the cylinder surface. The pressure distribution at $Re = 3.6 \times 10^5$ shows that the generation of a separation bubble leads to the delay of the separation of a turbulent boundary layer, which occurs about 130 degrees from the front stagnation point, resulting to the low drag.

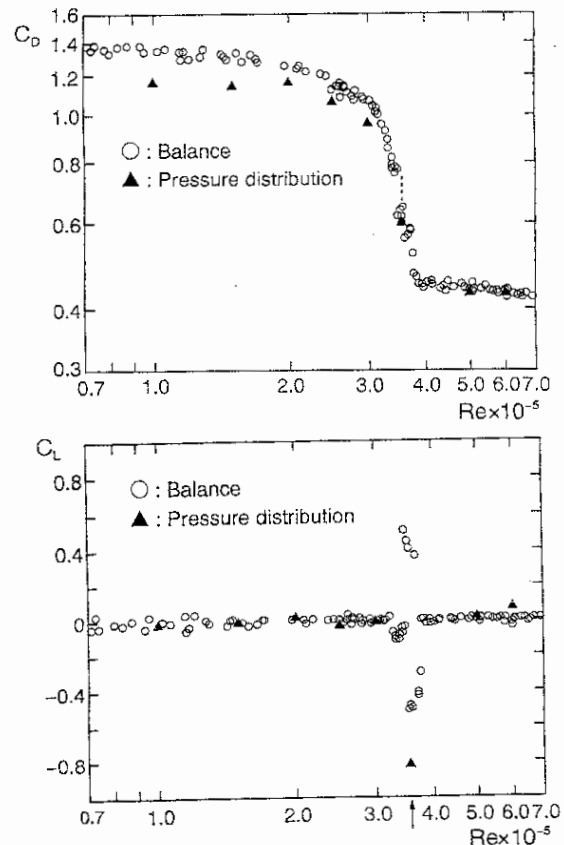


Fig. 1 Drag coefficient and lift coefficient

4. Stochastic appearance of separation bubbles

The surface pressure at two points, 90 and 270 degrees from the front stagnation point, was recorded when the uniform velocity was continuously increased from $Re = 3.2 \times 10^5$ to 3.9×10^5 during about 100 seconds. The measured results are shown in Fig.3. This is an example of forming process of a separation bubble.

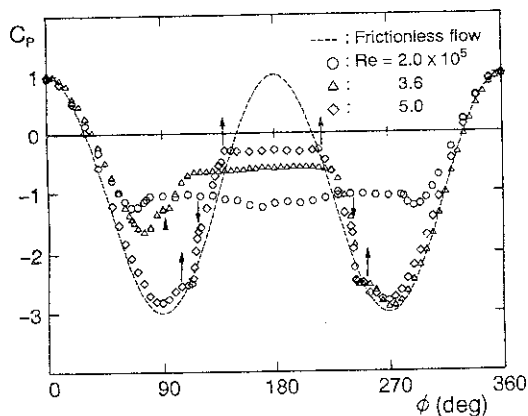


Fig. 2 Pressure distribution on the surface of a circular cylinder in a uniform flow

The pressure at 270 deg. suddenly dropped at about $Re = 3.6 \times 10^5$. It shows a jump in the drag coefficient curve and also generation of lift. This phenomenon shows the fact that the reattachment of separated shear layer to the cylinder surface, in other words, the generation of a separation bubble is a stochastic process. The duration of the pressure difference or the life time of the asymmetric separation bubbles is short. This fact is seen in Fig. 1, too.

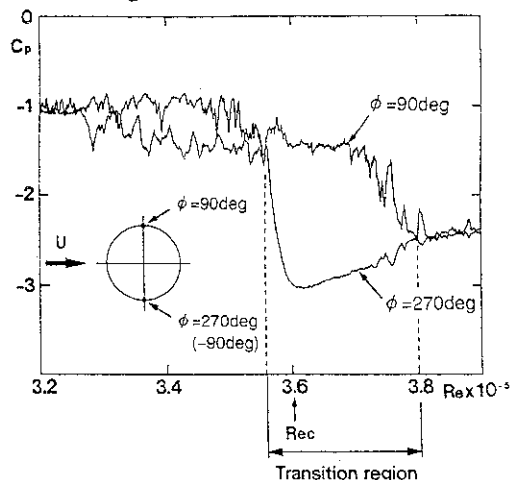


Fig. 3 Continuous change of the surface pressure at 90 and 270 degrees from the front stagnation

Therefore, the Reynolds number for the lowest pressure, $Re = 3.6 \times 10^5$, may be taken as the representative value of the transient, critical condition.

5. Summary

At about $Re = 3.6 \times 10^5$, separation bubbles were suddenly formed on a surface of a circular cylinder, as a result, drag was reduced and lift was generated. It is suggested that the Reynolds number is called the critical Reynolds number for drag coefficient of a circular cylinder in uniform flow.

References

1. Ohkura, N. and Okude, M.: Aero. and Space Sci. Japan **45** (1997), pp. 267-276.
2. Bearman, P.W.: J.F.M., **37**, (1969), pp. 577-585.
3. Kamiya, N., Suzuki, S., Nakamura, M. and Yoshinaga, T.: The 13th Congr. of Internat. Coun. Aero. Sci. (1980), pp. 417-428.

Numerical Simulations of Flow past a 2-D Airfoil at a Low Reynolds Number

T. Ikeda, T. Kurotaki, T. Sumi, and S. Takagi

Japan Aerospace Exploration Agency (JAXA)

ABSTRACT

Karman-vortex shedding induced by wake instability behind a 2-D airfoil is of interest at relatively low Reynolds numbers, to understand how a vortex street develops in the wake region, and also how an aeolian tone is generated therefrom; this is supposed to show a different flow mechanism from a high-Reynolds number flow that exhibits more complicated viscous-flow phenomena. In this study, we performed numerical simulations of a 2-D laminar flow past an NACA0012 airfoil. The computation was run on the simulation code being developed to predict an aero-acoustic problems by using a highly accurate numerical method. For the verification of our code, the results are compared with the experimental data obtained in a similar flow configuration and also with an available numerical study. The detailed flow visualization is presented to understand the mechanism of the wake instability that results in vortex shedding.

Key Words: 2-D airfoil, wake instability, tonal noise

1. Introduction

We, Aerodynamics Research Group in JAXA, are now developing a computational fluid dynamics (CFD) code to simulate aeroacoustic phenomena at high accuracy. The code is designed primarily to perform a compressible large eddy simulation (LES) by combining high-order numerical schemes and an inverse filtering approach. As a prior study using this code¹, a high-Reynolds number flow past a two-dimensional airfoil was solved by successfully reproducing the boundary-layer transition after the occurrence of Tollmien-Schlichting instability waves. The study also captured the evidence of trailing-edge (TE) noise generation observed both in the sound pressure spectra near TE and the visualization of instantaneous pressure fluctuation.

However, it is also known that a tonal noise occurs in similar flow configurations at rather lower Reynolds numbers. In this case, a Karman vortex street develops in a laminar wake region, without the occurrence of direct emission of vortices from foil surface. Also, the difference should arise how the generated fluctuation of sound wave propagates in the boundary layer.

Our objective of this study is twofold. One is to understand the mechanism of vortex shedding and aeolian-tone generation, presumably induced by wake instability, at a low Reynolds number. The spatial and temporal dependence of velocity fluctuations are examined within both boundary layer and wake. Secondly, we would demonstrate the validation of our CFD code as an aeroacoustic solver: the detailed data of flow and generated sound levels are compared with other numerical and experimental studies^{2,3}.

2. Numerical Procedure

The description of numerical methodology is detailed in Ref. 1, including the derivation of modeling sub-grid scales (SGS) for LES. Since a laminar 2-D flow is expected at a low Reynolds number, we do not apply any SGS models and only 2-D components (streamwise and wall-normal directions) of flow variables are solved, although the code can treat general 3-D problems.

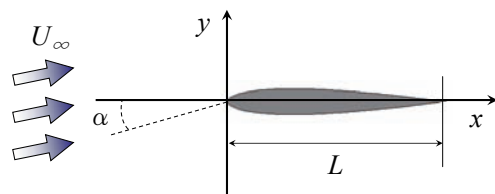


Fig. 1 Flow configuration

A schematic view of geometrical configurations is shown in Fig. 1. NACA0012 airfoil of the chord length L is aligned to the x -axis, so that the origin of coordinates comes to the leading edge. The Reynolds number based on L and the inflow velocity U_∞ is 7500, and the inflow Mach number is 0.1. The angle of attack α varies from 0.0 to 5.0[deg.] in this study. Flow field is discretized using C-grid topology with an interface condition applied where two boundaries collapse from TE toward downstream in the wake region. The grid dimension of the results shown here is $900 \times 160 = 144,000$, which is relatively small to be used in a direct simulation of aeroacoustics; for instance, nearly 2 million grid nodes were used at

$Re=5000$ in Ref. 2. However, the grid convergence is confirmed so that near-field sound pressure levels would not be affected by insufficient resolution.

3. Wake Instability

First, the instantaneous streamwise velocity (or u -velocity) contours are shown, from the middle of the airfoil to $2L$ downstream from TE, and compared for three different angles of attack, in Fig. 2. With no incident angle, almost no unsteady motion can be recognized just behind the airfoil; the vortex shedding gradually develops in the wake, and the velocity fluctuation takes its maximum at about $x=2L$, one chord length down from TE. Fig. 3 shows the power spectrum density (PSD) of wall-normal velocity (or v -velocity) at the location. The primary shedding frequency obtained for $\alpha=0.0[\text{deg.}]$ is 2.2, while those reported in Refs. 2 and 3 are close to ours, 1.8 and 2.5, respectively. As α increases, the location of the maximum u -fluctuation shifts toward upstream. At $\alpha=5.0[\text{deg.}]$, a considerable recirculation zone forms on the suction side near TE; vortices are directly generated therefrom, which resembles the vortex shedding of a bluff body.

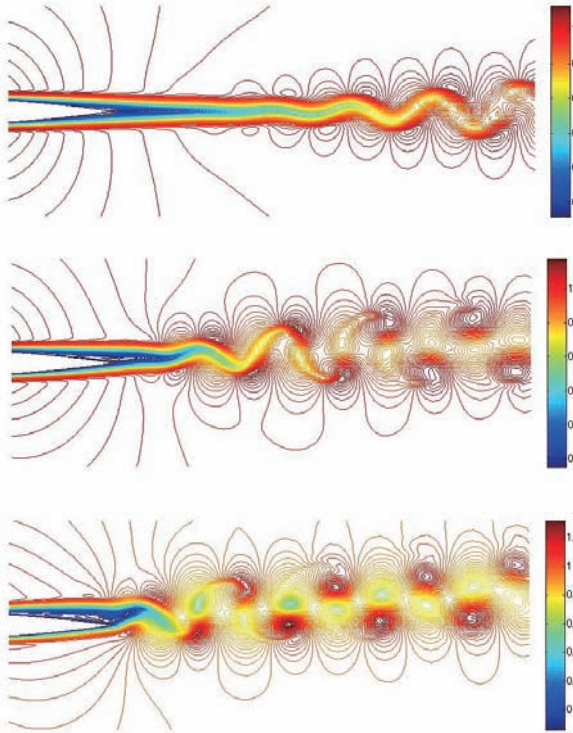


Fig. 2 The development of Karman vortex street: (top) $\alpha=0.0$; (middle) $\alpha=2.5$; (bottom) $\alpha=5.0[\text{deg.}]$.

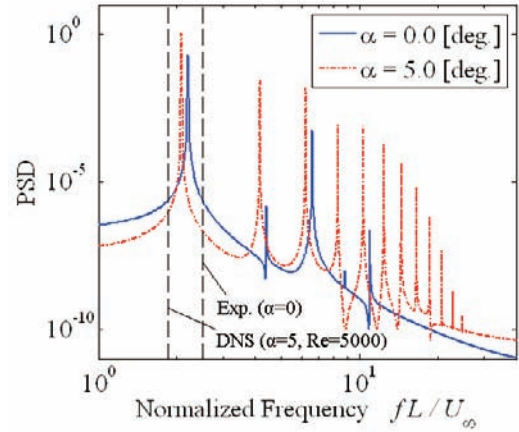


Fig. 3 PSD of v -velocity at $x=2L$

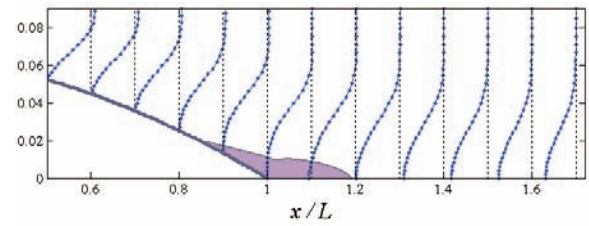


Fig. 4 Streamwise velocity profiles near TE ($\alpha=0.0$). Filled region indicates reverse flow.

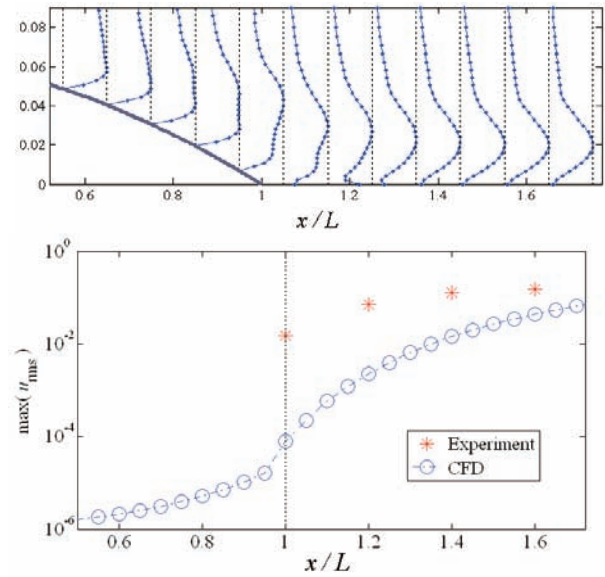


Fig. 5 RMS u -fluctuation ($\alpha=0.0$): (top) normalized profiles; (bottom) growth of maxima.

By examining the time-averaged velocity field for $\alpha=0.0[\text{deg.}]$ in Fig. 4, a bell-shaped profile is obtained in the wake. Clearly, the self-excited vortex shedding is attributed to the inflexion-point instability. However, we also see a reverse flow region around TE. It is possible that the growth of fluctuation, after the boundary layer separates, could be increased abruptly by the presence of reverse flow, as seen in Fig. 5. In the same diagram, the

experimental data of Ref. 3 are shown. The discrepancy may be explained by the wind-tunnel inflow fluctuation, as well as measurement errors. Also, the experimental peak location of maximum is rather close to TE than our numerical result; inflow fluctuation may accelerate the development of the Karman vortex. However, the overall maximum of u -fluctuation agrees well in both cases, as their maxima collapse toward downstream.

4. Tonal Noise Generation

Even though vortices are not fully developed near TE, as portrayed in Fig. 2, still an aeolian tone is generated by the interaction between the foil-surface and vortex shedding, unlike a bluff body case. Fig. 6 shows the generation and propagation of sound pressure up to about $10L$ from the airfoil. Our simulation code clearly reproduces fairly weak pressure fluctuation. Fig. 7 is the close views of a sound source. As shown in the figure of $\alpha=0.0$ [deg.], the undisturbed pressure oscillation indicates that the pressure fluctuations in the wake do not necessarily represent the presence of vortices traveling with them, since the vortices form rather downstream.

The magnitude of sound wave at $1L$ vertically away from TE is of the order of as low as 10^{-7} for $\alpha=0.0$, but still consistent with the other two cases, as well as the results in Ref. 2: dipole sound is generated near TE with the frequency of vortex shedding, and decays with $r^{-1/2}$ dependence, as shown in Fig. 8 by dashed line. As also seen, the sound pressure level strongly depends on the angle of attack, α . The increase of α enlarges the cross-sectional area for the inflow, which practically increase the Reynolds number. However, also with the increase of α , the separation bubble at TE becomes more distinguishable, which energizes vortex shedding, and eventually sound generation, too.

Fig. 8 also shows sound pressure levels at $\alpha=5.0$ [deg.] in Ref. 2. The reference cases were run at a different Mach number, 0.2; the plotted data were modified for $M=0.1$ by the factor $M^{2.5}$, Mach number dependence of 2-D dipole sound. The remaining discrepancy is due to the Reynolds number difference. We also tested the case of $Re=5000$ and $\alpha=5.0$ [deg.] on our code and obtained results well-agreed with Ref. 2; they are not shown here.

As for the velocity fluctuation due to the sound wave, Fig. 5 shows the positive growth of u -fluctuation all the way from the middle of the chord. However, the growth rate is altered abruptly across TE, which implies the different mechanism to amplify velocity fluctuations. To examine this, u -velocity is monitored in several locations in the boundary layer, as shown in Fig. 9. The sinusoidal temporal variations at all the locations do not exhibit a significant phase difference. In addition, the

instantaneous u -fluctuation contours do not show any discernible phase distribution in the streamwise direction, although the amplitude of fluctuation does show the exponential dependence as was shown in Fig. 5. This observation suggests that the fluctuations in the boundary layer represent a linear disturbance of acoustic wave decaying toward the leading edge, not the unsteady motions transmitted from an upstream region. Therefore, at this low Reynolds number, acoustic disturbance does not affect the laminar boundary layer on airfoil surface.

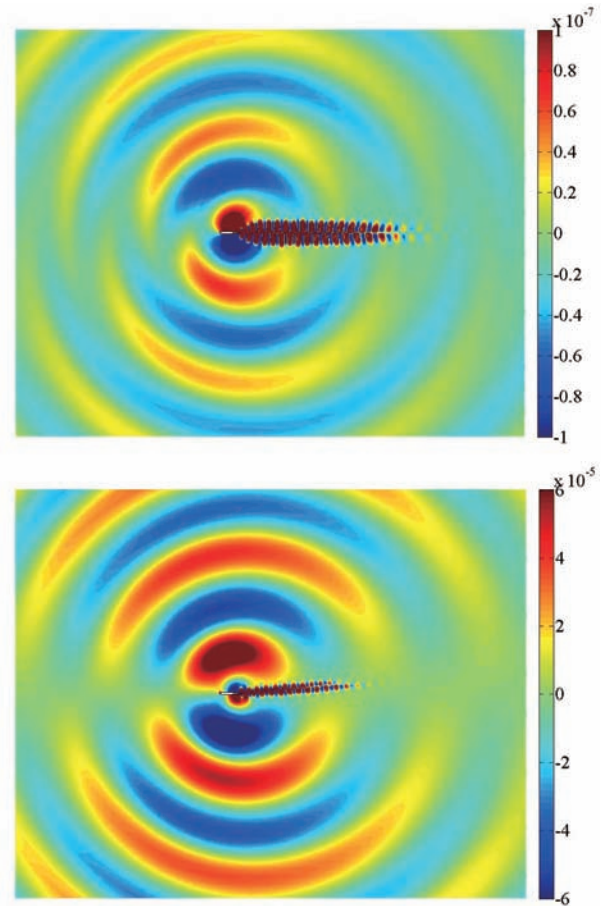


Fig. 6 Instantaneous pressure fluctuation: (top) $\alpha=0.0$; (bottom) $\alpha=5.0$

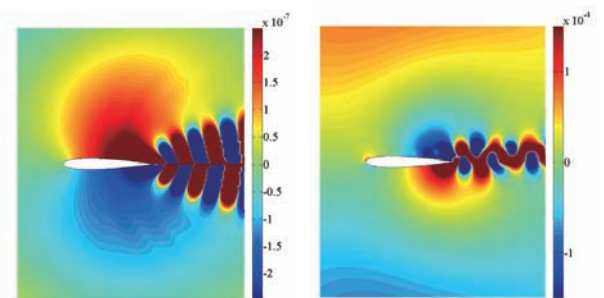


Fig. 7 Close views of instantaneous pressure fluctuation: (left) $\alpha=0.0$; (right) $\alpha=5.0$

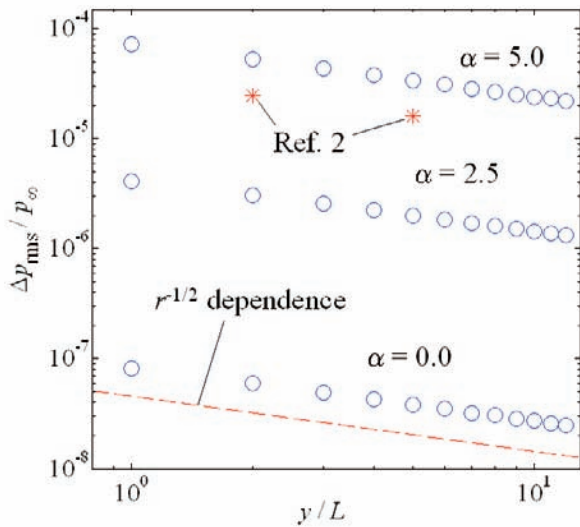


Fig. 8 RMS pressure fluctuations decaying on the distance from TE: O, current simulations; *, Ref. 2 ($Re=5000$, $\alpha=5.0$)

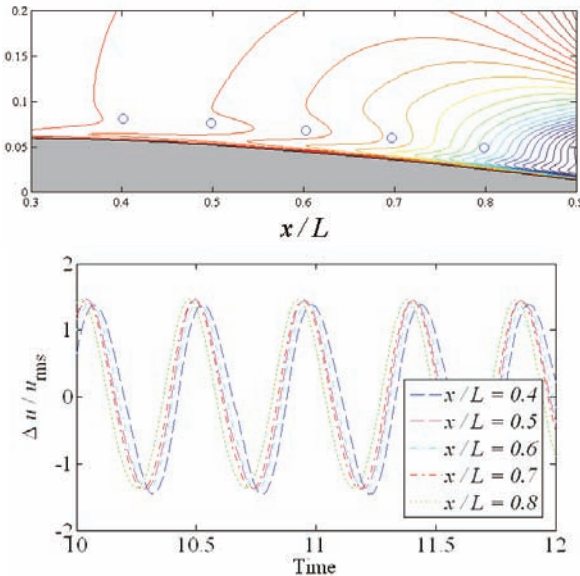


Fig. 9 Phase difference in boundary layer: (top) instantaneous u -fluctuation contours and monitoring locations denoted by O; (bottom) time history of u -fluctuation normalized by its RMS.

5. Summary

The two dimensional wake instability of flow past NACA0012 at $Re=7500$ was successfully reproduced by our simulation code that is being developed to solve aero-acoustic problems. A quantitative examination of velocity distributions and fluctuations, as well as shedding frequencies achieved a sufficient agreement with other studies. Visualizations also depict the qualitative mechanism of vortex-shedding development.

Aeolian tones, portrayed well in the instantaneous pressure fluctuation fields, also provide quantitatively accurate behavior. Unlike bluff body flows, pressure fluctuation moving downstream in the wake is not directly associated with vortices, although the frequencies of both pressure fluctuation and vortex shedding are consistent. Nevertheless, a dipole sound is produced at the vicinity of TE through the interaction of the airfoil surface and the Karman vortex that develops away from the foil.

On the boundary layer receptivity, we observed no evidence that the sound wave affects the boundary layer. The linear wave is only transmitted toward upstream from TE, and decays very quickly. The Karman vortex develops in self-exciting mechanism induced by the instability of wake velocity profiles, not affected by acoustic disturbances.

References

- 1) T. Kurotaki, T. Sumi, and T. Atobe: Numerical simulation around airfoil with high resolution in high Reynolds numbers, AIAA Paper 2007-720
- 2) T. Irie, N. Hatakeyama, and O. Inoue: Direct numerical simulation of aerodynamic noise around an airfoil, *Proceedings of 8th Japan-Russia CFD Symposium*, (2003), P.14-15
- 3) S. Takagi, T. Kamono, and S. Rikitake: Wake instability behind NACA0012 at low Reynolds numbers, *Proceedings of 6th International Symposium on Advanced Fluid Information* (2006), P.91-92

The Velocity Distribution Around Aerofoil for Wing in Ground Effect

S. Kikuchi*, Y. Kozato*, S. Imao*, and H. Mitsui*

* Dept. of Mechanical and Systems Eng., Gifu University

ABSTRACT

Flow characteristics around aerofoil for wing in ground effect are studied experimentally in a wind tunnel. Lift and drag forces were measured directly by 3-component force transducer and velocity distributions around the aerofoil were obtained by PIV. Experimental results show that lift and drag forces were consistent with the data obtained earlier qualitatively. With decreasing a ground clearance, the stagnation point moves backward and the effective angle of attack increases. For this reason, the flow rate between the aerofoil and the ground decreases, and the flow between the aerofoil and the ground is decelerated, and the pressure on the undersurface of the aerofoil increases. This is one of the causes of the wing in ground effect.

Key Words: Wing in ground effect, Effective angle of attack, Stagnation point

1. Introduction

When a wing approaches the ground or a water surface, its lift-drag ratio increases greatly. This phenomenon is called “wing in ground effect (WIG)”⁽¹⁾. The transportation system using WIG was proposed by Kohama et al.⁽²⁾ This WIG vehicle is referred to as “Aero-Train,” and it is developed by them.

The wing in ground effect is the effect of pressure rise under the wing and weakening of the wing tip vortices. Sometimes, it is said that this pressure rise is caused by ram pressure (compression of the air by dynamic pressure). However, at low speed, the ground effect can be found without ram pressure. Therefore, the pressure rise seemed not to be attributed to ram pressure. In this paper, to confirm why pressure increases under the wing, the flow around the aerofoil was investigated experimentally.

2. Experimental Procedure

Figure 1 shows the experimental setup. The airfoil profile was NACA6412 modified (Fig.2) that was the same profile of the Aero-Train model of Kohama et al.. The size of the wing was 152mm chord, 295mm span. A lift and drag of the wing was measured directly by a 3-component force transducer (Nissho Electric Works Co., Ltd., LMC-3501-50N). The velocity distribution around the wing was measured by PIV system. (This system belongs to Division of Instrumental Analysis, Life Science Research Center, Gifu Univ.) To make PIV measurement under the wing possible, the ground plate was made by a Plexiglas flat plate. Figure 3 shows the coordinate system used here and the definition of height of the aerofoil h , which is the ground clearance. The free-stream velocity U was set at 20m/s, and the Reynolds number was 2.0×10^5 .

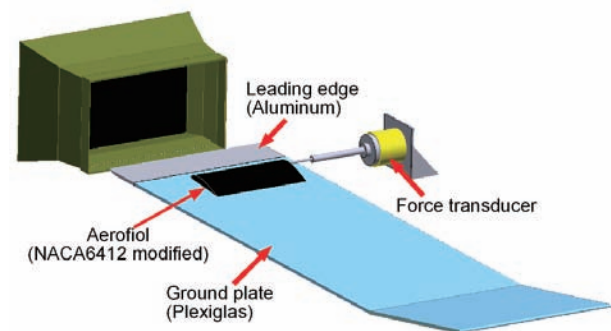


Fig.1 Experimental apparatus

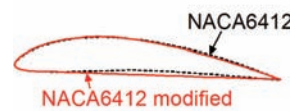


Fig.2 Aerofoil profile

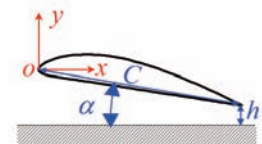


Fig.3 Coordinate system

3. Results and Discussion

Figure 4 shows lift, drag, and lift-drag ratio against the ground clearance. The lift increases and the drag decreases as the wing approaches the ground. As a result, the lift-drag ratio increases markedly. These results are consistent with previous data qualitatively, and it was confirmed that the ground effect occurred with this equipment.

Figure 5 shows the velocity distribution around the wing. The data was measured by dividing into four areas, then combined numerically. The data shown in Fig.5 is the time mean velocity averaged over 50 data. As the wing approaches the ground, the velocity under the wing decreases, and the velocity above the wing rises. Paying attention to the velocity near the leading edge, it seems that the stagnation point moves downward. In order to investigate in more detail, the velocity distribution near the leading edge was measured. The result is shown in Fig.6. The direction of velocity vectors near the leading edge

becomes upward with decreasing the ground clearance, which means the effective angle of attack increases. The dividing streamline, which is a line that separates the flow above the wing and the flow under the wing, was calculated from these data. These lines are shown in Fig.7 as a stream line that passes a point whose vorticity is zero near the leading edge. When the wing approaches the ground, the stagnation point moves downward and the effective angle of attack increase. The shift of the stagnation point and the increase of effective angle of attack lead to the reduction of the flow rate between the wing and the ground. This reduction in flow rate means the reduction of velocity and pressure rise under the wing. Therefore, it is found that the pressure rise is caused by the velocity reduction and it is not the ram pressure.

References

- 1) H.Tomaru, Y.Kohama: *J. Japan Soc. of Fluid Mech.*, 10, (1991), pp.47-60,(in Japanese).
- 2) S.Kikuchi, F.Ohta, T.Kato, T.Ishikawa, Y. Kohama: *J. Fluid Sci. and Tech.*, 2(1), (2007), pp.226-237.

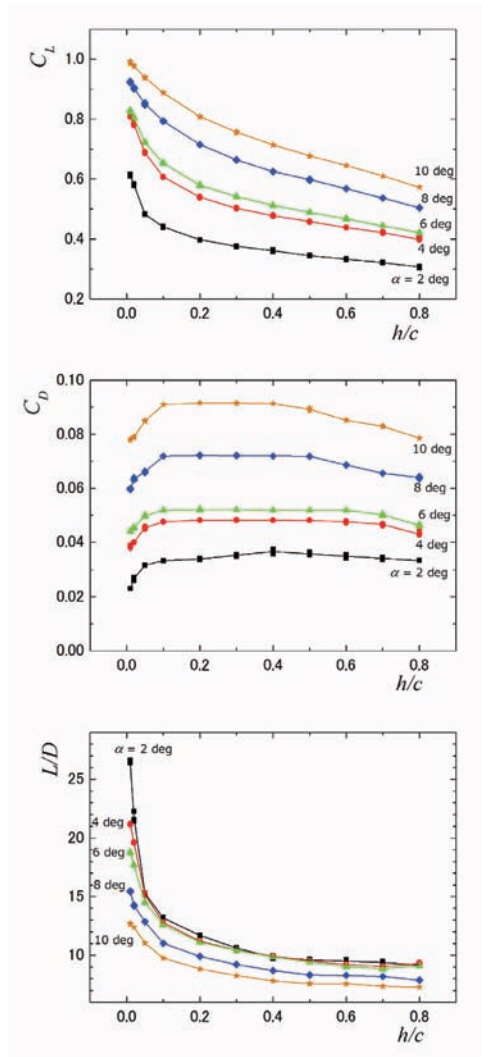


Fig. 4 Aerodynamic force

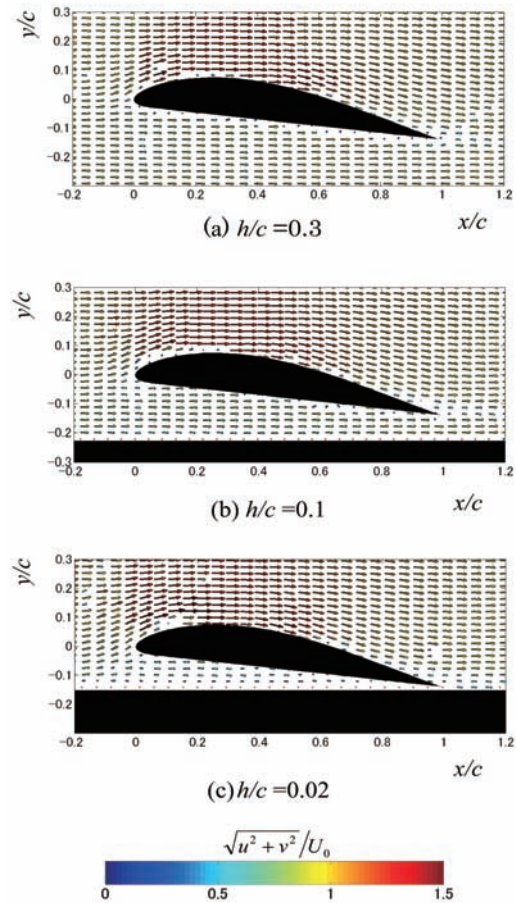


Fig.5 Velocity distribution around the wing ($\alpha=8\text{deg}$)

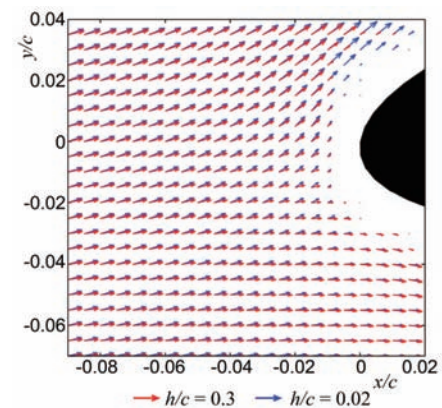


Fig.6 Velocity near the leading edge ($\alpha=8\text{deg}$)

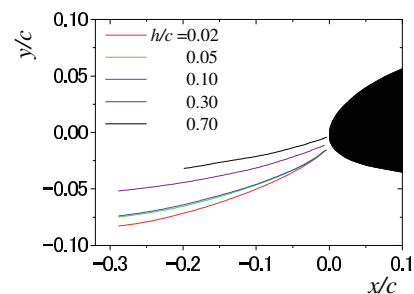


Fig.7 Dividing streamline ($\alpha=8\text{deg}$)

Experiments at the Sunrise-Beach Research Facility of the Aerodynamic Characteristics on Ground Effects of Aerofoils with a secondary aerofoil

Y. Takahashi^{*}, M. Kikuchi^{**}, K. Hirano^{**}, T. Yuge^{**}, T. Moriya^{***}, and Y. Kohama^{****}

^{*} Department of Mechanical Engineering, Miyakonojo National College of Technology,
^{**} Mechanical System Engineering, University of Miyazaki,
^{***} Graduate Student, Mechanical System Engineering, University of Miyazaki,
^{****} Institute of Fluid Science, Tohoku University

ABSTRACT

Investigation of a new high-speed zero-emission transportation “Aerotrain” is proceeded mainly in Tohoku University and Miyazaki University. Since the aerotrain utilizes the ground effect, researches of the aerofoil section which can harnesses the ground effect effectively are important. The aerotrain moves along U-shaped guide way which has a ground and side walls, so it has many viscous interference elements. We analyze the flow through a primary and secondary aerofoils, to prevent the boundary layer separation for the improvement of the aerodynamic characteristics at low speed and near the ground. A small secondary aerofoil is equipped above the trailing edge to increase lift at takeoff and landing. We find out the most suitable location of secondary aerofoil by the boundary layer approximation analysis, and experiment using towing wind tunnel at the Sunrise-Beach Research Facility in Miyazaki.

Key Words: Ground Effect, Secondary Aerofoil, Towing Wind Tunnel, Boundary Layer Approximation

1. Introduction

Recently, global warming caused mainly by greenhouse gas emissions, such as carbon dioxide, has become a more serious problem. The level of greenhouse gas emissions in transportation division is not small, therefore it is necessary to improve the energy efficiency to reduce the emissions of these gases and the utilization of natural energy for a power source.

On the basis of this background, an investigation on a new type of high-speed zero-emission mass transportation, the “Aerotrain” has been carried out mainly in Tohoku University and University of Miyazaki. The aerotrain with several short aerofoils is an aerodynamically levitated vehicle, which harnesses the energy of the sun and the wind around the guide way. The aerotrain runs at high energy efficiency, using the ground effect, which occurs when an aerofoil moves near the ground. Because the aerotrain utilizes the ground effect, researches on the aerofoil section, which can harness the ground effect effectively, is important. The aerotrain cruises along U-shaped guide way, which has a ground and side walls, so it has many viscous interference elements. In an analysis of ground effects on the aerodynamic characteristics of aerofoils, the boundary layers on the aerofoil surface must be considered.

We analyze the flow through primary and secondary aerofoils, to prevent the boundary layer separation for the improvement of the aerodynamic characteristics at low speed and near the ground. A

small secondary aerofoil is equipped above the trailing edge to increase lift at takeoff and landing. We find out the most suitable location of secondary aerofoil by the boundary layer approximation analysis, and experiment using towing wind tunnel. We verify the effect of secondary aerofoil by experiment, and verify the accuracy of the analysis by comparing with experimental results, and try to find the most suitable aerofoil section for Aerotrain

2. Analysis and Experimental Procedure

The ground effect on the aerodynamic characteristics of the aerofoils was analyzed using the following procedure. First, the vortex method is used to calculate the velocity distribution on the outside of the boundary layer. Next, the boundary layer approximation is used to calculate the boundary layer thickness. Then, the displacement thickness of the boundary layer is added to the aerofoil thickness. Finally, the vortex method is used to calculate the velocity distribution on the modified aerofoil profile. This procedure is repeated. When the solution converges, we estimate the aerodynamic characteristics of aerofoils. The computational geometry and parameters are shown in Fig.1.

The measurement of pressure distribution on aerofoil surfaces was carried using a towing wind tunnel. The equipment has 500m long test section, 1000m long accelerating and 500m long decelerating section. The experiment was done only in the wind

tunnel with the 500m full length. The cross section of the wind tunnel is shown in Fig.2. Aerofoil characteristics were measured by towing a test aerofoil in 50km/h with the car which is shown in Fig.3. An acrylic fiber board with 1.55m length, 0.9m height, 6mm thickness is equipped by the aerofoil tips to secure a two dimensional of the flow. The chord length and the width of the primary aerofoil is 1000mm and 1820 mm the secondary aerofoil is 300mm and 1810mm. The primary aerofoil has 37 pressure measurement holes with 1.2mm caliber along the direction of the moving at the centre of the aerofoil width, and the secondary aerofoil has 24 holes with 1.0mm. Both aerofoils adjust an angle of attack with the lever at the fixation axis of the aerofoils, and adjust the altitude with the elevator at the fixation axis. The test aerofoil section is NACA4412 for both aerofoils. The pressure on aerofoil surfaces is measured using the digital sensor array (scanivalve DSA3217). As the experimental parameter of the primary and secondary aerofoils, an angle of attack α and α_s , an altitude of the trailing edge h and h_s , was varied.

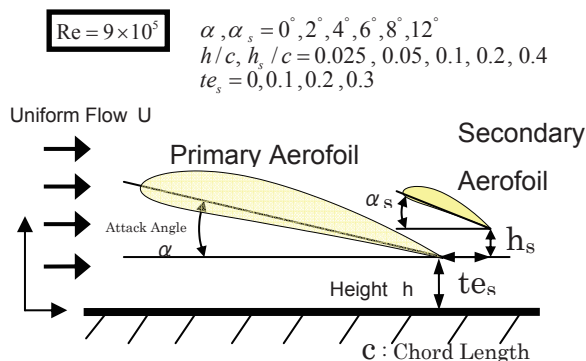


Fig.1 Computational geometry and parameters

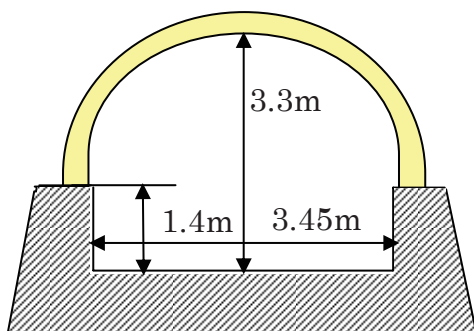


Fig.2 Cross section of wind tunnel

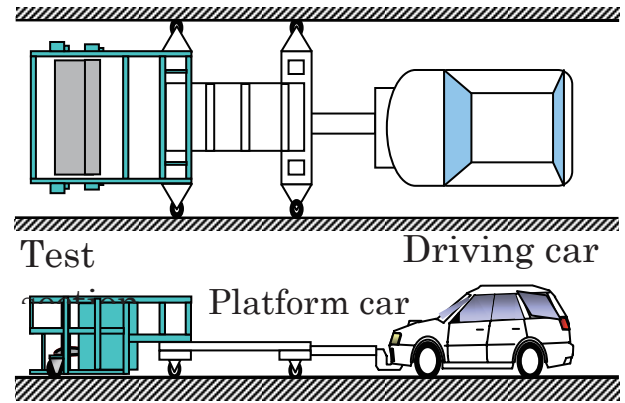


Fig.3 Experimental Device

3. Results and Discussion

The example of the computed pressure distribution on aerofoil is shown in Fig.4. The pressure coefficient for the primary aerofoil surface and on the secondary aerofoil are shown this figure. The pressure of the secondary aerofoil decreases suddenly, near the leading edge of lower surface. And, the pressure on the primary aerofoil is dipped near the leading edge of the secondary aerofoil. The reason for this, the flow through between primary and secondary aerofoils was accelerated like a venturi tube.

The relation between total lift coefficient and height of secondary aerofoil h_s is shown in Fig.5. Total lift coefficient is defined the sum of c_l for primary and secondary aerofoils. In this figure, horizontal lines indicate for the case without secondary aerofoil, curved line with secondary aerofoil. Lift coefficient is improved above each horizontal line. That is, the improved range is larger than about 0.15 of h_s in this computational parameter.

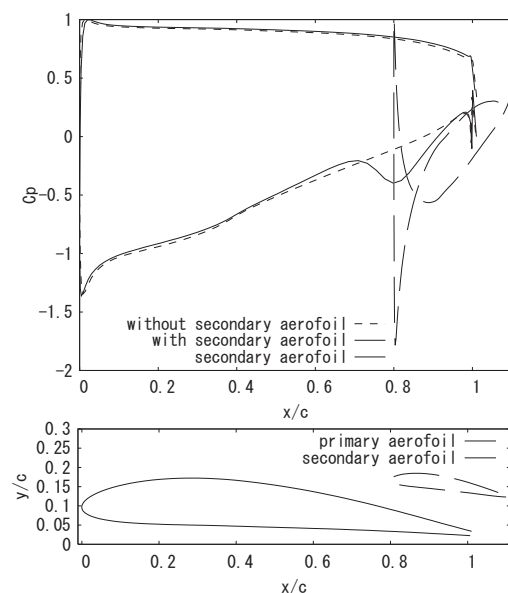


Fig.4 Pressure distributions of aerofoils

The relation between separation point and height of secondary aerofoil is shown in Fig.6. The vertical

lines indicate for the case without secondary aerofoil. Separation point is improved on the right side of vertical lines. That is, the improved range is 0.07 to 0.25 of h_s . The effect of attack angle on secondary aerofoil is shown in Fig.7.

The angle of attack on primary aerofoil is 4 degrees and 8 degrees. Just like previous Fig.4, lift coefficient is improved above horizontal lines. That is, in the case of $\alpha = 4^\circ$, lift coefficient is improved at almost range of secondary α_s . However, in the case of $\alpha = 8^\circ$, the improvement is not found below 8 degrees of α_s .

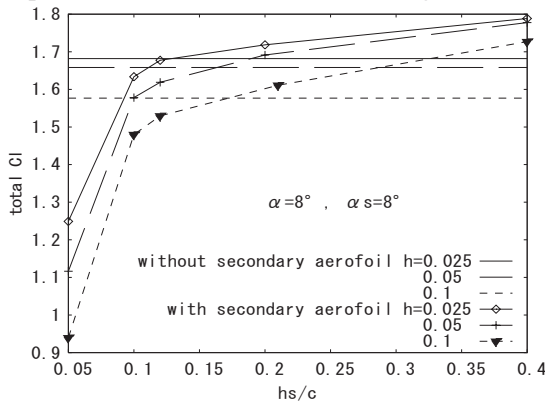


Fig.5 Total lift coefficient

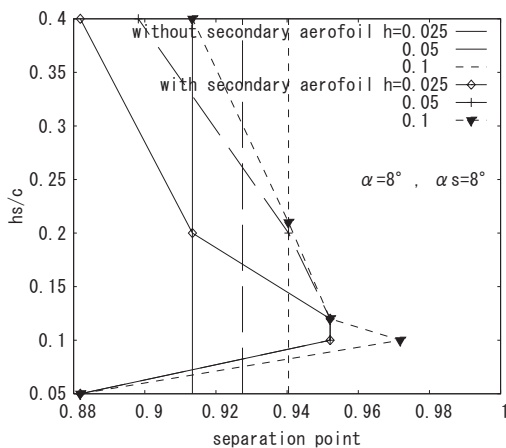
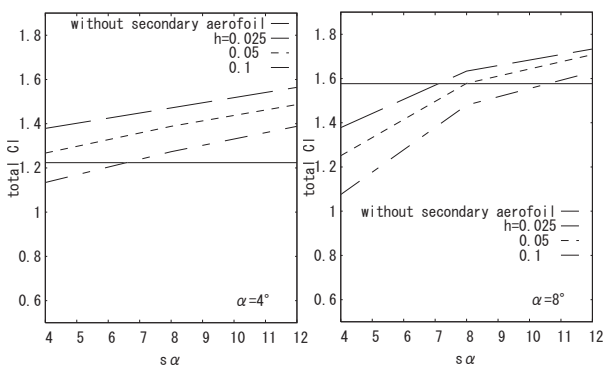


Fig.6 Separation point (primary aerofoil)


 Fig.7 Total lift coefficient ($h=0.1$)

The example of the experimental pressure coefficients on aerofoil using the towing wind tunnel

is shown in Fig.8. The computational results and experimental results, on the whole, indicate the same tendency. The example of the pressure distribution on primary and secondary aerofoils by attack angle of secondary aerofoil is shown in Fig.9 and Fig.10. This tendency became stronger, when the attack angle of secondary aerofoil α_s to smaller.

Comparison between the lift coefficient of primary aerofoil and the lift coefficient of single aerofoil is shown in Fig.11. In the case of h_s less than 0.2, the lift coefficient of the primary aerofoil is improved than case of the single aerofoil. The lift coefficient is improved at lower h_s and α_s . On the other hand, the lift coefficient of primary and secondary aerofoil is shown in Fig.12. Oppositely, the total lift coefficient of primary aerofoil and secondary aerofoil is improved at higher h_s and α_s .

4. Summary

We tried to improve ground effects on aerodynamics of aerofoils using secondary aerofoil. We examined the effect of the secondary aerofoil by analysis using vortex method with boundary layer approximation and experiment using towing wind tunnel at the Sunrise-Beach Research Facility in Miyazaki. We examined the improve range for an arrangement of the secondary aerofoil.

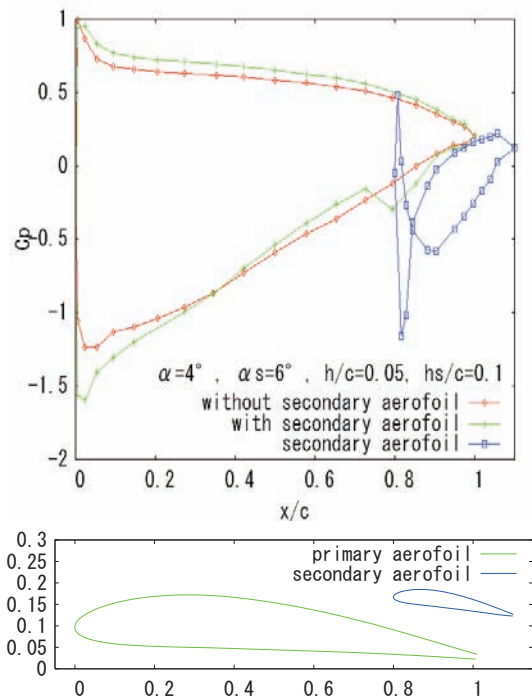


Fig.8 Pressure distribution of aerofoils

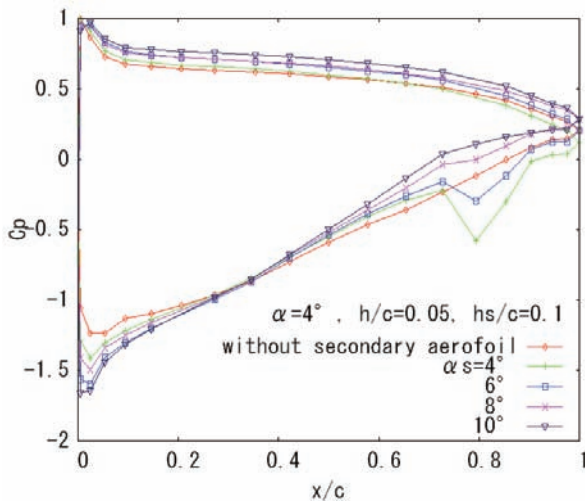


Fig.9 Pressure distribution of primary aerofoil

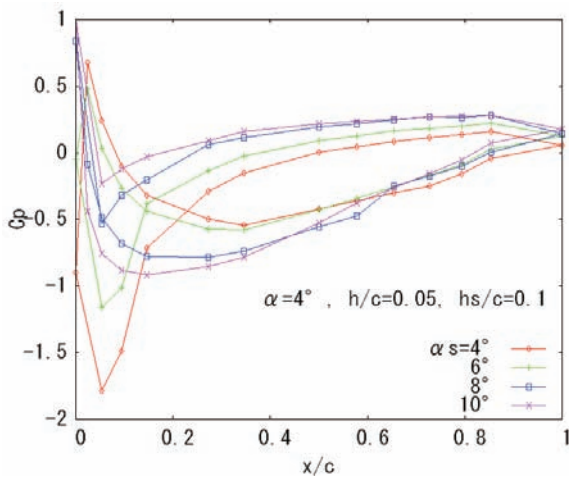
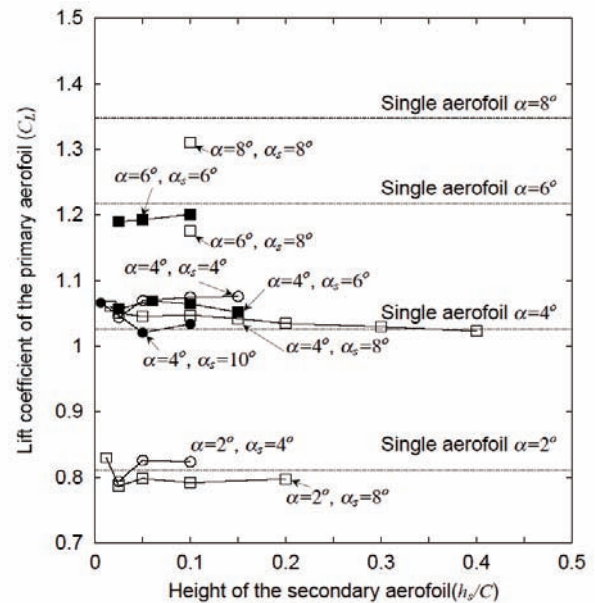
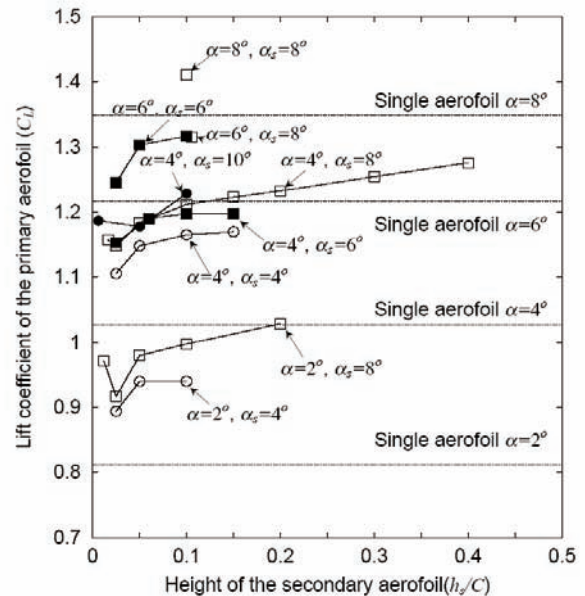


Fig.10 Pressure distribution of secondary aerofoil

References

- 1) Kikuchi, M. et al., Measurement of Aerofoil Characteristics by Method of Towing Model, *Transactions of the Japan Society of Mechanical Engineers, Series B*, Vol. 68, No.676 (2002), pp. 150-157.
- 2) Kikuchi, M. et al., Effect of Camber Form on Aerofoil Characteristics by Towing Wind Tunnel, *Proceedings of the 57th Kyushu Branch Regular Meeting of the Japan Society of Mechanical Engineers*, No.048-1 (2004-3), pp. 269-270.
- 3) Takahashi, Y. et al., An Analysis of Ground Effects on Aerodynamic Characteristics of Aerofoils using Boundary Layer Approximation, *Proceedings of the 57th Kyushu Branch Regular Meeting of the Japan Society of Mechanical Engineers*, No.048-1 (2004-3), pp. 267-268.
- 4) Takahashi, Y. et al., An Analysis of Ground Effects on Aerodynamic Characteristics of Aerofoils Using Boundary Layer Approximation, *Transactions of the Japan Society of Mechanical Engineers, Series B*, Vol. 71, No.705 (2005), pp. 122-129.

Fig.11 Lift coefficient of primary aerofoil ($t_{es}/c=0.2$)Fig.11 Lift coefficient of primary and secondary aerofoil ($t_{es}/c=0.2$)

- 5) Takahashi, Y. et al., An Analysis and Experiment of Ground Effects on Aerodynamic Characteristics of Aerofoils with a Secondary Aerofoil, *Proceedings of the 6th KSME-JSME Thermal & Fluids Engineering Conference*, (2005), Session JE.05.
- 6) Lewis, R.I., *Vortex Element Methods for Fluid Dynamic Analysis of Engineering System*, (1991), Cambridge University Press.
- 7) <http://www.fluidlab.naoe.t.u-tokyo.ac.jp/~yama/p/rog>
- 8) Çebeci, T. and Bradshaw, P., *Momentum Transfer in Boundary Layer*, (1977), McGraw-Hill Book Company.

Friction Wear Properties between Partially Polished CVD Diamond and Structural Steel

H. Miki, N. Yoshida, T. Abe, T. Takeno and T. Takagi
Institute of Fluid Science, Tohoku University

ABSTRACT

Low friction properties were achieved between partially polished diamond film and structural steel. Diamond films were deposited onto TiC substrates by microwave chemical vapor deposition (MWCVD) using gas mixture of CH₄ and H₂. Deposited diamond film was polished with each other up to surface roughness $R_a=0.25\text{ }\mu\text{m}$. We proposed newly developed pin-on-disk measuring device in order to obtain stable friction coefficient. Friction and wear tests were carried out in the nitrogen atmosphere, the ambient and dry air. In the case of D2, we confirmed the very low and stable friction coefficient $\mu=0.08$ without any lubricants in the ambient atmosphere.

KEYWORDS: CVD, polycrystalline diamonds, low friction, wear

Since the first breakthrough in the chemical vapor deposition diamond films, many research works have been done about their excellent properties such as high hardness, low friction, good thermal conductivity and wide band gap structure¹⁾. From the viewpoint of industrial applications, the artificial diamond is widely used for the cutting tools. However, the major problems for their practical application lie in the limitation of the substrates and their rather high hardness.

The former problem is being solved by particular technique such as the treatment of the substrate materials²⁾ and the fabrication of the machinable substrates, Ti₃SiC₂³⁾. In order to overcome the latter problem, we developed easily polishable diamond films. The investigated diamond films are categorized as a ballas diamond which was first discovered by Fischer⁴⁾. Related to ballas type diamond films, many research works have already been done⁵⁻⁷⁾. Ballas diamond consists of small polycrystal-

line diamonds connected with each other through amorphous carbon structure, which makes easy to polish diamond surface.

We used the partly polished polycrystalline CVD diamond films as mentioned before for the friction and the wear examination (Fig. 1). The low friction coefficient $\mu=0.08$ has been achieved by a ball-on-disk examination using AISI52100 ball when the diamond film was polished up to $R_a=0.05\text{ }\mu\text{m}$, here R_a is the arithmetic average roughness⁸⁾. But the steel ball is easily worn out and the contact area

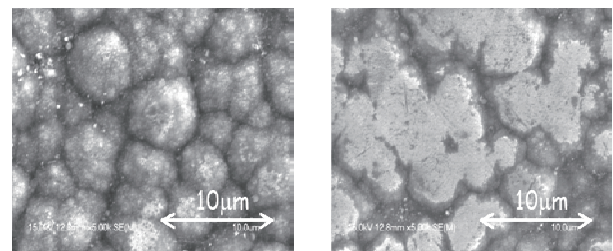


Fig.1. SEM images of as-deposited (top) and partially polished diamond films (bottoms). These films were deposited TiC substrates under the condition of table 1.

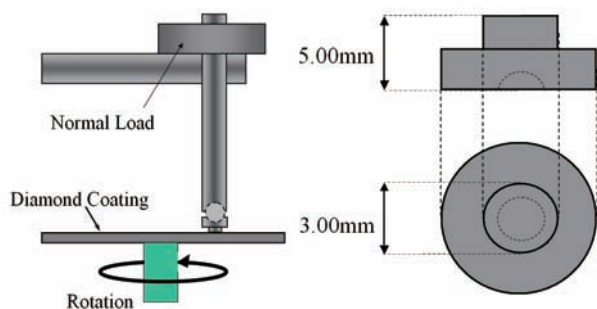


Fig.2 Schematics of pin of metals for friction test

increased remarkably, which cause the unstable behavior during the friction measurement.

In this paper, we focused on the friction properties between the diamond-metal contacts using the newly developed pin-on-disk (Fig. 2) instead of the conventional ball-on-disk. We investigated the relationship between friction coefficient and hardness of metals. Friction and wear test for the four kinds of metals has done in the nitrogen atmosphere, the ambient and dry air. Tested metals are as follows: D2 and AISI440C as the abrasion resistance and high hardness materials, AISI420 and AISI304 as the typical ferrite and austenitic stainless steels.

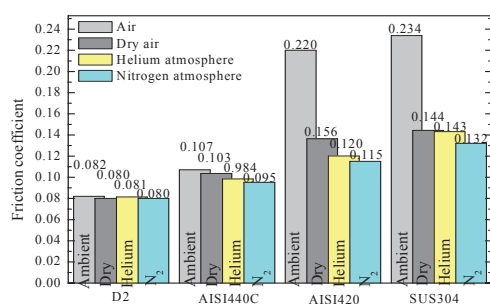


Fig.3. the difference of friction coefficient for each gas atmosphere; Disk : Polished CVD diamond on TiC substrate, $R_a=0.25\ \mu\text{m}$, Contact pressure 0.14 MPa, Sliding speed 0.20 m/s, Sliding cycle 20,000 cycles, 25-35 %RH(Air), 1.6 %RH(Dry Air) 15 %RH(N_2), 20-25deg.C

In the case of relatively hard metals, D2 and AISI440C, both the friction coefficient and wear volume are much lower than relatively soft metals, AISI420 and AISI304. We obtained very low ($\mu=0.08$) and stable friction coefficient, and small wear volume ($2.1 \times 10^{-9}\ \text{mm}^3/(\text{Nm})$) from D2 specimens.

We found the friction coefficient is strongly influenced by the level of humidity, and those differences occur notably in the case of relatively soft materials (Fig. 3).

In this paper, it clarified about the material dependence and atmosphere dependence of the friction coefficient of partially polished diamond film. It was shown clearly that the hardness of material and the humidity of the atmosphere are very important for friction properties.

References

- 1) M. Yoshikawa, N. Otake, chemical vapor deposition diamond, Ormsha, (1995), pp18-19.
- 2) M. Sommer, R. Haubner, B. Lux, Diamond and Related Materials **9**, (2000), pp 351-357.
- 3) T. Abe, T. Takagi, Z.M. Sun, T. Uchimoto, J. Makino, H. Hashimoto, Diamond and Related Materials **13**, (2004), pp 819-822.
- 4) R.B. Fischer, Nature **189**, (1961), 50.
- 5) B.R. Huang, C.T. Chia, M.C. Chang, C.L. Cheng, Diamond and Related Materials **12**, (2003), pp 26-32.
- 6) T.S. Yang, J.Y. Lai, C.L. Cheng, M.S. Wong, Diamond and Related Materials **10**, (2001), pp 2161-2166.
- 7) Y. Moriyoshi, M. Kamo, N. Setaka, Y. Sato, Journal of Materials Science **18**, (1983), pp 217-224.
- 8) T. Takeno, T. Komoriya, I. Nakamori, H. Miki, T. Abe, T. Uchimoto, T. Takagi. Diamond & Related Materials **14**, (2005), pp2118-2121.

Unsteady Aerodynamic characteristics of Wings in Ground Effect

T. Matsuzaki^{*}, S. Yoshioka^{**}, T. Kato^{**}, and Y. Kohama^{**}

^{*} Dept. of Mech. Eng., Tohoku University,

^{**} Institute of Fluid Science, Tohoku University

ABSTRACT

In spite of the great deal of effort has been made on researching the ground effect in the steady condition, little attention has been given to the ground effect in the unsteady condition. This paper is, therefore, intended as an investigation of the force generated and the flow around the wing when it undergoes unsteady movement at constant speed near the ground. And then it was proven that unsteady aerodynamic characteristics exist in the ground effect when moving in the direction of the height. The cause of these unsteady phenomena was the influence of the induced velocity. The induced velocity is derived from the starting vortex keeping on generating because the circulation around the wing continuously carried on changing when moving heightwise near the ground.

Key Words: ground effect, wing, vortex, unsteady flow

1. Introduction

The transportation system using ground effect is expected to become one of high speed and efficient transportation systems^{1, 2}. Kohama proposed a new transportation system using ground effect, which is called the “Aero-Train”³. Our research team has developed Aero-Train (Fig.1) and it has wings and flies near the ground inside a guide way using ground effect.

Aero-Train has been developed through wind tunnel testing and numerical simulation just like other aircraft. Wind tunnel testing and numerical simulation have often been applied to in the steady condition. But actual aircraft (including Aero-Train) are flying while undergoing unsteady movement like pitching, rolling, yawing, and heaving, etc.

Aircraft are developed based on the result of wind tunnel testing and numerical simulation, mainly in the steady condition. The aerodynamic force in the unsteady condition is usually calculated in the steady condition in each state, by assuming the unsteady forces to be quasi-steady.

However, ground effect is a phenomenon with unique characteristics even in the steady condition. The authors suggest that there is a phenomenon that has not been clarified in the ground effect in the unsteady condition.

Therefore, this research aims at the clarification of the force generated and the flow around the wing when it undergoes unsteady movement near the ground. This is carried out paying special attention to the phenomenon when the wing moves in the height direction, so the ground effect is a phenomenon that strongly depends on the height from the ground.

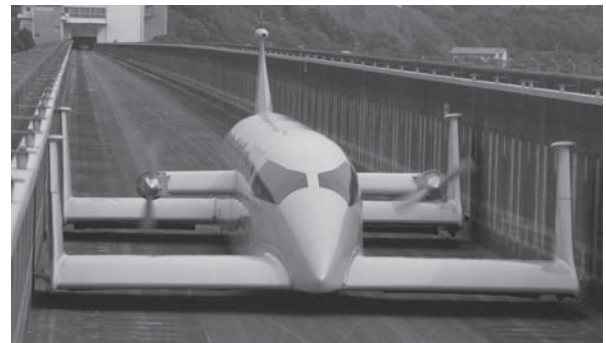


Fig. 1 Aero-Train test model.

2. Experiments

2.1. Experimental setup

At first, the aerodynamic characteristics with ground effect in the steady condition were measured in detail. And then, this data was used to identify the characteristics of the ground effect in the unsteady condition. Considering these results, the characteristics with ground effect were investigated in the unsteady condition about heaving motion.

Fig.2 shows the experimental setup. The wing model and the wing support parts fixed to the loadcells. The loadcells were moved up or down with electric sliders at constant speed. Aerodynamic forces were measured with the three momentum loadcells.

The measurement of the height from the ground was cross-checked by using a laser displacement sensor and the positional confirmation function of motor controller. The fixed ground plate was used to imitate the ground.

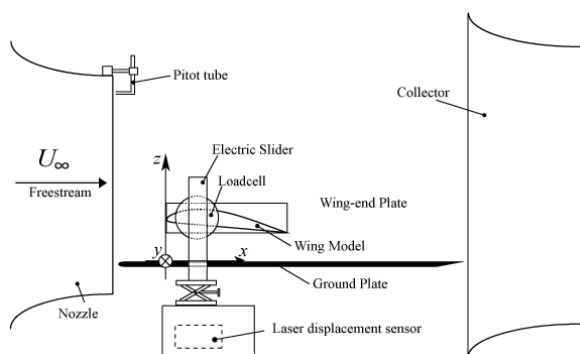


Fig. 2 Experimental setup

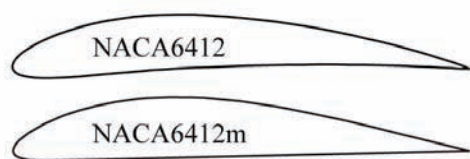


Fig. 3 Airfoils

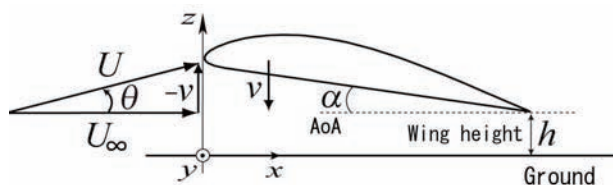


Fig. 4 Parameters and axis coordinates

Table 1 Parameters

Re	2.0×10^5
h/c	$0.01 \sim 1.0$
α	$1.0 \sim 5.0$ [deg]
θ	$0.1 \sim 1.0$ [deg]

2.2. Wing model

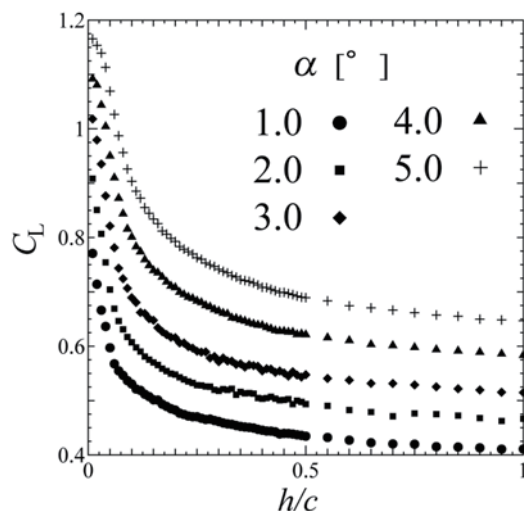
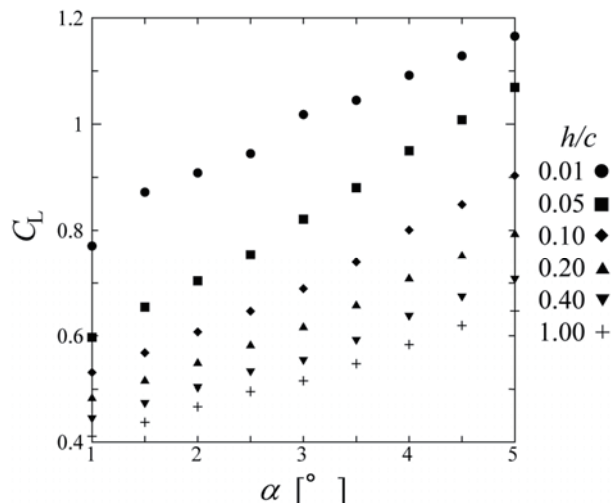
NACA6412-modified (NACA6412m) is used for the airfoil in this research. NACA6412m is improved to better shape based on NACA6412 in order to effectively use the ground effect wing. It has a flat bottom surface to suppress sucking at the lower surface, and the camber line is curved upwards at trailing edge area to decrease separation at the area.

The geometry of the wing model is recorded Fig. 3. The chord length c is 0.2 m. The span width b is 0.4 m. Aspect ratio A is 2.0.

2.3 Parameters

The Parameters are Reynolds number Re , height over chord length h/c , the angle of attack α , and the amount of change of the effective angle of attack θ .

The parameters and axis coordinates indicated in Fig.4. Reynolds number was based on the chord length and the freestream velocity. The parameters are shown in Table 1.

Fig.5 Lift coefficient as a function of h/c in steady conditionFig.6 Lift coefficient as a function of α in steady condition

3. Results and discussions

3.1. Results in steady condition

First, experiments were carried out in steady condition, and the base line result was obtained. Fig. 5 shows lift coefficient C_L vs. h/c and Fig. 6 shows C_L vs. α .

Fig. 5 shows that C_L nonlinearly increased as h/c became small. The inclination of the curve tended to become steep as h/c became small. This characteristic was seen in the ground effect.

Fig. 6 shows that C_L increased as the angle of attack became large.

Considering these results, the aerodynamic force in the unsteady condition is calculated in the steady condition in each state, by assuming the unsteady forces to be quasi-steady.

3.2. Results in unsteady condition

Actual value measured in the unsteady condition was compared with these identification values. The results where the effective angle of attack α_e were equated are shown. α_e is the sum of α and θ . θ is the amount of the changing of the effective angle of attack. θ is defined by freestream velocity U_∞ and the heaving speed v (Fig.4).

In this time, the one effective angle of attack α_e was used as an object of comparison. All of their α_e is 4 degrees. One is where α is 3 degrees and θ is +1 degrees. Another is where α is 4 degrees and θ is 0 degrees (no move). The other is where α is 5 degrees and θ is -1 degrees.

Fig. 7 (a) shows that the drag coefficient C_D changed when the wing moved up or down. When the wing moved down, the value measured was lower than the value identified. The value measured was, on the other hand, higher than the value identified when the wing moved up. This is because the axis of the lift and drag was inclined by the change in effective angle of attack (Fig.8). Fig. 7 (b) shows the results, taking the change in the inclination of the axis into consideration. These values identified and the actual values measured were nearly equal if this was taken into consideration. The inclination of the axis is taken into consideration for identifying at all the following.

Fig. 9 shows that the lift coefficient C_L changed when the wing moved up or down. When the wing moved down, the value measured was lower than the value identified. On the other hand, the value measured was higher than the value identified when the wing moved up.

Fig. 10 shows that lift coefficient C_L changed if the amount of effective angle of attack changed. It shows that the larger the change in effective angle of attack is, the more the gap grew.

The reason why there is the difference between the value identified and the value actual measured is the changing of the induced velocity around the wing. For example, it treats when wing moving down.. Lift force increases as the ground approaches. Another way of saying, the circulation around the wing increases as the ground approaches. In fact, the circulation around the wing kept changing when the wing moved down (Fig.11).

The circulation around the wing kept changing and the starting vortex kept being generated at the same

time while the wing moved down in the direction of height. As a result, the starting vortex inclined the effective angle of attack. For example, the starting vortex was generated and the downwash was strengthened when the wing moved down. The downwash worked to decreasing the effective angle of attack, so the lift coefficient came down. In consequence, the difference between the value identified and the value actual measured is occurred.

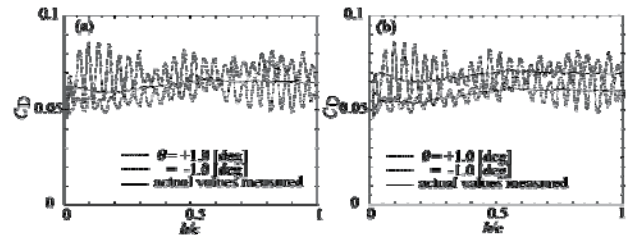


Fig. 7 The drag coefficient as a function of h/c in unsteady condition

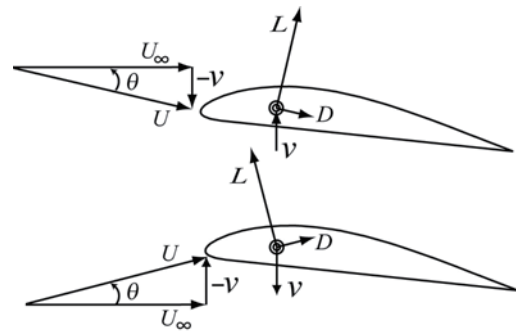


Fig. 8 The inclination of the axis

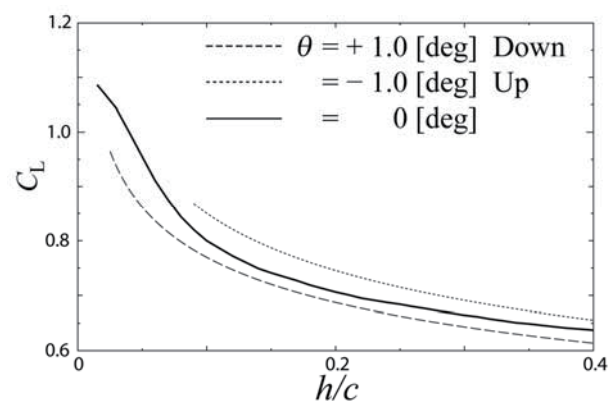


Fig. 9 The lift coefficient as a function of h/c in unsteady condition

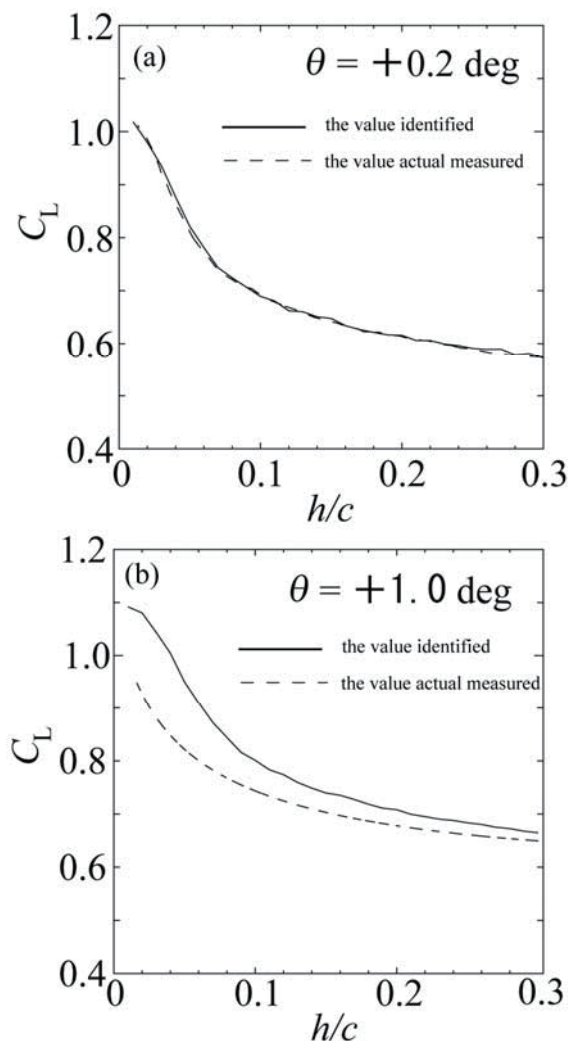


Fig. 10 The difference of the amount of effective angle of attack changed

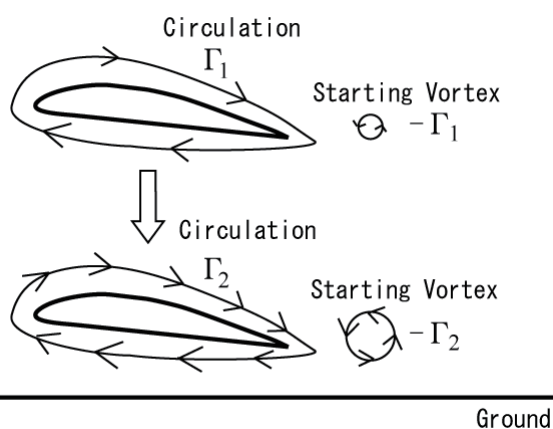


Fig. 11 The reason why the difference was occurred

4. Conclusion

This study demonstrates that it paid attention to clarify the unsteady characteristics of wings in the ground effect for the improvement of the flight performance of the WIG crafts.

Unsteady characteristics couldn't be estimated from the steady characteristics in the ground effect when moving in the direction of the height.

The unsteady characteristics are caused by the changing of induced velocity around the wing. This phenomenon is peculiar to the ground effect.

The nearer the distance between the wing and the ground is, the more remarkable the unsteady characteristics becomes.

Moreover, these unsteady characteristics are decided depending on the direction of the movement and the speed of the movement.

It will be possible to contribute to the stability improvement of the WIG vehicles if the control law is constructed taking this unsteady characteristic into consideration when the WIG vehicles are put to practical use in the future.

References

- 1) R.G.Ollila: Historical Review of WIG Vehicles, *Journal of Hydronautics*, **14**, (1980), pp.66-76.
- 2) R.H. Lange, and J.W. Moore : Large Wing-in-Ground Effect Transport Aircraft, *Journal of Aircraft*, **17**, No.4, (1980), pp.260-266.
- 3) Y.Kohama: *Aero-Train and Earth's Environment*, (2004), Science and Engineering Review Publisher, Tokyo. (in Japanese)
- 4) T.Matsuzaki: Abstracts of the third International Symposium on Transdisciplinary Fluid Integration, Miyagi, June. (2006), P.39-40.

LDV measurements of Unsteady Blade Suction-Surface Flow of an Axial-Flow Turbine Rotor

Takayuki Matsunuma

National Institute of Advanced Industrial Science and Technology (AIST)
1-2-1 Namiki, Tsukuba, Ibaraki, 305-8564, Japan

ABSTRACT

The unsteady flow field of an axial-flow turbine rotor was investigated experimentally using a laser Doppler velocimetry (LDV) system. Detailed measurements of the time-averaged and time-resolved distributions of the velocity, flow angle, turbulence intensity, etc. were carried out at a low Reynolds number condition, $Re_{out,RT} = 3.5 \times 10^4$. The data obtained were analyzed from the viewpoints of both an absolute (stationary) frame of reference and a relative (rotating) frame of reference. The effect of the turbine nozzle wake and secondary vortices on the rotor flow field was clearly captured. It was found that the nozzle wake and secondary vortices are suddenly distorted at the rotor inlet, because of the rotating potential field of the rotor. The nozzle flow (wake and secondary vortices) and the rotor surface flow (boundary layer flow) interact intensively inside the rotor passage. The periodic fluctuation of the relative velocity on the rotor suction surface due to the nozzle effect is as much as 20% of the mean rotor exit velocity.

Key Words: LDV measurement, Axial-flow turbine, Rotor, Unsteady flow, Wake, Secondary vortex

1. Introduction

The flow field around turbine blades is very unsteady and complex due to “rotor-stator interaction,” the aerodynamic interaction between the turbine nozzle (stator) and the turbine rotor. Boundary layer behavior, loss generation, secondary vortex growth, and heat transfer in turbines are strongly affected by the rotor-stator interaction. Even though unsteady flow plays an important role in axial-flow turbines, turbines are mainly designed using steady-flow calculations. Because few actual models exist for the loss-generating mechanisms seen in unsteady flow, empirical correlations are used to account for the effects of unsteadiness. Therefore, more knowledge on unsteady rotor-stator interaction is essential to increase the performance of turbines. Although a variety of measurement techniques can easily be applied to the flow field within the stationary blades, difficulties arise with measurements of the flow field within the rotating blades. Binder et al. [1], Zaccaria and Lakshminarayana [2], Göttlich et al. [3], and Matsunuma [4] used laser measurement systems, such as laser two-focus velocimetry (L2F), laser Doppler velocimetry (LDV), and particle image velocimetry (PIV).

This paper focuses on the unsteady effect of turbine nozzle wake and secondary vortices (passage vortex and trailing edge vortex) on the suction surface flow of an axial-flow turbine rotor.

2. Experimental Facility and Method

2.1 Annular turbine wind tunnel and turbine cascade

Figure 1 shows the annular turbine wind tunnel used in the experiment. This wind tunnel is an air suction type, open circuit facility. The total length of the wind tunnel is approximately 3.8 meters. The outside and inside annular wall diameters of the test section are 500 mm and 350 mm, respectively. A single-stage axial-flow turbine designed using a free vortex method to attain radial equilibrium was installed at the test section. The geometries and specifications of the turbine nozzle and rotor cascades are shown in Fig. 2, Fig. 3, and Table 1.

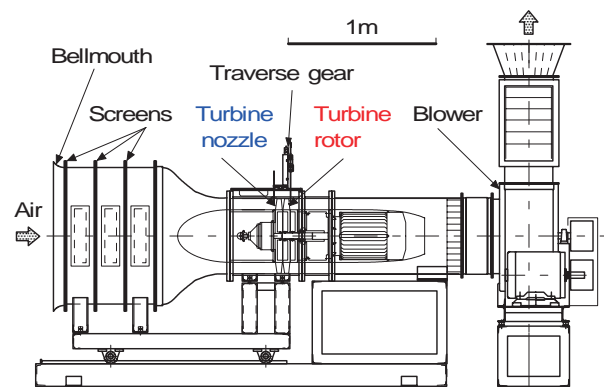


Figure 1 Annular turbine wind tunnel

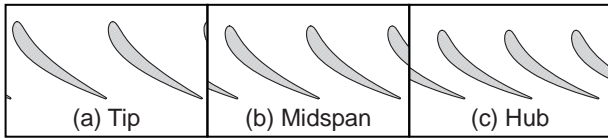


Figure 2 Geometry of turbine nozzle

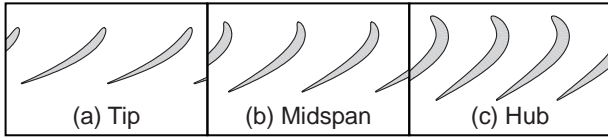


Figure 3 Geometry of turbine rotor

Table 1 Specifications of turbine cascades

	Nozzle			Rotor		
	Tip	Mid	Hub	Tip	Mid	Hub
	28			31		
Chord, C mm	69.1	67.6	66.1	58.5	58.5	58.5
Axial chord, C_{ax} mm	45.0	42.5	40.0	32.3	40.9	48.0
Blade span, H mm	75.0			74.0		
Blade pitch, S mm	56.1	47.7	39.3	50.7	43.1	35.5
Aspect ratio, H/C	1.09	1.10	1.13	1.26	1.26	1.26
Solidity, C/S	1.23	1.42	1.68	1.15	1.42	1.65
Inlet flow angle, α_1 deg	0.0	0.0	0.0	-16.5	21.8	51.7
Exit flow angle, α_2 deg	63.9	67.4	71.1	66.9	63.4	58.7
Stagger angle, ξ deg	49.3	51.0	52.7	55.9	47.6	33.4
Inner diameter, D_1 mm	350			350		
Outer diameter, D_2 mm	500			500		
Hub / tip ratio, D_1/D_2	0.7			0.7		
Tip clearance, τ mm	0.0			1.0		

2.2 LDV measurement system and data analysis method

A photograph of the wind tunnel and the LDV measurement system is shown in Fig. 4. The LDV system was a standard two-color, four-beam, two-dimensional measuring system with a fiber-optic probe (System 90-3, TSI Inc.). The system consisted of a 4 W argon-ion laser tuned to 488 nm (blue) and 514.5 nm (green) output. The fiber-optic probe was mounted on a three-dimensional traverse gear. The half-angle between the beams was 4.29 deg. and the calculated dimensions of the measurement volume at e^{-2} intensity locations were 0.85 mm in length and 0.073 mm in diameter. Dantec Safex standard fog fluid with a mean particle diameter of 1.068 μm was used to seed the flow. The liquid was atomized using a Dantec Safex Model 2001 fog generator. Tracer particles were introduced into the test section from the wind tunnel inlet. An incremental rotary encoder (1,800 pulses/revolution) was attached to the rotor shaft to detect the rotor angular position. An automatic measurement system controlled by a personal computer was adopted in this study, and all measured data were stored on a hard disk in the computer.

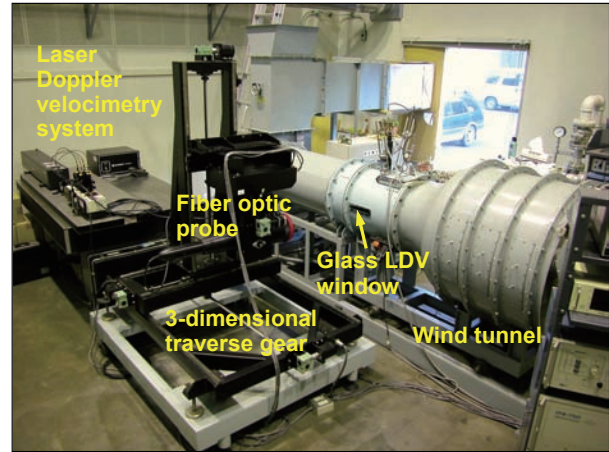


Figure 4 Wind tunnel and LDV system

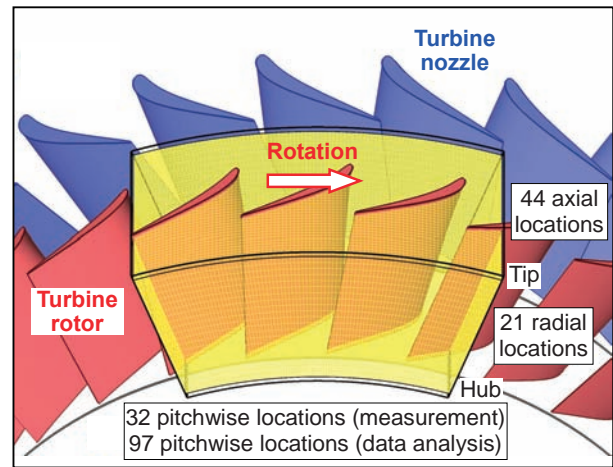


Figure 5 LDV measurement locations

Figure 5 shows the LDV measurement locations around the rotor. Measurements were taken at 44 axial locations from immediately downstream of the nozzle to downstream of the rotor (an axial interval of 2 mm), 21 spanwise locations (from 3.3% span to 96.7% span), and 32 pitchwise locations for one pitch of the nozzle. Ninety-seven pitchwise data (three nozzle pitches) were displayed in the subsequent data analysis to make the flow clearly intelligible. Since two-dimensional LDV was applied, the axial and circumferential velocities (V_z and V_x) were measured. At each measurement point, 10,000 instantaneous velocity samples were collected. Ensemble averaging of the instantaneous velocity data was performed with the help of the rotor encoder signal. The relative velocity V_{Rel} and turbulence intensities Tu_{Rel} were calculated as follows:

$$V_{Rel} = \sqrt{V_z^2 + (V_{x,Abs} + V_{RT})^2} / V_2$$

$$Tu_{Rel} = \sqrt{\frac{v_z'^2 + v_x'^2}{2}} / V_2$$

All data presented in this paper are nondimensional. The time-averaged, pitchwise-averaged, and spanwise-averaged relative velocity

V_2 at the rotor exit ($V_2 = 9.27$ m/s) made the velocity and turbulence intensity in the relative frame of reference dimensionless.

It should be noted that this paper describes rotor synchronous unsteady effects because the ensemble averaging purges all nonrotational effects, such as instabilities, trailing edge vortex shedding, etc.

The Reynolds number used during the experiment was set at $Re_{in,NZ} = 2.0 \times 10^4$ based on the nozzle chord length and nozzle inlet velocity. The reason for using the Reynolds number of the nozzle inlet $Re_{in,NZ}$ was because the flow condition at the nozzle inlet is easy to measure. The Reynolds number based on the rotor chord length and rotor exit velocity $Re_{out,RT}$ was calculated as 3.5×10^4 from the measured LDV data. The axial velocity at the test section was 4.47 m/s and the rotor speed was set at 402 rpm to attain the design operating condition (design rotor inlet flow

angle). The flow in this experiment was considered to be incompressible because the Mach number was very low. The Mach numbers based on the mass-averaged velocities at the nozzle inlet, nozzle outlet, rotor inlet, and rotor outlet were $M_{in,NZ} = 0.013$, $M_{out,NZ} = 0.031$, $M_{in,RT} = 0.014$, and $M_{out,RT} = 0.027$, respectively. The author would like to note that the flow in actual gas turbines should be considered compressible because those Mach numbers are typically $M_{out} = 0.5$ to 1.2.

3. Results and Discussion

Figure 6 shows the time-averaged flow close to the rotor suction surface. Figures 6(a) and 6(b) show the relative velocity and the turbulence intensity, respectively. The main flow moves from right to left as indicated by the light green arrows in these figures. In Fig. 6(a), a large boundary layer region associated with the low relative velocity was observed at the rear section of the suction surface. This is because the thickness of the boundary layer developed from the rotor leading edge increases rapidly at the adverse pressure gradient region on the rear part of the suction surface. The existence of flow separation on the suction surface could not be confirmed from the LDV measurements because of insufficient measurement resolution in the boundary layer region. The pink solid line in the figure indicates the thick boundary layer onset line, which was defined as the position with the maximum velocity gradient (largest decrease in velocity). Low relative velocity regions due to the rotor tip leakage and passage vortex are observed near the tip and hub endwalls. In Fig. 6(b),

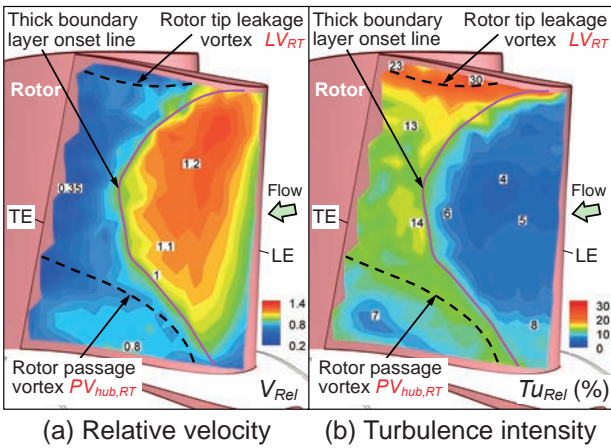


Figure 6 Time-averaged flow on rotor suction surface

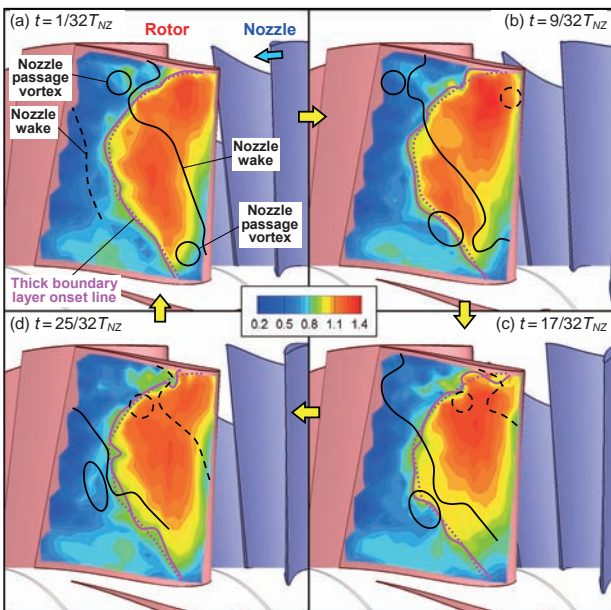


Figure 7 Time-resolved relative velocity on rotor suction surface

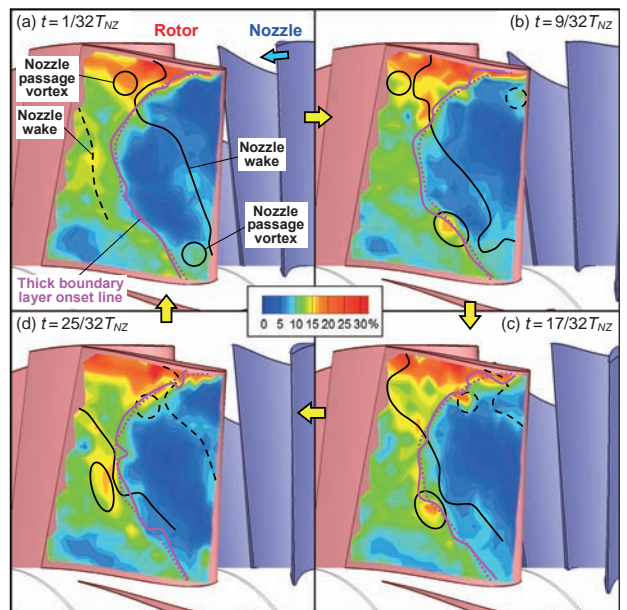


Figure 8 Time-resolved turbulence intensity on rotor suction surface

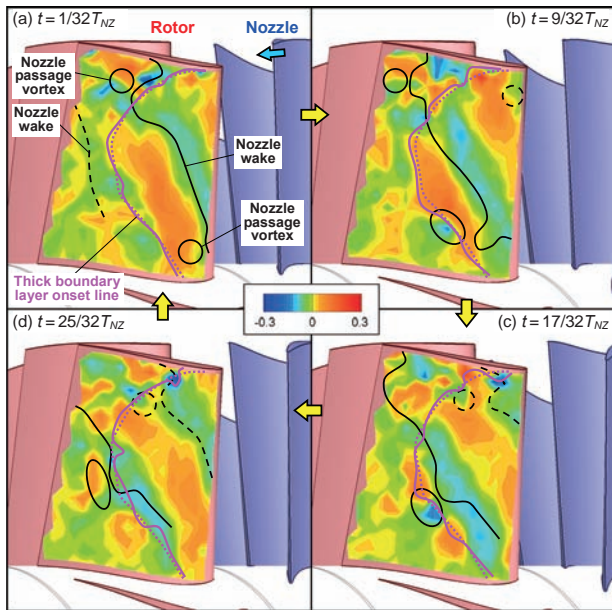


Figure 9 Periodic fluctuation of time-resolved relative velocity on rotor suction surface

the turbulence intensity increases dramatically behind the thick boundary layer onset line. The tip leakage vortex generates a high turbulence intensity region near the tip endwall. The maximum value of the turbulence at the tip leakage vortex region is approximately 30%.

Figures 7 and 8 show the time-resolved relative velocity and turbulence intensity close to the rotor suction surface, respectively. Figures 9 and 10 show the periodic fluctuations of the time-resolved relative velocity and turbulence intensity close to the rotor suction surface, respectively. The periodic fluctuations were obtained by subtracting the time-averaged distributions in Fig. 6 from the time-resolved distributions in Figs. 7 and 8. The pink solid lines in these figures indicate the time-resolved thick boundary layer onset lines. In order to observe the unsteady motion of the lines, the time-averaged thick boundary layer onset line in Fig. 6 is superimposed on the figures, as indicated by the pink dotted lines. The approximate positions of the nozzle wake and the nozzle passage vortices are shown by the black lines and circles in the figures. The black line was defined as the high turbulence intensity position due to the nozzle wake and passage vortices. The nozzle wake and passage vortices generate large fluctuations of the relative velocity and turbulence intensity on the rotor suction surface. The range of periodical fluctuation of the relative velocity due to the nozzle effect is about 20% of the mean exit velocity V_2 . The nozzle wake and passage vortices also have a moderate effect on the boundary layer

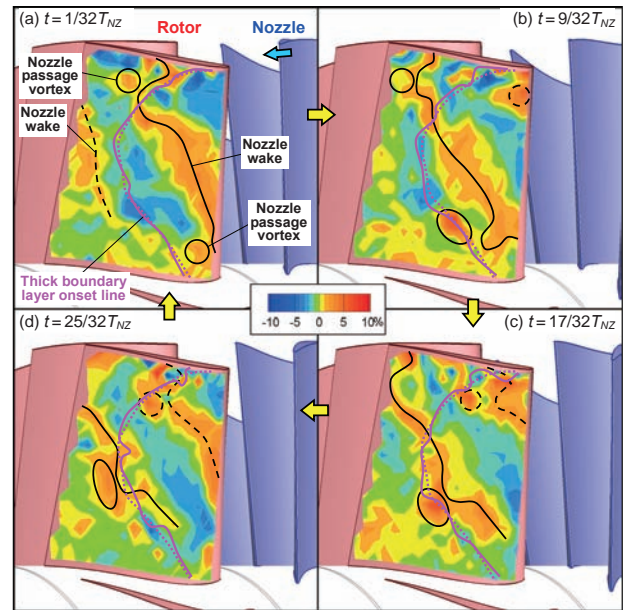


Figure 10 Periodic fluctuation of time-resolved turbulence intensity on rotor suction surface

region. The interaction between the rotor boundary layer flow and the nozzle wake and passage vortices generates complex local skews on the thick boundary layer onset line. It is evident that the thick boundary layer onset line locally moves upstream under the effect of the nozzle wake.

4. Summary

Laser Doppler velocimetry (LDV) was successfully applied to provide detailed experimental data on the time-resolved unsteady flow fields around the rotor of a single-stage axial-flow turbine at a low Reynolds number ($Re_{out,RT} = 3.5 \times 10^4$). The complex aerodynamic interactions between the turbine nozzle and the turbine rotor were described in detail. The periodic fluctuation of the relative velocity on the rotor suction surface due to the nozzle effect is as much as 20% of the mean rotor exit velocity. The nozzle wake and passage vortices generate complex local skews of the thick boundary layer onset line.

References

- [1] Binder, A., Forster, W., Mach, K., and Rogge, H., 1987, *ASME J. of Turbomachinery*, Vol. 109, pp. 251–257.
- [2] Zaccaria, M. A., and Lakshminarayana, B., 1995, *ASME J. of Turbomachinery*, Vol. 119, pp. 201–224.
- [3] Göttlich, E., et al. Woisetschlager, J., Pieringer, P., Hampel, B., and Heitmeir, F., 2006, *ASME J. of Turbomachinery*, Vol. 128, pp. 178–187.
- [4] Matsunuma, T., 2007, *ASME J. of Turbomachinery*, Vol. 129, pp. 360–371.

Observation of the feedback loop associated with airfoil trailing-edge noise

Y. Konishi and S. Takagi

Institute of Aerospace Technology, JAXA

ABSTRACT

It is well known that acoustic noise emanated from an airfoil trailing edge is discrete. The mechanism on why the noise becomes discrete and how the frequency is selected remains unclear. To reveal the mechanism, the boundary layer near the trailing edge on the pressure side was artificially disturbed with the use of distributed roughness elements. As a result, the separation is swept away and an acoustic sound is suppressed. The experimental results indicate that the frequency of trailing-edge noise is determined in separation region where mean velocity distribution has an inflection point accompanying reverse flow. These are necessary conditions for absolute instability.

Key Words: trailing-edge noise, boundary layer instability, absolute instability

1. Introduction

Tonal noise is emanated from the trailing-edge (T-E) of 2-D airfoils at moderate Reynolds numbers. Most prevailing explanation is ascribed to the feedback loop between T-E noise and T-S waves growing in the boundary layer on the pressure side. Nash et al reveal that the T-S waves near the trailing edge are preferentially amplified and play an important role in frequency selection.⁽¹⁾ (Fig.1) But they could not explain why the discrete tone was observed and how the frequency is selected. The T-S instability is inherently unstable to broad-band disturbances, indicating that other mechanisms associated with an absolute instability⁽²⁾ is required. Considering the fact that separation is observed near the trailing-edge on the pressure side when T-E noise is emanated, the experiment is performed in configuration to suppress T-E noise by manipulating the boundary layer near the trailing edge on the pressure side.

2. Experimental Setup and Procedure

The experimental set-up is shown in figure 2. The experiment is conducted in the JAXA low turbulence wind tunnel with a rectangular test-section of 550mm by 650mm in cross section. The free-stream velocity U_∞ was chosen at 14.5m/s. At this velocity, the free-stream turbulence level is less than 0.05%.

The wing model is NACA0015 cross-section whose chord length and spanwise length are 400mm and 550mm, respectively. The wing was set horizontally in order for the pressure side of the airfoil to become upper side. So that the hot-wire probe from the ceiling can be readily surveyed on the pressure side.

The streamwise velocity, whose time-mean and fluctuation components are denoted by U and u respectively, is measured with a constant temperature hot-wire anemometer. The hot-wire sensor is 5 μ m in diameter and 1mm in length of the tungsten. The hot-wire probe is traversed in the x - and y - directions.

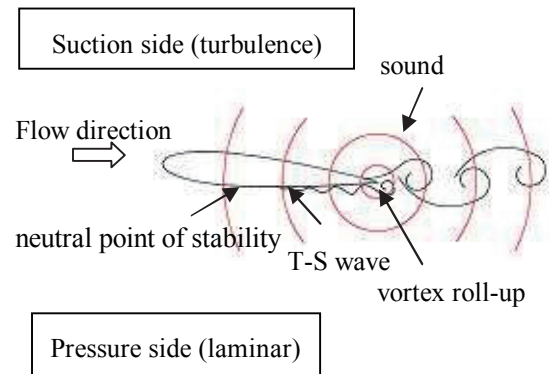


Figure 1. Diagram of the T-E. noise generation

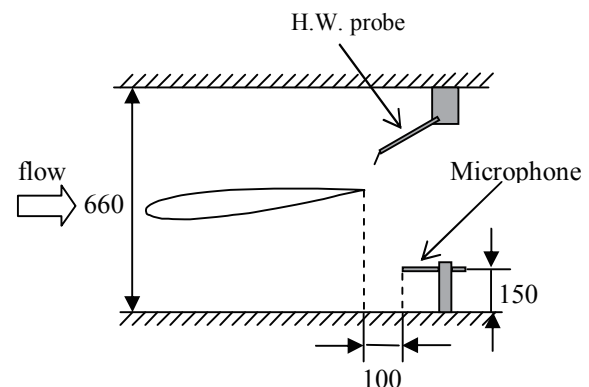


Figure 2. Experimental setup. (dimension is in mm)

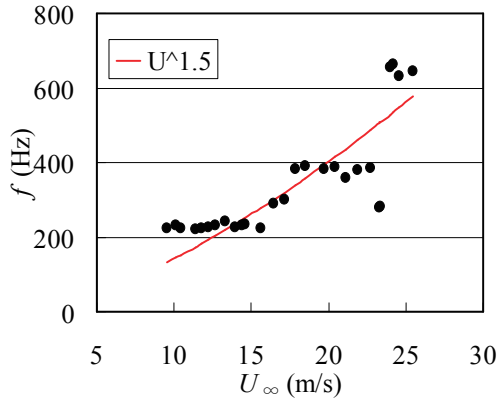


Figure 3. Sound pressure frequency VS uniform velocity. Line shows $U^{1.5}$ dependency

The acoustic sounds are measured by the microphone, B&K type 4138, which is located 100mm behind the T.E and 300mm toward the suction side of the airfoil. The velocity and acoustic sounds data are stored in personal computer with the use of an A/D converter.

Previous experimental observations showed that the T-S wave is abruptly amplified in separation region near the trailing edge and then discrete sound is emitted when the amplified T-S wave is shed from the trailing edge. Therefore, acoustic sound should be weakened or suppressed, if the separation structure can be destroyed. According to this speculation, isolated roughness elements with 3mm in diameter and 4mm in height were distributed in staggered formation at 92.5% of the chord length on the pressure side.

3. Results and Discussion

Some fundamental results are shown in Figs.3 and 4. Figure 3 shows the frequency dependency of the sound against the uniform velocity. As numerous researchers observed⁽³⁾, a ladder-like structure with $U^{1.5}$ is observed. But each step does not fit to $U^{0.8}$ but rather fit to constant. This behavior is identical to the result observed by Nash et al. before the anechoic test section is used, which allows the reflections of the sound at a hard wall. The step-like structure in Fig. 3 seems to be due to the test section without anechoic treatment. We do not discuss any more about this constant behavior, because this point is away from the present subject on the frequency-selection mechanism of the T-E noise.

Figures 4 (a) and (b) show typical frequency spectra of the sound pressure for the free stream velocity of 14.5m/s with and without the distributed roughness, respectively. Also the background noise spectrum in the empty test section is superimposed in black line. In natural case, the tonal noise is clearly

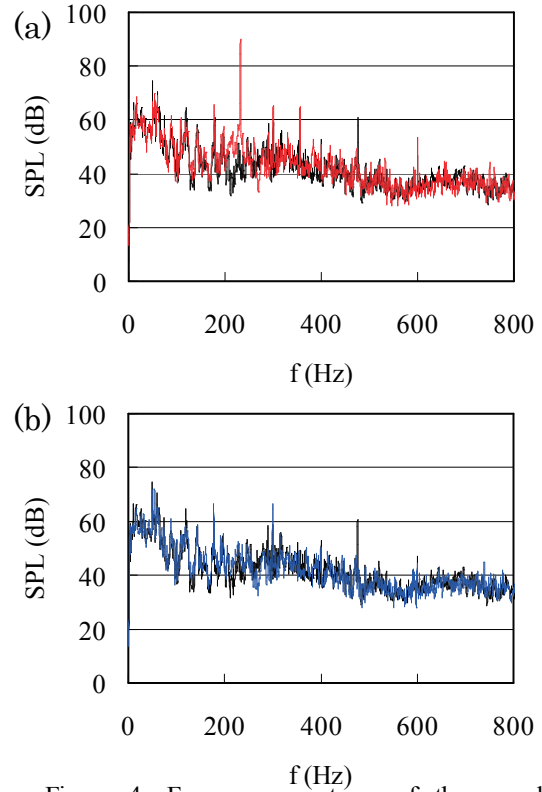


Figure 4. Frequency spectrum of the sound pressure.

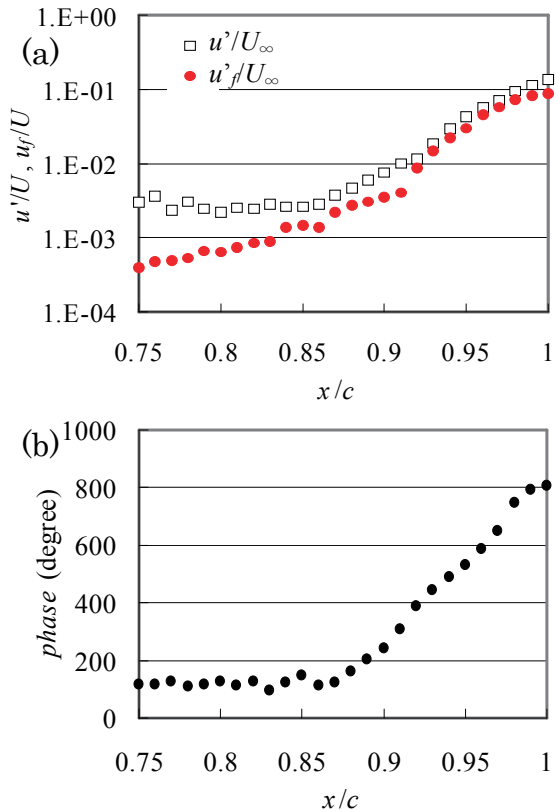


Figure 5. Disturbance development and its phase distribution in the chordwise direction on the pressure side. Phase shifts are obtained from using the microphone as a reference signal.

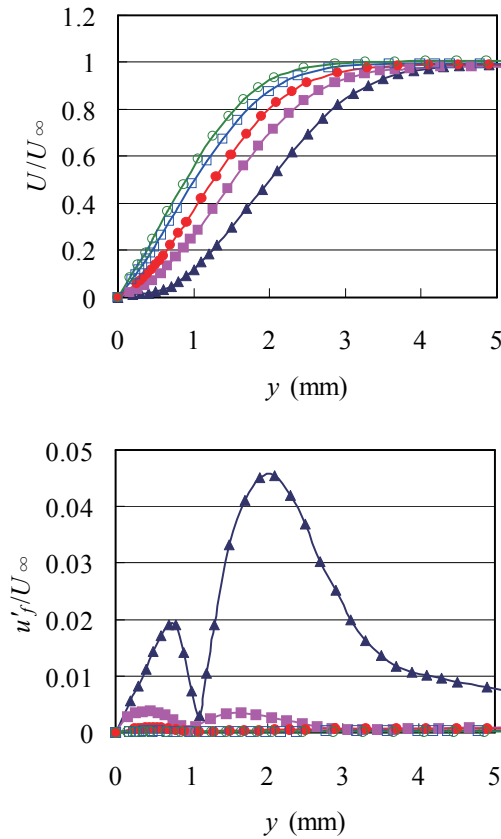


Figure 6. Velocity distribution and RMS distribution of the T-E. noise component.
 \circ : $x/c=0.75$, \square : $x/c=0.8$, \bullet : $x/c=0.85$, \blacksquare : $x/c=0.9$,
 \blacktriangle : $x/c=0.95$.

observed at 232 Hz. Once the boundary layer on the pressure side is artificially disturbed, this tonal noise disappeared, suggesting that the distributed roughness elements prevent the 2-D vortex shedding, which generates strong acoustic emission.

Figure 5 (a) shows disturbance growth against the chordwise direction on the pressure side, where u' and u'_f denote the total RMS value and the RMS value of the discrete frequency component. The discrete frequency coincides with the tonal noise frequency in the sound pressure. As can be seen from the total RMS value, the disturbances start exponentially to grow downstream of $x/c=0.875$. The discrete frequency component and its higher harmonics contributes in the exponential growth. Therefore, the flow is highly periodic. Since the magnitude of the overall disturbance exceeds 10% of the free stream velocity U_∞ at the verge of the airfoil, significantly strong vortex should be shed from the trailing edge.

Figure 5 (b) shows the phase differences between velocity fluctuation u and sound pressure measured by the microphone against the chordwise direction. Because of a limited range of the measurement area, the delay of sound pressure at each measurement

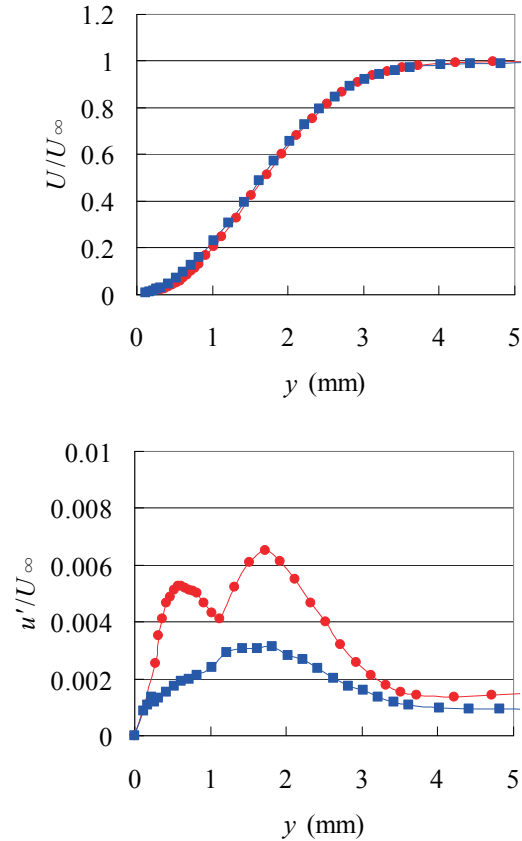


Figure 7. Mean velocity distribution and RMS(O.A) distribution at $x/c=0.9$ just upstream of the distributed roughness. \bullet : natural case, \blacksquare : artificially disturbed case.

position is not considered. Upstream of $x/c=0.875$, no phase change is observed, indicating that the discrete component fore of this location in Fig.5 (a) is not the velocity fluctuation but the sound pressure radiated from the trailing edge. This is the reason why the hot-wire anemometer is sensitive to the acoustic fluctuations as well as the velocity components. The phase velocity of the growing discrete disturbance is about 40% of the free-stream velocity U_∞ deduced from the wave length. This observed value is identical to the phase velocity of T-S waves.

Figure 6 (a) and (b) show distributions of the mean velocity and RMS value of the tonal noise component in y direction at various x locations. It is clearly visible that the velocity profile is inflectional, which destabilizes the flow leading to rapid growth of the disturbance.

Figure 7 shows distributions of the mean velocity and the overall RMS value of velocity fluctuation just upstream of the roughness elements, where no tonal noise is perceptible. No effect of the roughness is visible in the mean velocity distribution even though the flow downstream of the roughness is drastically changed from laminar to turbulent state, although the

RMS profile is definitely altered. This alteration suggests that without acoustic forcing there is no massive amplification of disturbance fore of this x -position. Thus, the condition that the mean velocity profile has an inflectional profile is not a sufficient condition of the amplification of the disturbances.

Figure 8 shows the frequency spectra of the u -component at $x/c = 0.9$. Discrete u -component disappeared in the presence of distributed roughness even if the mean velocity profile is still inflectional. Instead of discrete u -component, a moderate broadband bump is observed in slightly higher frequency region than that of the discrete u -component. This is due to the fact that naturally growing instability waves consist of broad-band components. Also, there is another difference in spectra that the lower frequency components than that of the discrete u -component are attenuated. This indicates that the mean flow of the boundary layer in no roughness case is fluctuating at low frequency associated with the fact that the separation point on the pressure side is unsteady.

This disappearance of the discrete component documents that there obviously exists an acoustic feedback loop between tonal noise and u -component. Also, the result suggests that the disturbance rapidly grows when the mean velocity profile instantaneously contains a reverse flow in a laminar separation bubble.

4. Conclusion

In order to reveal the frequency-selection mechanism of the 2-D airfoil trailing-edge noise, we focused on the relation between tonal noise and flow separation near the trailing-edge region. To remove the separation, the distributed roughness elements were adhered on the airfoil near its trailing edge and eventually sound emission was suppressed.

For the case with no roughness elements, the discrete disturbance, the so-called T-S wave, grows in the boundary layer where an inflectional point accompanying reverse flow was observed on the mean velocity profile.

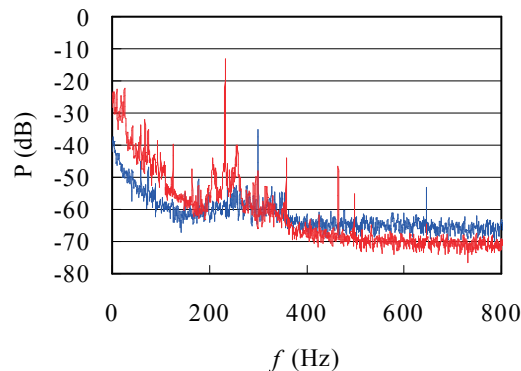


Figure 8. Frequency spectra of the velocity fluctuations at $x/c=0.9$. Red line: natural case, blue line: artificially disturbed case.

When the boundary layer near the trailing edge on the pressure side was disturbed, a tonal noise disappeared. This is because the boundary layer near the trailing edge becomes turbulence and reverse flow was removed. The mean velocity profile does not change upstream of the roughness and an inflection point still exists. However, no rapid growth of disturbances is observed. These results represent that in addition to an inflection point on the profile a recirculation near the trailing-edge is essentially necessary for the noise generation.

It can be finally concluded that the frequency of the trailing-edge noise is selected in the laminar separation region, where the mean velocity distribution in the normal-to-wall direction has an inflection point and reverse flow, both of which are necessary conditions for absolute instability⁽³⁾.

References

- 1) E. C. Nash, M. V. Lowson, and A. McAlpine: J. Fluid Mech., 382, (1999), pp.27-61.
- 2) P. Huerre and P. A. Monkewitz, Annu. Rev. Fluid Mech. 22, (1990), pp.473-537.
- 3) R. W. Paterson, P. G. Vogt, M. R. Fink, and C. L. Munch, J. Aircraft. (1973), pp.296-302.

Momentum and energy transfer characteristics in nanoscale Couette flow and at solid-liquid boundaries

D. Torii and T. Ohara

Institute of Fluid Science, Tohoku University

ABSTRACT

A Couette flow in an ultra-thin liquid film confined between solid plates has been studied by molecular dynamics simulations. Water was assumed for the liquid film, to which a shear is given by the relative motion of two solid walls. Thermal energy is generated by so-called 'viscous heating', resulting in a heat conduction as well as a transfer of momentum in the system. It was revealed that there is little velocity slip at the boundary even the shear stress is as high as the order of 10^2 MPa, which is contrary to the case with monatomic or linear molecules that showed a large velocity jump.

Key Words: Nanoscale flow, Solid-liquid boundary, Energy transfer, Momentum transfer

1. Introduction

Analysis of solid-liquid interfaces to clarify their characteristics of thermal energy transfer and momentum transfer is important not only for basic research on nonequilibrium microscopic thermal and fluid phenomena, but also for practical applications, such as lubrication control under extreme conditions, fabrication of low friction surfaces, and the development of new lubricants.

We have been working on molecular dynamics simulation of sheared liquid films confined by solid surfaces, where both energy and momentum transfer are present simultaneously. Monatomic and linear molecules were employed as liquid and various interesting findings were reported by the previous study.^{1,2} In the present report, liquid water film is analyzed and the characteristics of the energy and momentum transfer at the solid-liquid interfaces are examined by employing four different solid surfaces, whose configuration have been found to have great influences on those characteristics in cases of monatomic and diatomic liquid films.³

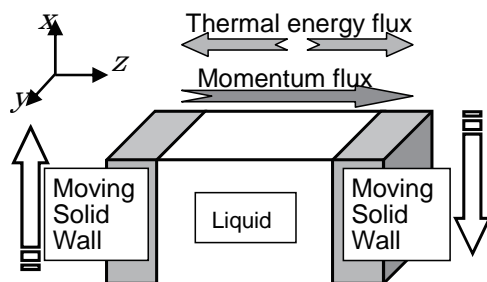
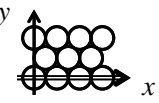
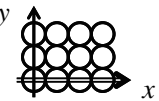
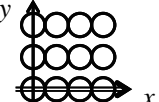
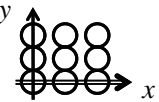


Fig. 1 Simulation system

2. Molecular Dynamics Simulation

The simulation system employed in the present study is shown in Fig. 1. The system consists of two parallel solid walls and a liquid film between them. The solid walls at each end of the cell moved in the x direction with velocities of the same magnitude and in opposite directions. As a result, the momentum flux is generated in the liquid film, liquid temperature being raised by the viscous heating, and the generated thermal energy is transferred to the solid walls. The velocity of solid wall was selected to be ± 100 m/s. The thickness of the liquid film was set to

Table 1 Solid walls employed in the simulation

	Surface molecular number density	Surface crystal plane	Surface molecular configuration	Numbers of atoms in x and y directions
A	Largest	FCC (1,1,1)		20×20
B	↑ ↓	FCC (1,0,0)		20×17
C	Small	FCC (1,1,0)		20×12
D				12×20

be $5\sigma_{OO}$ (a few nanometer). Periodic boundary conditions were applied in the x and y directions.

The four solid walls used in the simulation are shown in Table 1. Interaction between the solid molecules is modeled by the harmonic potential with parameters for platinum. The spring constant, equilibrium distance, and mass of molecules are 46.8 N/m, 2.77×10^{-10} m, and 3.24×10^{-25} kg, respectively. Outside the solid molecules, the phantom molecules⁴ are installed to model a semi-infinite solid at a constant temperature of 300 K.

For water, the SPC/E potential, which is the most successful potential model that reproduces various thermophysical properties and equation of state of real water, was applied. For the potential between a water molecule and a solid molecule, the work of Kimura and Maruyama⁵ has guided us and the SH potential⁶ was applied.

3. Simulation Results

For the case with wall B, the macroscopic flow distribution and the temperature distribution are shown in Fig. 2. A Couette-like flow is observed in the liquid film and there is almost no slip at the solid-liquid interfaces, which is contrast to the fact

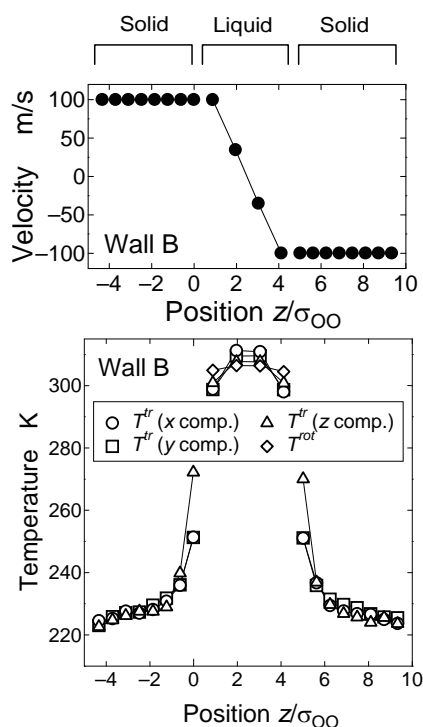


Fig. 2 Velocity (upper panel) and temperature (lower panel) distribution in liquid water film and platinum solid walls. The temperature shown here corresponds to kinetic energy of molecules in each degree of freedom.

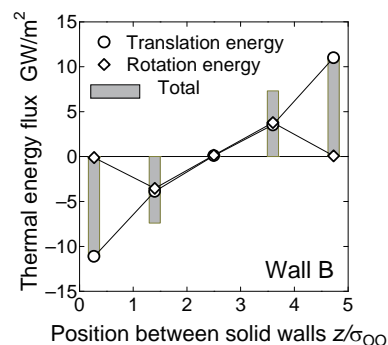


Fig. 3 Thermal energy flux in the liquid water film and at the solid-liquid interfaces for the case of solid wall B: Contribution of translational energy transfer and rotational energy transfer.

that large velocity jump was observed in most cases of linear molecules. The temperature difference between T^{tr} and T^{rot} is remarkable, which shows that the system is in nonequilibrium state.

Thermal energy flux measured at the control surfaces in the film and at solid-liquid interfaces is plotted in Fig. 3. In bulk liquid, the contribution of the rotational motion to the total thermal energy flux is assumed to be around 70 %.⁷ Strongly influenced by the solid wall, the contribution observed in the present simulation is reduced to 60-40 % in the center region of the liquid film, while no contribution is made at the solid-liquid interfaces.

Acknowledgement

This paper reports a portion of the work supported by the Grant-in-Aid for Scientific Research and the 21st Century COE Program "International COE of Flow Dynamics" by the Japan Society for the Promotion of Science (JSPS). All calculations were performed on a SGI Origin 2000 at the Advanced Fluid Information Research Center, Institute of Fluid Science, Tohoku University.

References

- (1) T. Ohara and T. Yatsunami, *Microscale Thermophys. Eng.*, 7-1 (2003), 1-13.
- (2) T. Ohara and D. Torii, *Microscale Thermophys. Eng.*, 9-3 (2005), 265-279.
- (3) T. Ohara and D. Torii, *J. Chem. Phys.*, 122-21 (2005), 214717.
- (4) S. Maruyama and T. Kimura, *Thermal Sci. Eng.*, 7-1 (1999), 63-68.
- (5) T. Kimura and S. Maruyama, *ASME-JSME Thermal Eng. Joint Conf.*, 2003, TED-AJ03-183.
- (6) E. Spohr and K. Heinzinger, *Ber. Bunsenges. Phys. Chem.*, 92 (1988), 1358-1363.
- (7) T. Ohara, *J. Chem. Phys.*, 111-14 (1999), 6492-6500.

A numerical analysis of aerofoil flutter in ground effects

T. Kawahara^{*}, M. Kikuchi^{**}, and K. Hirano^{**}

^{*} Graduate School, University of Miyazaki,

^{**} Dept. of Mech. Systems Eng., University of Miyazaki

ABSTRACT

The “Aero-train” flies in the close field above the ground using ground effects. It is important for Aero-train that making known the relationship between the Ground Effects and “Flutter”. So we simulated Aerofoil Flutter in Ground Effects. We made wing models having arbitrary oscillations and they were analyzed both situations with or without ground. After the phenomena of the flow around the oscillating wing were considered, we calculated the Aerodynamic works that the oscillating wing gets from the flowing fluids during one-period of its oscillation.

Key Words: Wing in ground effect, aero-train, aerofoil flutter, unsteady flow, unsteady aerodynamic force

1. Introduction

Researches of a new rapid transport system with an environmental affinity “Aero-train” are conducted mainly in Tohoku University and University of Miyazaki. The Aero-train has wings and it glides in the close-field above the ground using ground effects. Until now, although researches for improvements of lift and drag in the ground effects have been held a lot, there has been little research for the dynamic stability of the wing in the ground effects. So it is thought that making known the mechanism how the ground effects affect to dynamic stability of the wing is very important. To elucidate the effects of ground on aerofoil flutter, we calculated the aerodynamic work on the aerofoil oscillating in two-freedom of heaving and pitching oscillations.

2. Flutter analysis

There is a phenomenon called “Flutter” which relates to the stability of wing. It is self-induced oscillation with two-degree-of-freedom: heaving and pitching, which occurs when wing get energy from fluids flowing around it. In this paper, we simulated the flutter in the ground effects using a numerical analysis method. We made wing models having arbitrary oscillations and they were calculated for both situations with or without the ground using a thermo-fluid analysis software FLUENT. After the phenomena of the flow around the wing were considered, the aerodynamic works that the wing gets from the flowing fluids during one-period of its oscillation were calculated.

The oscillation modes are given by

$$h = h_0 \sin(2\pi ft) \quad \text{for heaving motion} \quad (1)$$

$$\alpha = \alpha_0 \sin(2\pi ft - \phi) \quad \text{for pitching motion} \quad (2)$$

where ϕ is the phase difference between the heaving and the pitching oscillations. The numerical parameters used in calculation are listed in Table 1, where $A_g = \alpha_0 b' / h_0$: amplitude ratio of the pitching and heaving oscillation at the leading edge of the aerofoil and b' is 1/4 chord length. H is the trailing edge time average height above the ground. The aerofoil section used in the calculation is NACA0012.

Table 1 Numerical parameter in the calculations

U [m/s]	5, 10, 15
ϕ [rad]	0, $\pi/6$, $\pi/3$, $\pi/2$, $2\pi/3$, $5\pi/6$, π
H/b	inf, 4, 1, 0.75, 0.5
h_0 [m]	2×10^{-3}
α_0 [rad]	0.08
A_g	1
f [Hz]	10
ρ [kg/m ³]	1.225
μ [Pa · s]	1.7894×10^{-5}

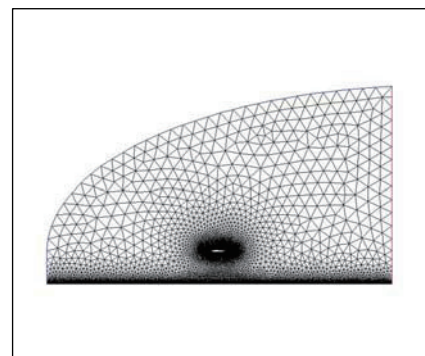


Fig. 1 Element breakup in the calculating area above the ground.

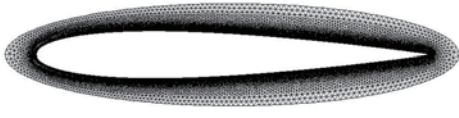


Fig. 2 Dynamic mesh zone

Fig.1 shows the element breakup in the calculating area above the ground and fig.2 shows the dynamic mesh zone around oscillating aerofoil. The number of mesh is 61,260~132,624, it depends on the oscillating modes and the height of the aerofoil.

As the boundary condition, the uniform flow velocity and a turbulent intensity are given at the inlet, the pressure is given at the outlet. In this problem there is a strong interference of the aerofoil and the ground through the fluid, we gave the moving ground with the same velocity as the inlet velocity.

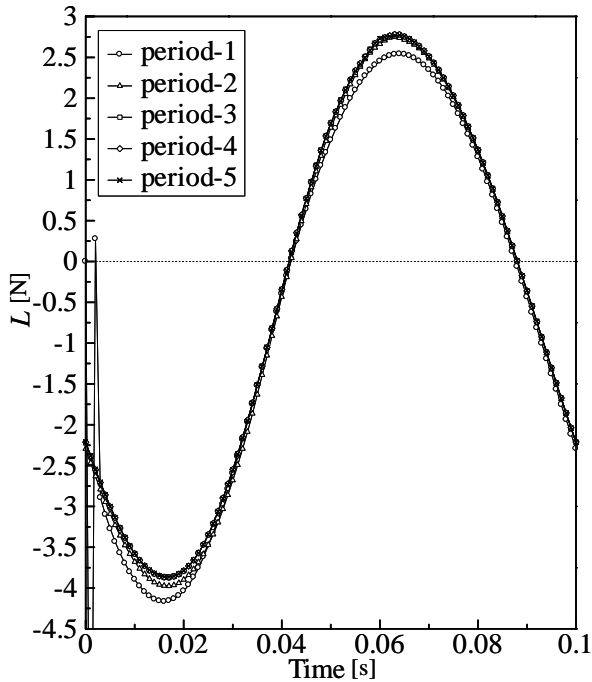
The aerodynamic work in a period W is given by

$$W = \frac{1}{T} \int_0^T (L(-\dot{h})dt + M\dot{\alpha}dt) \quad (3)$$

where L is lift, M is nose up moment. When it is positive, the oscillation of the aerofoil is encouraged by the air flow.

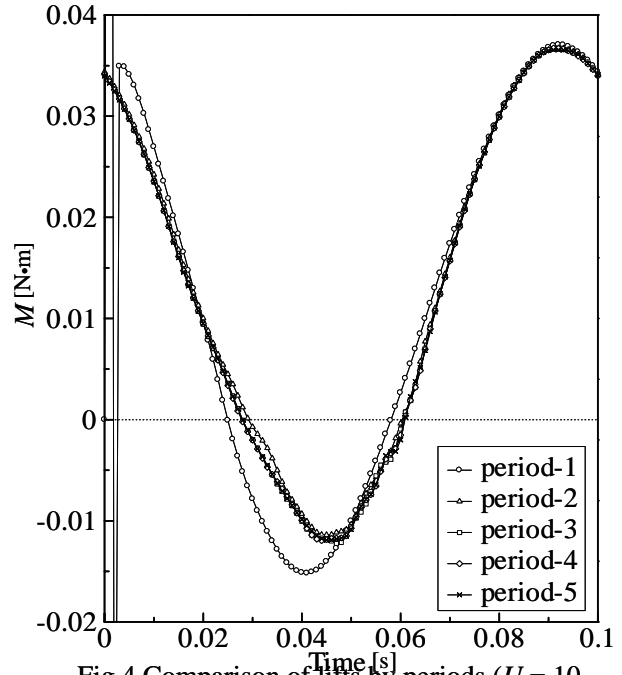
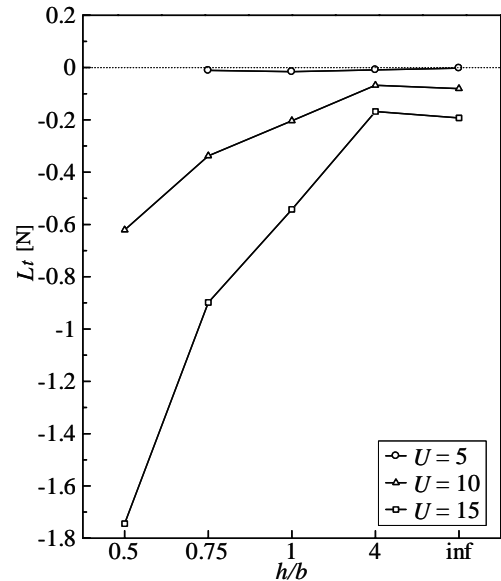
3. Numerical results and consideration

We created the meshes close to the aerofoil surface instead of using the wall function in the calculation. We confirmed the non-dimensional parameter $y^+ = \rho u_\tau y / \mu$ was less than unity in all cases, where u_τ the friction velocity and y the distance between the closest mesh

Fig.3 Comparison of lifts by periods ($U = 10$ [m/s], $\phi = 5\pi/6$, $H/b = 0.5$, $Re = 3.4 \times 10^4$)

point and the aerofoil surface.

Fig. 3 and 4 show the lift force and the moment for five periods respectively, in the heaving and the pitching oscillations, where the phase lag ϕ is $5\pi/6$, average height H/b is 0.5, the reduced frequency $k_f = 2\pi f b / U$ is 0.31. The time average of lift is negative and the nose up moment is positive. Fig. 5 shows the time average lift for the fifth period. The reason is that the lift is exerted at near the maximum thickness of the aerofoil 30% chord, on the other hand the pitching axis is 25% chord. It is supposed to work the Venturi effect in the oscillating case.

Fig.4 Comparison of lifts by periods ($U = 10$ [m/s], $\phi = 5\pi/6$, $H/b = 0.5$, $Re = 3.4 \times 10^4$)Fig. 5 Time average of lifts in the fifth period ($\phi = \pi/6$)

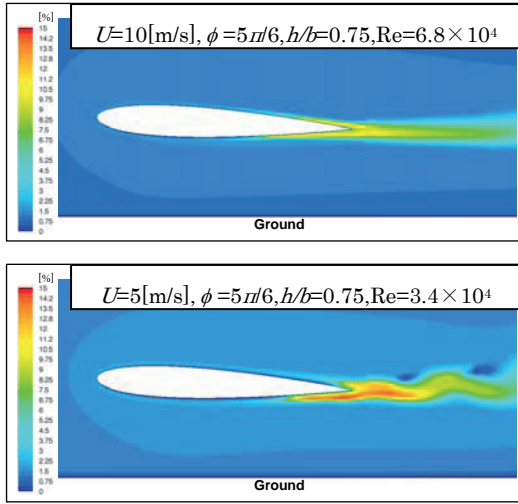


Fig.6 Turbulent intensity distribution

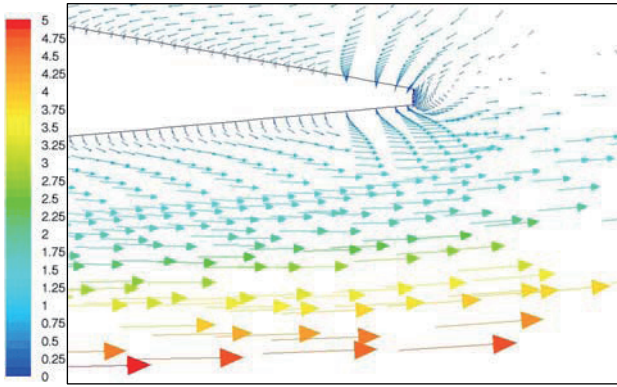

 Fig.7 Velocity vector around the trailing edge
($U=5\text{m/s}$, $\phi=5\pi/6$, $h/b=0.75$, $\text{Re}=3.4 \times 10^4$)

Fig.6 shows the turbulent intensity I in the flow fields, where

$$I = \sqrt{(2/3)k} / U \quad (4)$$

$$k = \frac{1}{2} \overline{u_i' v_j'} \quad (5)$$

k is the turbulent energy. The turbulent intensity for $U = 10\text{m/s}$ is stronger near the trailing edge of the aerofoil than for $U = 5\text{m/s}$. In the calculation, the frequency was fixed at 10Hz, then the former reduced frequency is 0.31, the latter is 0.62. The difference of the turbulent intensity is due to unsteadiness. Fig.7 shows velocity vector near the trailing edge for $k_f = 0.62$, the reverse flow is seen in the upper side of the near trailing edge. It may be the cause of the increase of the turbulent intensity. Fig 8 shows the velocity profile which is colored by the turbulent intensity. The velocity gradient becomes smaller traveling towards the trailing edge.

In the calculation of aerodynamic work, we used the aerodynamic force in the fifth period, because the both of lift and moment have same value after the third period. Fig.9 shows the dependence of aerodynamic works on the

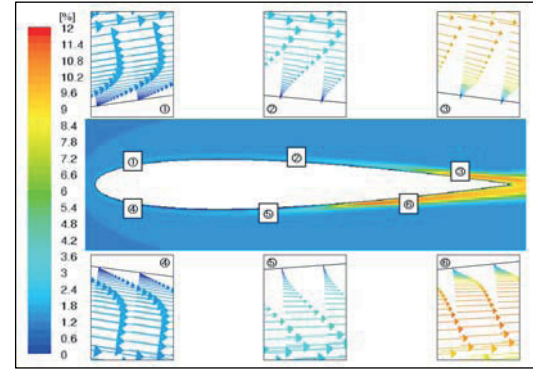


Fig.8 Velocity gradient on the oscillating aerofoil colored by the turbulent intensity.

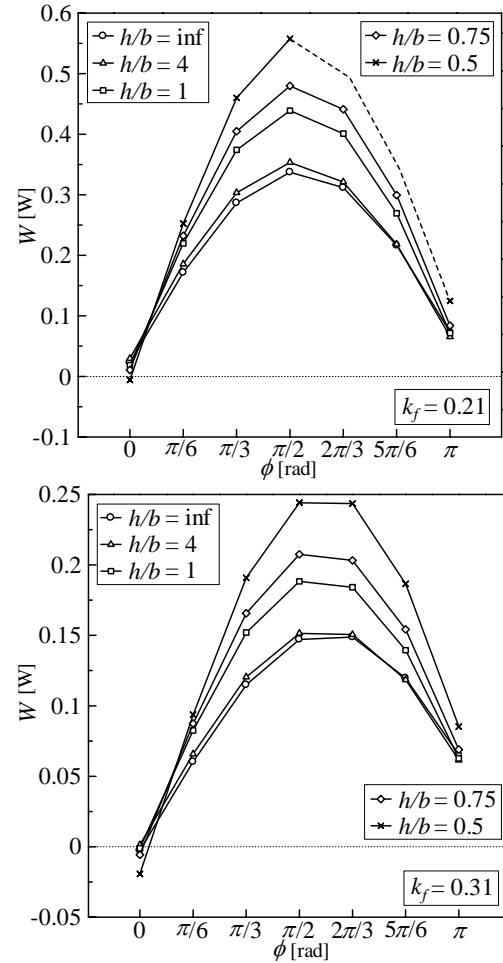


Fig.9 The dependence of aerodynamic work on phase for $U = 15\text{m/s}$ (upper) and 10m/s (lower) lag between the heaving oscillation and the pitching oscillation. It is well known that the maximum work is done near $\phi = \pi/2$, fig.9 shows that the ground increases the work.

4. Summary

The relation between the flutter phenomena and the aerodynamic works was considered. As a result, we came out the tendency of relation between the flutter phenomena and aerodynamic works.

JAXA Special Publication JAXA-SP-07-026E

Date of Issue : February 29, 2008

Edited and Published by : Japan Aerospace Exploration Agency

7-44-1 Jindaiji-higashimach, Chofu-shi, Tokyo 182-8522, Japan

URL : <http://www.jaxa.jp/>

Printed by : NORTH ISLAND Co., Ltd

Inquires about copyright and reproduction should be addressed to the Aerospace Information Archive Center, Information Systems Department, JAXA.

2-1-1 Sengen, Tsukuba-shi, Ibaraki 305-8505, Japan

Phone : +81-29-868-5000 Fax : +81-29-868-2956

Copyright © 2008 by JAXA.

All rights reserved. No part of this publication may be reproduced, stored in retrieval system or transmitted, in any form or by any means, electronic, mechanical, photocopying, recording, or otherwise, without permission in writing form the publisher.

